INSTITUTO SUPERIOR DE ENGENHARIA DO PORTO

MESTRADO EM ENGENHARIA MECÂNICA

J-Integral analysis of the mixed-mode fracture behaviour of composite bonded joints

FERNANDO JOSÉ CARMONA FREIRE DE BASTOS LOUREIRO
novembro de 2019

POLITÉCNICO
DO PORTO

Instituto Superior de Engenharia do Porto

J-INTEGRAL ANALYSIS OF THE MIXED-MODE FRACTURE BEHAVIOUR OF COMPOSITE BONDED JOINTS

Fernando José Carmona Freire de Bastos Loureiro

1111603

2019

ISEP – School of Engineering

Mechanical Engineering Department

POLITÉCNICO
DO PORTO

Instituto Superior de
Engenharia do Porto

J-INTEGRAL ANALYSIS OF THE MIXED-MODE FRACTURE BEHAVIOUR OF COMPOSITE BONDED JOINTS

Fernando José Carmona Freire de Bastos Loureiro

1111603

Dissertation presented to ISEP – School of Engineering to fulfil the requirements necessary to obtain a Master's degree in Mechanical Engineering, carried out under the guidance of Doctor Raul Duarte Salgueiral Gomes Campilho.

2019

ISEP – School of Engineering

Mechanical Engineering Department

POLITÉCNICO
DO PORTO

JURY

President

Doctor Elza Maria Morais Fonseca

Assistant Professor, ISEP – School of Engineering

Supervisor

Doctor Raul Duarte Salgueiral Gomes Campilho

Assistant Professor, ISEP – School of Engineering

Examiner

Doctor Filipe José Palhares Chaves

Assistant Professor, IPCA

ACKNOWLEDGEMENTS

To Doctor Raul Duarte Salgueiral Gomes Campilho, supervisor of the current thesis for his outstanding availability, support, guidance and incentive during the development of the thesis.

To my family for the support, comprehension and encouragement given.

KEYWORDS

Adhesively-bonded joints, Single-Leg Bending, *J*-integral method, fracture mechanics, fracture toughness, fracture envelope, finite element method, cohesive zone models, cohesive laws.

ABSTRACT

The adhesive technology has been constantly growing and expanding into industrial environments, not only for traditional applications but also for high-end applications, where it has been competing fairly with the conventional connection technologies, such as welding, brazing, bolting and riveting. Its unique key features allow it to raise the type of technology to unreachable levels, for certain applications, by its competitors. Some of the advantages are the lightness of the adhesively-bonded joints, good behaviour under cycling and fatigue loading conditions, flexibility in bonding several types of materials and low stress concentrations. However, in order to design and develop efficient adhesively-bonded joints, the strength prediction must be accurate for the assessment of the fracture properties, mainly the critical energy release rate for tensile (J_{IC}) and shear (J_{IIC}), associated to the mode I and II, respectively. For most of the adhesively-bonded joints applications, the loading conditions under operational service feature a combination of different stresses, for instance tensile and shear stresses, from which the concept of mixed-mode came to exist. For this reason, the assessment of fracture properties under those conditions is essential, especially the energy release rates related to different mode-mixities. The fracture properties are related to Fracture Mechanics and are obtained through energetic analyses, from which three methods are often used: models based on the measurement of the crack length during the damage propagation, models based on an equivalent crack length and methods based on the *J*-integral formulation. In the specific case of the *J*-integral it is furthermore possible to obtain the cohesive laws of the adhesive, which can be later used in the design of adhesively-bonded joints.

This current work presents an experimental and numerical analysis of a Single-Leg Bending (SLB) adhesively-bonded joint where the specimens were bonded with three distinct adhesives, in order to assess and compare their behaviour under mixed-mode load conditions, fracture properties and cohesive laws. For that purpose, the *J*-integral formulation of Ji et al. [1] was considered to obtain the energy release rate for mode I and II, tensile (J_I) and shear (J_{II}), respectively, whereas the cohesive laws are attained through direct differential operation of the J_I-w_0 and J_{II}-δ_0 curves, where w_0 and δ_0 are the local normal separation and local tangential slip between the two adherends at the cross-section of the crack tip, respectively. Afterwards, the fracture analysis was performed, where the experimental results were compared through load-displacement (P-δ) curves. The J_I and J_{II} values, obtained through correlation between experimental and numerical results incorporated into the *J*-integral formulation, were addressed by *R* curves and fracture envelopes. These latter were used to establish which criterion was more suitable for each adhesive type. For last, the tensile and shear stresses were determined through the cohesive laws, attained by the direct method. Overall, a good agreement on the fracture properties was obtained between the specimens of the same adhesive. Moreover, the cohesive laws also presented a good correspondence between specimens, and further enabled the design of adhesively-bonded joints with arbitrary geometry.

PALAVRAS CHAVE

Juntas adesivas, Single-Leg Bending*, método do integral J, mecânica da fratura, tenacidade à fratura, envelope de fratura, Método de Elementos Finitos, modelo de dano coesivo, leis coesivas.*

RESUMO

A tecnologia adesiva tem vindo a evoluir significativamente, expandindo-se para ambientes industriais, não apenas para aplicações convencionais, mas também para aplicações de elevada exigência, onde compete justamente com outras tecnologias de conexão tradicionais, como a soldadura, brasagem e ligações aparafusadas e rebitadas. As suas características únicas permitem elevar esta tecnologia para níveis inacessíveis, para certas aplicações, relativamente às suas concorrentes. Algumas das vantagens são o baixo peso das juntas adesivas, bom comportamento sob condições de cargas cíclicas e à fadiga, flexibilidade na construção da junta, possibilidade para ligar materiais diferentes e também baixa concentração de tensões. Contudo, a fim de projetar e desenvolver juntas adesivas eficientes, a previsão da resistência deve ser precisa para a avaliação das propriedades de fratura, principalmente a taxa crítica de libertação de energia em tração (J_{IC}) *e corte* (J_{IIC})*, associada ao modo I e II, respetivamente. Na maioria das aplicações de ligações adesivas, as condições de carga cujas juntas estão sujeitas, sob condições de serviço operacional, consistem numa combinação de esforços distintos, como por exemplo tração e corte, a partir dos quais o conceito de modo misto foi criado. Por essa razão, é essencial a avaliação das propriedades de fratura sob essas condições, especialmente as taxas de libertação de energia relacionadas a diferentes modos mistos. As propriedades de fratura estão relacionadas com a Mecânica da Fratura e são obtidas através de análises energéticas, das quais são frequentemente utilizados três métodos: modelos baseados na medição do comprimento de fenda durante a propagação do dano, modelos baseados no comprimento de fenda equivalente e métodos baseados na formulação do integral J. No caso específico do método do integral J, é ainda possível obter as leis coesivas do adesivo, que podem ser utilizadas posteriormente no projeto de juntas adesivas.*

Nesta dissertação é apresentada uma análise experimental e numérica realizada a uma junta adesiva de configuração Single-Leg Bending (SLB) *onde os provetes foram colados com três adesivos distintos, de modo a avaliar e comparar o seu comportamento sob condições de carga em modo misto, as suas propriedades à fratura e as respetivas leis coesivas. Para esse efeito, considerou-se a formulação proposta por* Ji et al. [1] *do método do integral J, de modo a determinar a taxa de libertação de energia para os* *modos I e II, tração (J_I) e corte (J_{II}), respetivamente, enquanto as leis coesivas foram obtidas por derivação direta das curvas J_I-w_0 e J_{II}-δ_0, onde w_0 e δ_0 correspondem à separação normal local e deslizamento tangencial local entre os dois aderentes na secção transversal da ponta da fenda, respetivamente. Posteriormente, foi realizada uma análise de fratura onde os resultados experimentais foram comparados, através de curvas carga-deslocamento (P-δ). Os valores de J_I e J_{II}, obtidos através da correlação de dados experimentais e numéricos incorporados na formulação do integral J, foram analisados pelas curvas R e envelopes de fratura. Estes últimos foram utilizados para estabelecer qual o critério mais apropriado para cada tipo de adesivo. Por fim, as tensões de tração e corte foram obtidas das leis coesivas, estimadas pelo método direto. No geral, foi conseguido um bom acordo entre as propriedades à fratura entre os provetes colados com o mesmo adesivo. Além disso, as leis coesivas apresentaram uma boa correspondência entre os provetes, possibilitando assim o projeto de justas adesivas de geometria arbitrária.*

LIST OF SYMBOLS AND ABBREVIATIONS

List of abbreviations

2D	Two Dimensions
3D	Three Dimensions
4ENF	Four-Point End Notched Flexure
ADCB	Asymmetric Double Cantilever Beam
ASTM	American Society for Testing and Materials
BSI	British Standard Institution
CBBM	Compliance Based Beam Method
CDCB	Contoured Double-Cantilever Beam
CO_2	Carbon Dioxide
CZM	Cohesive Zone Models
DCB	Double Cantilever Beam
DIC	Digital Image Correlation
ELS	End Loaded Split
ENF	End Notched Flexure
FE	Finite Elements
FEM	Finite Element Method
FPZ	Fracture Process Zone
ISO	International Organization for Standardization
LEFM	Linear Elastic Fracture Mechanics

LVDT	Linear Variable Differential Transformer
MMF	Mixed-Mode Flexure
PEK	Polyarylene Ether Ketone
PES	Polyaryl Ether Sulfone
SAAS	Stress Analysis for Adhesive Structures
SLB	Single-Leg Bending
SLJ	Single Lap Joint
TDCB	Tapered Double-Cantilever Beam
XFEM	eXtended Finite Element Method

List of units

°C	Degree Celsius
bar	Bar
g	Grams
GPa	GigaPascal
Hz	Hertz
kN	KiloNewton
min	Minute
mm	Millimetre
mm$_2$	Square millimetre
MPa	MegaPascal
N	Newton
s	Second

List of symbols

a	Crack length
A	Area enclosed by C
a_0	Initial crack length
A_i	Cross-section area of the beam
A_i	Axial stiffness of the beam
B	Adherends width
C_0	Beam compliance
c_i	Half-thickness of the beam
D_i	Bending stiffness of the beam
ds	Element of arc length along C
E	Young´s modulus
E_f	Flexural modulus
E_x	Young´s modulus, *x* direction
E_y	Young´s modulus, *y* direction
E_z	Young´s modulus, *z* direction
G	Energy release rate
G	Shear modulus
G_C	Critical energy release rate
G_{IC}	Critical energy release rate for tensile (mode I)
G_{IIC}	Critical energy release rate for shear (mode II)
G_{int}	Energy release rate from thermal and mechanical load interaction
G_T	Energy release rate from residual stresses

G_{xy}	Shear modulus, *xy* plane
G_{xz}	Shear modulus, *xz* plane
G_{yz}	Shear modulus, *yz* plane
h	Adherends thickness
h_i	Thickness of the beam
h_t	Adhesively-bonded joint thickness
I	Second moment of area
J_I	Energy release rate for tensile (mode I), *J*-integral method
J_{IC}	Critical energy release rate for tensile (mode I), *J*-integral method
J_{II}	Energy release rate for shear (mode II), *J*-integral method
J_{II}	Critical energy release rate for shear (mode II), *J*-integral method
k	Shear correction factor
$\mathbf{K}$	Constitutive matrix
L	Distance between the roller and the applied load
L	Distance between the centerline of the rollers at the edges of the joint and the loading line, halfway between the upper adherend
M_1	Bending moment, mode I
M_2	Bending moment, mode II
M_L	Bending moment
n_j	Outward normal vector of the contour C
P	Load
P_{max}	Maximum load
Q_i	Shear force applied to the beam

Q_T	Resultant shear forces on the bonded joint
t_A	Adhesive thickness
t_m^0	Mixed mode cohesive strength
t_n	Tensile strength
t_n^0	Maximum tensile strength
t_s	Shear strength
t_s^0	Maximum shear strength
U	Strain energy
u_i	Displacement vector
V_i	Transverse load of the beam
w	Normal separation between the bottom fiber of the upper beam and the top fiber of the lower beam
w_0	Local normal separation between the two adherends at the cross-section of the crack tip
W_f	Work of external forces
w_{nk}	Strain energy density
α	Power law exponent
γ_f	Shear failure strain
δ	Displacement
δ	Tangential slip between the bottom fiber of the upper beam and the top fiber of the lower beam
δ_0	Local tangential slip between the two adherends at the cross-section of the crack tip.
δ_{ij}	Kronecker tensor

δ_{Pmax}	Displacement at maximum load
ε	Strain
ε_f	Tensile failure strain
ε_n	Tensile strain
ε_s	Shear strain
θ_P	Relative rotation between the two adherends at the loading line
ν	Poisson´s ratio
ν_{xy}	Poisson´s ratio, *zy* plane
ν_{xz}	Poisson´s ratio, *xz* plane
ν_{yz}	Poisson´s ratio, *yz* plane
σ	Normal interface stress
σ	Tension
σ_f	Tensile failure stress
σ_{ij}	Stress tensor
σ_y	Tensile yield stress
τ	Shear interface stress
τ_f	Shear failure strength
τ_y	Shear yield strength

FIGURES INDEX

TABLES INDEX

INDEX

INTRODUCTION

1 INTRODUCTION

1.1 Framework

Currently, adhesively-bonded joints are used in a wide range of applications, some featuring several advantages over the traditional joining processes. With the introduction of structural adhesives in the most demanding applications, it is essential to know the mechanical and fracture properties relevant to these potential applications, as well as their behaviour against various types of adherends. Depending on the type of application and loading conditions, in operational service, to which the adhesively-bonded joint may be subjected, the solicitations may vary, thus influencing the performance of the adhesively-bonded joint, which is dependent on its capacity to withstand the applied stresses. There are several destructive tests to assess the adhesively-bonded joint behaviour and performance under several distinct loading conditions, to which the adhesively-bonded joint may be subjected, and evaluate its fracture properties. The assessment of these properties is very important since it allows to predict their strength. An adhesively-bonded joint, when used in operational service, may be subjected to tensile or shear stresses, although the existence of these individual stresses alone is unusual since, most of the times, the combination of both is most frequent, thus creating the mixed-mode. Therefore, the assessment of the adhesively-bonded joint properties, considering the mixed-mode, is crucial. In fact, there are numerical methods, such as cohesive zone modelling, related to finite element analysis, to predict the strength of an adhesively-bonded joint although, for this method, the energy release rate in mode I (J_I) and mode II (J_{II}), associated to tensile and shear stresses respectively, are fundamental. Moreover, besides the energy release rate, due to the mixed-mode loading conditions, it is necessary to establish a fracture criterion that promotes damage propagation under these conditions. From the diverse criteria available, it is extremely important to define the most suitable criterion based on each kind of adhesively-bonded joint behaviour. Therefore, the fracture tests under mixed-mode conditions grant the possibility to characterize and locate the adhesive failure in the fracture envelope in order to define the most suitable fracture criterion.

1.2 Objectives

The scope of this thesis is the assessment of the energy release rate, considering combined tensile (mode I) and shear (mode II) loading conditions, through the *J*-integral method, proposed by Ji et al. [1], and the assessment of the cohesive laws based on the cohesive zone model approach. The Single-Leg Bending (SLB) geometry was considered for the adhesively-bonded joints between composite adherends, based on unidirectional carbon-epoxy pre-preg, and bonded together with three distinct adhesives (brittle, moderately ductile and ductile). The SLB joint geometry allows to characterize the energy release rate of each adhesive type under combined loading conditions, mode I and mode II. Through the experimental tests, the results obtained are collected and the load-displacement (P-δ) curves are established. Also, in parallel, a numerical simulation analysis is performed, using the software Abaqus®, to obtain the geometrical parameters required in Ji et al. [1] formulation. After, both experimental and numerical data are correlated and, through Ji et al. [1], the J_I and J_{II} are obtained and represented through R curves, for each type of adhesive. The results are showcased by the fracture envelopes will allow to identify the location of J_I and J_{II}, in comparison to J_{IC} and J_{IIC}, which are the correspondent values to pure mode, and establish the most suitable propagation criterion for each type of adhesive, in mixed-mode. Finally, the cohesive laws for each type of adhesive are obtained, considering the triangular model, from direct derivation of the energy release rates, function to the geometrical parameters from the J-integral formulation.

1.3 Thesis layout

The present thesis is structured as follows:

Chapter 1 – General framework of the thesis content in the panorama of adhesive bonding technology, the scope and the main targets of the thesis and the overall structure of the thesis.

Chapter 2 – Adhesive bonding technology theoretical background where some basic concepts of the technology are described, such as the general properties, applications, typical loads and failure modes that the adhesively-bonded joint may subjected, as well as their possible configurations, optimized for each kind of loading conditions, and the current structural adhesives properties, advantages and applications. There are also more specific sections, related to the theme of the thesis, that are needed further along the thesis content, such as the strength prediction of adhesively-bonded joints and fracture toughness tests. The last section is fully dedicated to the SLB test, where all the aspects are referred, from the test characterization to the existing formulations and methods applicable for this kind of adhesively-bonded joint configuration.

Chapter 3 – Description of the thesis main content and development. Includes the detailed description of the materials used for the adherend and the type of adhesives used, following by the experimental work description, step by step until the final results, and P-δ curves. Next, the numerical work is described, where the numerical conditions are established and the cohesive zone model method explained. The last section is related to the results, where the analytical approach for the *J*-integral parameter estimation procedure, based on Ji et al. [1] formulation, is explained. The fracture analysis where the results from the experimental and numerical works are showcased and interpreted for each adhesive type and, finally, the data analysis is presented, where the three adhesives behaviour are compared between each other and also according to the specialty literature.

Chapter 4 – Final conclusions obtained from the overall thesis and potential future works developed from it.

THEORETICAL BACKGROUND

2 THEORETICAL BACKGROUND

2.1 Adhesive bonding

Adhesives have been around in our everyday life without proper recognition of their true potential, sometimes even despising the power of a simple “glue”, which is traced as one of the technologies of the future. Nature, for a thousand of years, has been supplying natural products, such as bones, skins, fish, milk and plants, which we used for several bonding applications. The 20th century marks a new step in the adhesive bonding technology history with the introduction of synthetical polymers and, today, the range of adhesive applications reaches the industrial market [2]. With the adhesive business expansion, applications abound from office “post-it-notes®” to automotive safety glass, footwear, aerospace structures or “no-lick” postage stamps [3]. Many products that are used in a daily basis would not exist if it were not for adhesive bonding. Being one of the future technologies, research and development of adhesives and sciences surrounding their applications has never been more important for scientists and engineers in order to meet tomorrows demands [3].

2.1.1 Bonded joints’ characterization

The scope of this chapter is to describe bonded joints generalities such as: What is it and how it’s constituted; Who “discovered” adhesive bonding and for what application; Why they are better, or not, than other connection technologies; Their properties; How it’s made the bonded joint.

2.1.1.1 Concept

Adhesives have been used for many centuries, however, only about 70 years ago did adhesives undergone a major evolution, greatly due to the introduction of synthetic polymers which brought new properties as compatibility with other material and strength. During the process of evolution of adhesive technologies, several concepts were formulated and terminologies created to characterize adhesive bonds [2].

The concept of adhesive can be defined as a material capable of holding two or more surfaces while maintaining the joint in a rigid and permanent form [3].

Adhesives have the following characteristics [3]:

- Behave in a liquid state so that when applied, they can spread and wet the surface to be bonded creating an intimate contact with the surface of the adherends;
- Create a layer on the surface of the adherend to develop adhesion phenomenon, where the intermolecular forces are present;
- Harden to withstand continuous and variable loads during their lives;
- Transfer and distribute the loads applied to the components of the assembly;
- Fill empty spaces, cavities and gaps, also acting as sealant;
- Cooperate with other components from the assembly to ensure the product durability.

Adhesives are generally grouped as structural and non-structural. The structural term is generally given to adhesives made by synthetical polymers which are able to resist high loads, responsible for the structural integrity, strength and stiffness of the assembly (≈7 MPa shear), and which have good environmental resistance [4]. Structural adhesives are usually expected to last the same lifetime as the product where they are applied. The non-structural term is applied generally to adhesives with lower strength and permanence usually used for fastenings or to bond weak adherends [3].

Adhesion is the phenomenon behind the bonded connection and is defined as the attraction between two different materials through intermolecular forces. Cohesion, on the other hand, only involves the intermolecular forces between a single material. These two phenomena define the typical failure modes in bonded joints. The intermolecular forces attracting the both materials are primarily van der Waals [3].

Adherend is the material where the adhesive is applied and usually, after the bonding process is complete, this material is designated as adherend, although these two terms are used without distinction [3].

The area between the adherend and adhesive is defined as the interphase. The physical and chemical properties of the interphase are different from all the materials present in the bonded joint and its nature will directly impact the mechanical properties of the adhesively-bonded joint [2].

Interface, different from interphase, is the contact plane between the surface and two materials, and if is inserted within the interphase. The interface, often referred as boundary layer, is useful to define and measure the surface energy. Within the interphase, there could be several interfaces between different materials localized between the adherend and the adhesive [2].

The joint is the final product from the adhesive bonding process, combining all the elements, represented in Figure 1: adhesive, adherend, primer if applied, and the interphase and interface associated to it [2].

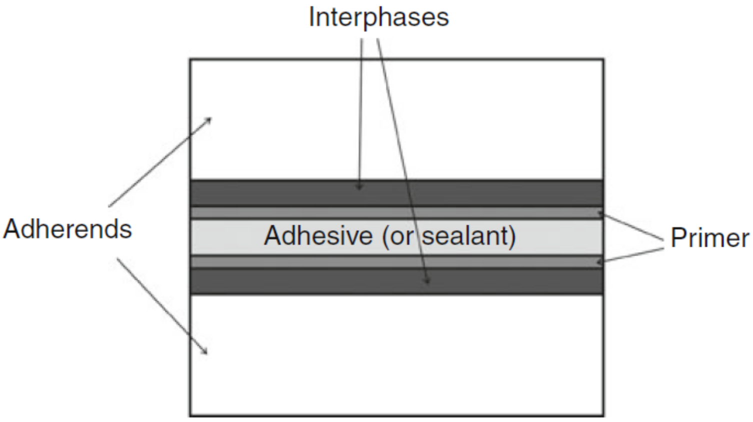

Figure 1 - Structural representation of an adhesive joint [2].

2.1.1.2 History background

Adhesive bonding history is rich, and it goes back to thousands of years ago, where the first evidences of this technique were registered in old writings and archaeological artefacts. The need of more decorous, stronger, useful or maybe cheaper objects, lead the adhesive bonding technique to be used continually along the history of human kind, using the nature resources given, until a few centuries back. It's unknown that it was a certain individual that discovered the adhesive technique. Instead, adhesives were likely introduced gradually from applications which used "sticky" products to preparations of simple adhesives [5].

The major step in the adhesive history began in early 1900s with the introduction of synthetic polymeric adhesives, which surpass the conventual natural based adhesives due to the stronger bonding performance, several formulation possibilities and higher resistance to the environmental exposure. However, traditional non-polymeric adhesives are still widely used due to a large range of applications that do not require, for instance, high environmental resistance [3].

The development of phenol formaldehyde adhesive, in 1910, for plywood industries marks the era of modern adhesives introduction into the industrial market, especially in construction [3]. Significant advances were then again achieved between 1940s and 1950s with direct contribute of the military aircraft industry developing structural adhesives. The unique characteristic of these new adhesives, specially the strength-to-weight ratio, lead to a successful partnership between this new technology and an industry in need of an efficient and reliable connection method. For decades, synergies between adhesive technology and military aircraft industries were strengthened, overcoming several difficulties, such as the durability of adhesive joint, until advanced adhesive systems, were defined, introduced and verified in the late 1970s [3].

The performance of the adhesive technology in the industrial environment, during 20th century, was a success and soon became clear that adhesives could be an upgrade in comparison to the traditional mechanical connection technologies such as welding, brazing, or riveting [3].

Today, adhesive technology, after almost a century of research and development, defining its basic rules, standards and methods for reaching high performance joints, built a strong foundation of formulation and process. These foundations lead the industries to embrace the technology and even develop it in order to reduce production cycle time and cost, control the environmental impact, and experiment new applications with different adherends made by new materials such as engineering polymers, advanced composites and ceramics [3].

2.1.1.3 Advantages & Disadvantages

Joining technologies should be considered based on the product requirements. Adhesive technology sometimes can be the optimal solution, sometimes can be the worst possible solution and sometimes neither of them [3]. Selection of the joining process can be arduous, certainly not consensual, since it may involve several variables with different grades of importance according with the established requirements. The variables may be, for instance, working environment, mechanical performance, process capability, cost and durability [3].

The main advantages of structural adhesive bonding are [3, 4]:

- Stress distribution through the bonding surface which grant higher stiffness and load transmission resulting in weight reduction, meaning overall cost reduction. Stress concentration in the bonding surface are inexistent, due to the stress distribution, increasing the fatigue strength;
- Vibration damping allowing the stresses applied to the joint to be partially absorbed, improving the fatigue resistance of all the bonded components;
- Bonding different materials with dissimilar chemical compositions and physical properties, increasing new possible applications and preventing, for instance, galvanic corrosion between dissimilar metals;
- Effective manufacturing process of join two materials, from mixture to the application, since it can be automated;
- Flexible technology able to combine different concepts and new materials, such as honeycomb structures and advanced composites. Applicable to all geometrical shapes and thicknesses;
- Smooth surfaces without welding marks or screw holes;
- Continuous contact between the bonded surfaces. Also grants sealing capabilities to the bonded joint;
- Tendency to present lower costs compared to other joining technologies;
- Exceptional strength-to-weight ratio if compared to traditional joining technologies.

Adhesive bonding, similarly to any other joining technology, has its disadvantages [3, 4]:

- External solicitations such as peeling forces, cleavage and impact are critical, especially the first, for the safety of the bonded joint. These solicitations must be minimized as much as possible and, if not, adhesive bond is definitely not the most suitable connection process;
- Localized stresses, in the bonded geometry, can jeopardize the joint structural integrity compromising the stress distribution, key feature of adhesive bonding;
- Limited resistance to extreme degrading environments such as moisture, high temperature or chemicals. The adhesive strength degradation may increase, result of continuous stresses or elevated temperatures;
- The long adhesive curing time requires additional equipment, such as jigs, for correct positioning of the joint. Adhesives are often cured at high temperatures, for instance, in industrial ovens or presses;
- Surface preparation is mandatory to achieve good adhesive bonding performance. However, depending on the joint component characteristics, adhesive and adherend, this process can be difficult and time consuming. Usually, the surface preparation can be performed through mechanical abrasion, primary application, chemical attack, solvent degreasing, etc;
- Quality control and safety process for non-destructive trials are not yet completely developed nor standardized. Though improvements have been achieved, with new techniques introduced, this is still a setback for adhesive bonding;
- Inexistent standard calculation procedure for adhesive bonding structures. The bonded joint application has a significant impact on the structural integrity of the joint, meaning that, for instance, a bonded joint designed for an application used only in summer will behave differently if used during the winter.

2.1.1.4 General properties

The design of an adhesive joint is very flexible and diverse, combining several materials with different properties and characteristics. The adhesive and adherends are the components of the joint where it is possible to vary the type of material in order to achieve the most suitable combination of properties for a particular application. The features showcasing the adhesive bonding flexibility are, for instance:

- Reduced acoustics if the adhesive joint has adherends made of sandwich structure composite with a foam core;
- Sealing adhesive joints, specific characteristic of the adhesive, which assigns unique functions to this type of joint;
- Great strength-to-weight, ratio which is a key feature for several industries such as motorsport, aerospace and aeronautics. General automotive industries are investing in this feature since it is directly linked with CO_2 emissions reduction;

- Thin sheet metal bonding, which is a unique feature comparing with the traditional joining technologies.

Adhesive bonding is, without doubt, a great technology, with a promising future, capable of competing with the traditional technologies and, in some applications, even surpass them [3].

2.1.1.5 Stages of the bonding process

The bonding process is rather different and unique when comparing with other conventional joining technologies. The process steps can be defined as: adhesive selection; joint configuration definition; surface preparation; joint manufacturing; process and quality control [4]:

- The selection of the adhesive is made according to the type of application and its operating requirements. Usually, the parameters to be taken into consideration are, for instance, operating temperature and environment, mechanical strength and application method [4].
- Based on the adhesive properties and application characteristics, the joint is designed in order to enhance the adhesive strength. Calculation methods are used to determine the static mechanical strength and eventually the fatigue and fluence strength [4].
- With the adhesive, adherend and joint design defined, and the calculations supporting the adhesive bonding integrity and safety completed, the joint manufacturing process starts with the adherend surface preparation. This step of the process is essential since it will guarantee the required adhesion for a proper initial and then operating behaviour of the adhesive bonding joint [4].
- The manufacturing process then involves applying the adhesive to the adherends to be bonded and curing the adhesive, under specific pressure and temperature conditions, until the joint is completed [4].
- Finally, the adhesive joint undergoes a process of control through several destruction and non-destructive test in order to assess, in the short and long term, whether or not its strength meets the requirements of the application [4].

2.1.2 Common applications of bonded joints

Adhesives are used in a wide range of industries: construction, packaging, furniture, automotive, appliance, textile, aircraft, among many others. Several adhesive business units exist to develop, manufacture and market different adhesive products, to numerous end-user customers, for a wide variety of applications. In some markets and applications, the adhesive technology surpasses the conventional joining technologies [3].

The packaging and construction industries, together, represent the highest percentage of demand for adhesive technology, although non-structural adhesives are the most used in these markets. In construction, adhesives are often used as binder of wood panels, while in packaging they are used within one of the sector largest products, the corrugated boxes. On the other hand, structural adhesives represent a small fraction of the adhesive market, being used mostly by the transportation, industrial assembly and construction industries [3].

The consolidation of structural adhesives in the aircraft industries, which were developed and gradually improved over the years, allows them to be sought for new application and markets. Automotive industries, in the need of efficiency increase and fuel consumption reductions, found in the adhesive bonding technology a potential partnership, as exemplified in Figure 2. The low weight-to-strength ratio alongside with the possibility of connecting different materials, so far difficult to join, allow the automotive industries to overcome those current concerns and seek new possibilities of improvement with adhesive bonding technology [4].

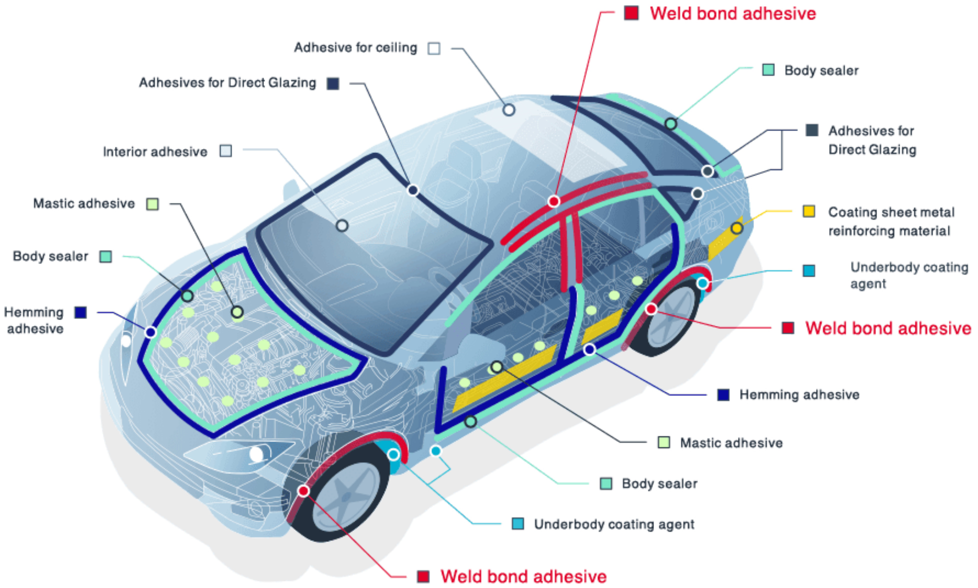

Figure 2 - Adhesive technology application for automotive industries [6].

The naval industry, exploiting new materials mainly for weight reduction and corrosion resistance, such as plastics and composites, is also embracing the use of structural adhesives since they perform a great bonding connection between those materials, especially composites. Keeping into consideration that marine environment is stern and should not be underestimated [4].

The applications of structural adhesive joints are growing in a diversified way and the tendency is to continue increasing due to their clear inherent advantages compared to other technologies. The civil construction industries are using this technology, for example in bridges and small metallic structures, represented in Figure 3, responsible for the structural integrity of the final product. The motorsport industries, in pursuit of speed and performance through weight reduction is using, whenever possible, adhesively-bonded composite joints. The adhesive joint could represent, in the near future, about 50% of all the joints in a competitive vehicle. This market segment is committed to developing and applying this technology due to the recognition of its current potential [4].

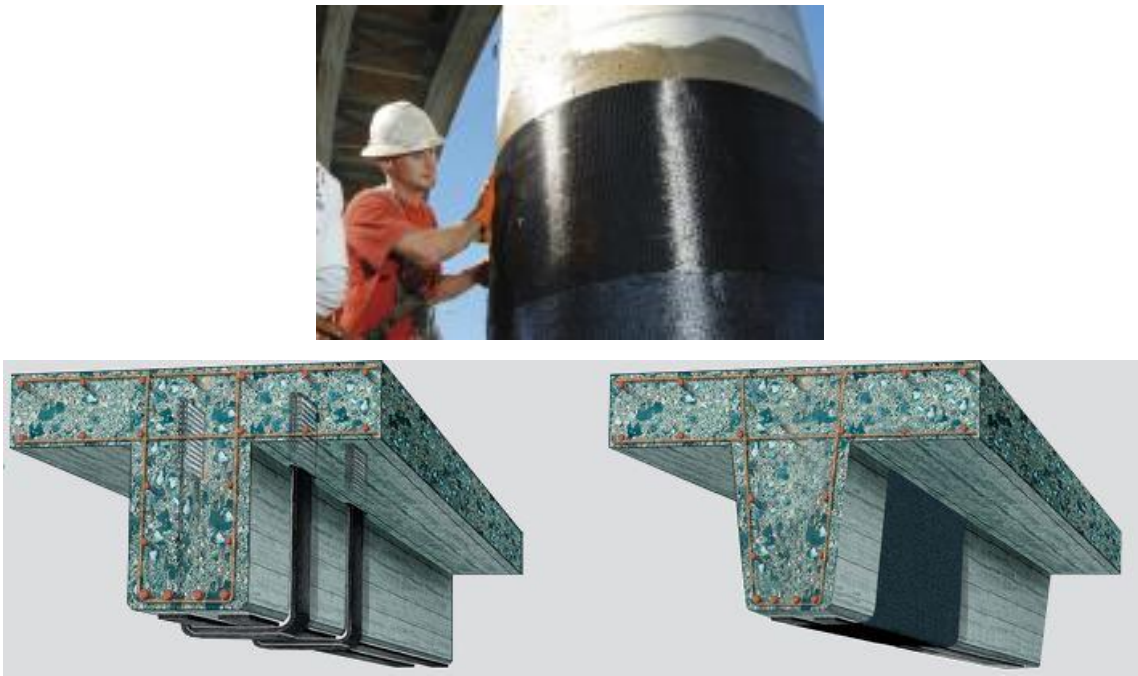

Figure 3 – Epoxy resin & structural engineering systems for construction industries [7].

2.1.3 Typical loads and failure modes in bonded joints

The purpose of adhesively-bonded joints is to safely endure the expected stresses when they are set in service operations. For an adhesive project development, anticipated stresses and environmental conditions must be known and considered in the design. The strength of an adhesively-bonded joint is given by the mechanical properties of the materials comprising the joint, the interfacial contact area and residual stresses within the joint. However, knowing the type of load that the joint will be subjected is also crucial since there are critical types of loads that can jeopardize the adhesively-bonded joint structural integrity if not taken into consideration [3].

Uniform stress distributions, theoretically ideal, are rarely formed in adhesively-bonded joints. Instead, non-uniform stress patterns are predominant. Since the fracture phenomenon starts when and where the local stress surpasses the local strength, the stress concentrations have a high impact on the collapse of bonded joints. Local stresses, caused by external loads, may sometimes exceed many times average stress value.

These stress concentrations are often unpredictable, being responsible for defining the actual force that the adhesively-bonded joint can endure [3].

There are four common load types to which adhesively-bonded joints are usually subjected to: tensile, shear, cleavage and peel, represented in Figure 4. Moreover, it is possible to have combinations or variations of those stresses in adhesively-bonded joints [3].

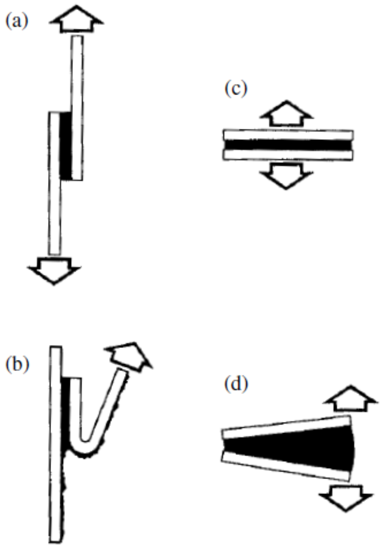

Figure 4 – Common load types to which adhesively-bonded joints are usually subjected: (a) tensile shear; (b) tensile loading; (c) cleavage; (d) peel [8].

Tensile stresses develop when forces perpendicular to the plane of the joint are uniformly distributed along the bonded surface. Therefore, the joint has to be designed in order to ensure the parallelism between the adherend surfaces and normal forces. In practice, due to the difficult process control of the adhesive layer thickness and the difficulty to ensure strictly axial loads, undesirable combinations of stresses tend to develop, such as cleavage or peel. The adhesively-bonded joint, to be effective with high performance, should be designed with guiding plates, for alignment, to assure continuous axial loadings. Also, the adherend should be stiff enough, avoiding undesirable bending, to ensure the uniform distribution of the stresses [4].

Compressive forces, similarly to tensile forces, must be aligned in such a way that the adhesive remains in pure compression. Adhesively-bonded joints subjected to compression only fail if the stress distribution is non-uniform. In fact, an adhesively-bonded joint subjected to pure compression practically does not require adhesive [4].

Shear stresses develop when the forces acting in the adhesive plane trend to separate both adherends. Adhesively-bonded joints designed to endure shear stresses, relying mainly on the adhesive shear strength, are the easiest to manufacture, which in turn makes them the most commonly used. These joints are usually more resistant when subjected to shear stresses since the entire bonded surface is active and the easiest to keep the adherends aligned [4].

Cleavage and peel stresses are natural enemies of adhesively-bonded joints and are considered critical in joint design. Cleavage can be defined as the stress developed by forces applied at one edge of a stiff joint in order to detach both adherends. Peel stresses are similar to cleavage. However, they develop when one or both adherends are not stiff enough and, as a result, the separation angle between the adherends is higher in peel than cleavage. Adhesively-bonded joints subjected to cleavage or peel stresses are normally less resistance than joints subjected to shear stress since the stress concentration is located in a very small area. The stress distribution in an adhesive joint subjected to cleavage is not uniform since the joint edge where the cleavage load is applied has high stress concentrations, while at the opposite end the stresses are practically residual, not contributing to the overall strength of the adhesively-bonded joint. Brittle and stiff structural adhesives are usually quite sensitive to peel forces. Epoxy adhesives, for instance, have a peel strength of nearly 0.35 N/mm. On the other hand, ductile structural adhesives, being more flexible, grant a less concentrated stress distribution increasing the joint strength, in such a way that it can reach 8 N/mm [4].

Knowing the several kinds of forces and loads to which an adhesively-bonded joint can be subjected enables to design and develop an efficient and successful joint. In the same way, the knowledge of the failure mode allows to draw evidence and conclusions about the nature of the installed stresses, stress distribution, adherend surface preparation and adhesive and adherend strength.

Adhesively-bonded joints can fail by adhesion, cohesion or by the combination of both, represented in Figure 5. An adhesive failure may be defined as an interfacial bond failure between the adhesive and adherend, whereas a cohesive failure may be defined as an intrinsic failure in the adhesive, leaving layers of adhesive on the surface of each adherend. If the adherend fails before the adhesive, it is referred to as a cohesive failure of the adherend [3].

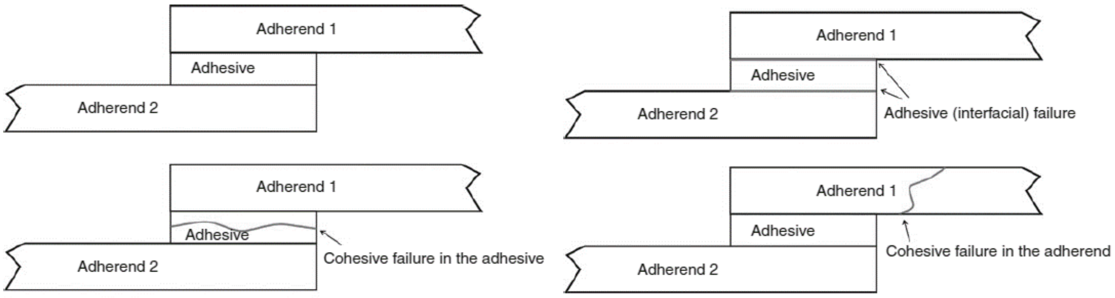

Figure 5 – Adhesively-bonded joints failure modes [2].

Although cohesive failures within the adhesive or the adherend are often considered as preferable scenarios, since the respective material is reaching its strength limit, they should not be considered as single criterion for a joint design and development. The functionality of an adhesively-bonded joint to the design loads is the most reasonable criterion to follow, to the detriment of the joint failure mode, since this last criterion may not guarantee functionality. Still, the failure mode of an adhesive joint is a very useful criterion, since it allows identifying the limiting failure type. For instance, an adhesive failure can be due to weak boundary layer or due to insufficient surface preparation [3].

2.1.4 Joint configurations

Adhesively-bonded joints are often designed in a variety of configurations aiming to achieve the highest performance from the adhesive when subjected to a specific load. In fact, the joint design to be used, considering the operational conditions of loading, should be the design that ensures that the adhesive is stressed in the direction of his greater strength, thus avoiding failure. For a specific application, some adhesive joint configurations might be inappropriate, expensive to manufacture or make difficult the adherends' alignment. All these factors must be measured until a balance between practicality and performance is achieved [3]. The most commonly used adhesively-bonded joint configuration are: butt, lap, strap and tubular joints.

The butt joint concept features several possible configurations, each one with his own specific application. The plain butt joint is the easiest to manufacture, but it does not have the capacity to resist bending stresses, which translates in cleavage stresses in the adhesive. If the adherend has high thickness, geometric configurations in the joint may be considered for the purpose of improving the bending strength, which deviates cleavage stresses from the adhesive. The usual geometric modifications of butt joints are the scarf butt, double butt lap and tongue-and-groove configurations, represented in Figure 6. The tongue-and-groove butt joint is the one that achieves the highest performance due to its auto-alignment, granted by the modified geometry, and its capacity of retaining the adhesive inside, acting as an adhesive reservoir. However, it is necessary to consider that complex geometries often result in high manufacturing costs that could not be compatible with the application or project [4].

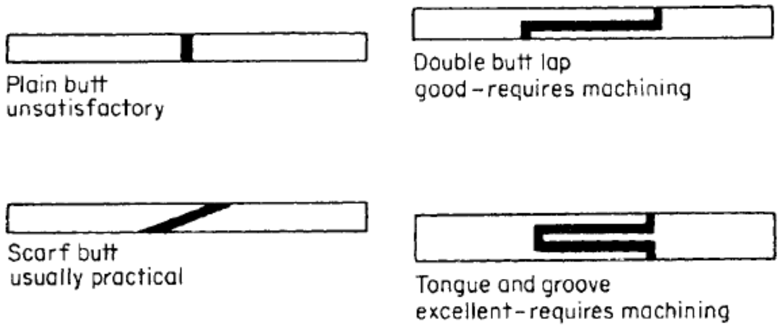

Figure 6 - Butt joint designs and configurations [3].

The lap joint is often used because the joint manufacturing process is simple and can be applied in circumstances where the adhesive is subjected mainly to shear, which is the setback of butt joints. However, due to the joint configuration, the forces applied to the adherend are non-collinear, meaning that peel stresses will arise at the overlap edges. There are several lap joint configurations optimized for peel stress reduction. The main types of lap joints are: plain lap, beveled lap, double lap and joggle lap joints, represented in Figure 7. Beveled lap joints, such as plain lap joints, are practical to manufacture and allow to greatly decrease stress concentrations at the ends of the adhesive. Double lap joints, although featuring a balanced construction, which drastically reduce the bending moment. However, the manufacturing process is more complex due to the two bonded surfaces. The joggle lap joint is the configuration which is more acceptable inside the concept since it does not require complex manufacturing processes and its geometry guarantees the collinearity between the two forces applied to the adherends [4].

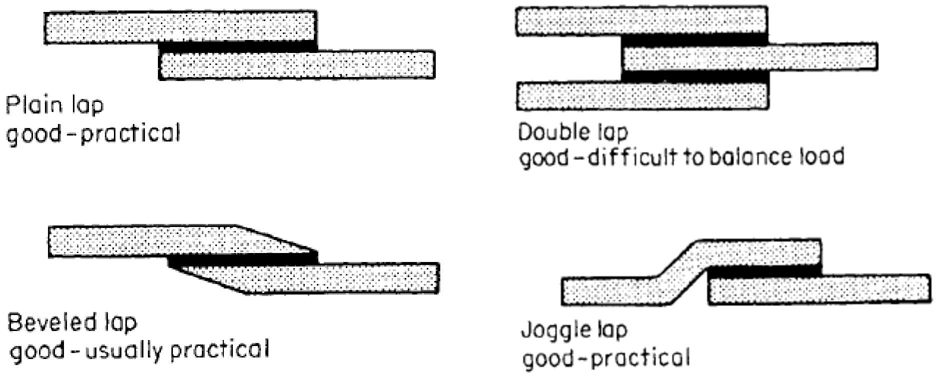

Figure 7 - Lap joint designs and configurations [3].

Strap joints require a laborious and complex manufacturing process with potential high costs associated. The concept has several possible configurations, such as single strap, double strap, recessed double strap and beveled double strap joints, represented in Figure 7. The single strap joint, similar to the plain lap joint, is subjected to significant peel stresses. Double strap joints, similarly to double lap joints, promote a practically inexistent bending moment at the cost of increasing the complexity of the manufacturing process. The recessed and beveled double strap joints are the ones with best performance, surpassing the previous two configurations, but they have a higher manufacturing cost, especially due to required machining operations. The strap concept is also often used as a patching solution in aluminium or composite structures in the aerospace industry [4].

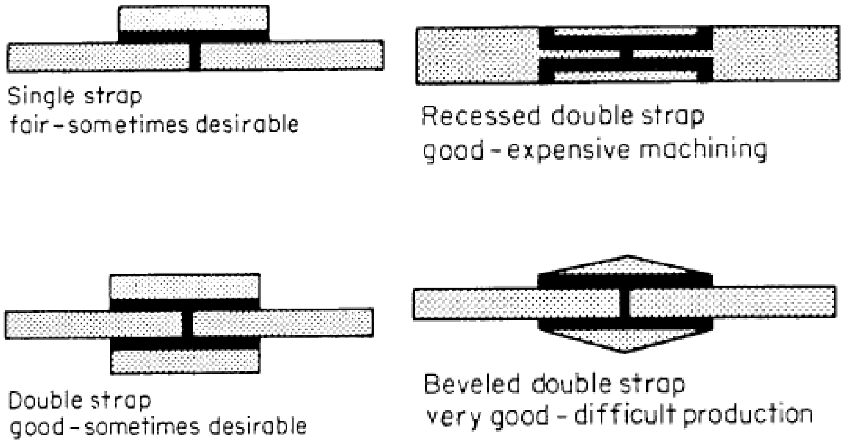

Figure 8 - Strap joint designs and configurations [3].

Tubular joints are commonly used when the design specifies connections between tubes or rods. Compared to plain butt joints, this configuration allows to define a larger resistant area, and to vary the overlapping length and its geometry. Moreover, the peeling phenomenon in the joint is significantly reduced, providing a higher joint performance. Still, the joint manufacturing process may be complex, depending on the geometry of the bonding area. Moreover, if machining operations are required, the entire process becomes more expensive [4].

The concept of angle and corner joints, compared to the concept of lap or cylindrical joints, is more complex, not only in the manufacturing process but mainly in the analysis of stresses. However, this concept allows configurations that minimize peel stresses and maximize the shear loads applied to the adhesive [4].

2.1.5 Structural adhesives

The main role of structural adhesives, in an adhesively-bonded joint, is to permanently hold together two or more adherends and endure the high stress operational loadings in service during his lifetime. Sometimes, the structural adhesive is responsible for keeping the structural integrity of the product intact and safe. They are often chemically created from thermosetting resins which require chemical crosslinking through both a curing agent or heat supply. Polyurethane, a high strength thermosetting elastomer, may also be defined as a structural adhesive [3].

Adhesive technology has several definitions, specifically for adhesive mixtures characteristics, that affect the adhesively-bonded joint performance and manufacturing process. The pot life or working life defines the application time limit of the adhesive when the resin and the cure agent are mixed, which may be short if the adhesive is to cure under room temperature, and besides, it is a key feature to be reckon with when using component adhesives, one-part. With regard to multiple component adhesives, two-part, the shelf life is the key feature to take into consideration since it defines the allowed time from the mixture to the adhesive application, depending on the storage conditions [4].

There are several families of polymeric resin that can formulate structural adhesives, the most relevant being: epoxies, phenolics, polyaromatic high temperature, polyurethanes and modified acrylics [3].

2.1.5.1 Epoxies

Epoxy based adhesives were introduced in the aerospace and automotive industries back in 1946 during the affirmation period of adhesively-bonded joints, providing a consolidated and reliable method to bond two or more materials. Epoxy adhesives are flexible since they easily bond different adherends, with the exception of polymers and elastomers, with low surface energy, and can be modified in order to achieve the required properties of the application [4].

Cured epoxies, with thermosetting molecular structures, feature excellent tensile and shear strength results, underperforming only when subjected to peeling stresses unless they are modified with a more resilient polymer. They also feature key characteristics to specific applications, such as excellent oil resistance, moisture and several solvents. Concerning the manufacturing process, they feature a low shrinkage ratio during the curing process, high resistance to creep when subjected to continuous stresses and do not release volatiles through evaporation during the curing process [4].

Commercial epoxies combine both an epoxy resin and a curing agent. The curing agent can be incorporated into the epoxy resin creating a component adhesive, or it can be supplied independently of the resin and then mixed with the resin just before application. Epoxies may be supplied in several states, as such: liquids, pastes, films or solids [4].

One-part adhesives cure under heat, while two-part adhesives may cure under room temperature or with high temperatures. Those that cure under high temperatures feature a higher crosslinking density and glass transition temperature than those cured under room temperature. High temperature curing epoxies feature high shear strength at high temperatures, and environmental resistance. However, they underperform when subjected to peeling stresses due to the lower tenacity. Room temperature cured epoxies, in some circumstances, may harden in seconds, but generally it takes them a period of time between 18 to 72 hours to harden. Yet, they can be hardened in short period of times if they are cured under higher temperature than room temperature [4].

Epoxy adhesives are often post-cured, granting the possibility of a better handling of the hardened joint without jeopardizing its structural integrity, therefore, improved handling strength. Epoxies can also be semi-cured, known as B-staged. In this stage, the adhesive features a fusible and soluble form which, combined with the additional heat generated from the curing process, the adhesive becomes fully cured. They are only one-part adhesive, feature several final shapes such as films, pre-forms or post-forms and promote the adhesive waste reduction, being these the main advantages of semi-cured epoxy adhesives [4].

One of the factors that makes epoxy adhesives so flexible is the amount of secondary ingredients that can be incorporated into the adhesive formulation. Reactive diluents ensure viscosity balance, mineral fillers reduce manufacturing process cost or modify the coefficient of thermal expansion, and fibrous fillers enhance thixotropy and cohesive strength. Epoxies may also be modified with other kinds of resins in order to accomplish the adhesive requirements for the specific application [4].

Several polymers blended and co-reacted with epoxy resins are often used to improve specific adhesive properties and may have various forms. Epoxy hybrid adhesives consists of epoxy resins that are toughened with elastomeric resins and alloyed blend, on which are frequently formulated into epoxy-phenolics, epoxy-nylon and epoxy-polysulfide adhesives [3].

2.1.5.2 Phenolics

Phenolic resins result from the phenol condensation and formaldehyde with the main application being wood bonding in plywood industries. Moreover, due to the high temperature resistance, high dimensional stability and low product cost, these adhesives are also being introduced in brake linings, abrasive wheels, sandpaper, and foundry moulds. The adhesive is often applied as an alcohol, acetone and water solution over a dry adherend and then cured under pressure and temperature. It may also be supplied as powder, to be dissolved into water, or film. Yet, the curing process should be performed under high temperature, approximately 140 °C, for several minutes. Phenol based adhesive joints feature good durability and environmental resistance [4].

Phenolic resins are also commonly known for being able to bond adherends of metal to wood. However, the bond between these two kinds of materials is brittle and tends to shatter if subjected to impact or vibration conditions. Nevertheless, phenolic adhesives are frequently modified with the incorporation of elastomeric resins that enhance the toughness and peel strength [4].

In order to overcome the limitations of phenolic-based adhesives and improve their range of applications, they are modified with the introduction of synthetic rubbers and thermoplastic materials. These hybrid adhesives are suitable for structural connections, being the most common the vinyl-phenolic, nitrile-phenolic and neoprene-phenolic [4].

2.1.5.3 Polyaromatic high temperature

The aromatic heterocycle polymer family, originally developed by aeronautic industries for high temperature applications, is commonly known for its outstanding thermal resistance. The most used resins are: polyimide, bismaleimide, polybenzimidazole and other high temperature. These high temperature resins are acknowledged as aromatic polymers due to its chemical structure, characterized as a closed ring which, when polymerized, features a polymeric structure defined as ladder [4].

While the thermal resistance is an appealing property, these resins are also known for their difficult manufacturing process, mainly due to the required aggressive solvents, suitable for high temperatures, which are hard to remove from the final product. Besides, the hardening process, through a condensation mechanism, releases water. The combination of the aggressive solvent and the water, resulting from the hardening process, often causes voids and bubbles in the adhesive [4].

These adhesives are supplied as a supported film, although some polyimide resins may be supplied as a solvent solution. Concerning the curing process, its recommended to use high temperature, around 290-340 °C, and high pressure, which should be initially slightly low, for crosslinking development, and finish with high pressure. Vacuum is often used for volatile elimination [4].

The modification of polyaromatic adhesives sometimes becomes a hindrance since, in the majority of the elastomeric additives, the adhesive service temperature is higher than the degradation point of the additive. However, researches have been conducted in order to enhance the tenacity with the incorporation of high temperature thermoplastics, for instance *polyarylene ether ketone* (PEK) and *polyaryl ether sulfone* (PES) [4].

2.1.5.4 Polyurethanes

Polyurethane adhesives can be supplied as a solid or dissolved in a solvent of one-part or two-part and, regarding the curing process, they may cure under room temperature or high temperature conditions, similarly to epoxy adhesives. Polyurethane adhesives feature high flexibility, which is a clear advantage considering epoxy adhesive properties [4], while also presenting acceptable shear and peel strengths.

Another distinctive feature of polyurethane adhesives is their tenacity, property granted by its chemical connections, and the resistance to low temperatures, better than most adhesives. Concerning the behaviour under low temperatures, polyurethane are only surpassed by silicon adhesives, which lack tensile strength in comparison with polyurethane adhesives [4].

Although polyurethane adhesives develop good chemical resistance, they provide no match compared to epoxy or acrylic adhesives. High temperature resistance is a feature that polyurethane adhesives are not strong at, being the maximum service temperature approximately 150 °C for particular formulations, while the most common formulations only allow 120 °C. Environmental conditions, such as moisture, are pretty harmful to polyurethane adhesives, substantially jeopardizing their structural integrity [4].

Concerning the applications, the high flexibility of polyurethane adhesives ensures the capacity to bond films, thin metal sheets and elastomers. The high wettability is a key feature of these adhesives since it grants the capacity to bond a wide range of adherends, including wood and polymers [4].

2.1.5.5 Modified acrylics

Modified acrylics, a branch of the acrylic family, are thermosetting systems, which are sometimes also referred as reactive acrylics in such way that a clear distinction can be made between the other acrylics used in pressure sensitive thermoplastic applications [4].

Thermosetting acrylics are two-part adhesives that feature high shear strength. The standard formulation of structural acrylics is similar to anaerobic adhesives. However, newly developed formulations are based on crosslinked polymethyl methacrylate grafted to vinyl terminated nitrile rubber [4].

Modified elastomers are often added into the acrylic formulation aiming to enhance its mechanical properties. However, these thermosetting adhesives, due to his nature, are quite stiff, with low peeling strength and also underperform in low temperature environments [4].

Regarding the joint manufacturing process, due to the fast curing process and high strength, the acrylic adhesive application can be highly automated. Modified acrylics feature high impact resistance, high shear strength, mainly between -100 and 120 °C, and high moisture resistance [4].

2.2 Strength prediction of bonded joints

The development of adhesively-bonded joints considers the selection of the structural adhesive as well as the adherends to be used, in line with the application to which the joint will be implemented. Joint configurations already known, deeply studied and consolidated, as well the loads, service stresses and potential failure modes, to which the joint will be subjected, are definitions with direct impact on the performance of the adhesively-bonded joints. However, all of these definitions may change after an analysis approach of the joint design in such way that the joint be fully optimized to the application itself.

The strength prediction of bonded joints breakthrough was first recorded in the middle of the 20th century with the introduction of analytical methods, based on the classic mechanic, which were not as representative of the real models, but for sure were better than the previous trial – and – error methods. These methods have been upgraded constantly, up today, increasing the complexity of the model in a more realistic perspective of the real models. Numerical methods were also introduced in strength prediction analysis granting the possibility of solving non-analytical applications, which have been mainly used within the adhesive joint development.

2.2.1 Analytical methods

The analytical analysis of adhesively-bonded joint began about eighty years ago based on Olaf Volkersen studies [9]. His analytical approximation is based on a conventual single lap joint (SLJ) model, represented in Figure 9 which, despite being a simple and limited method, allows the determination of shear stresses. The shear stresses are not uniform along the bonded length, achieving its maximum peak values at the overlap edges and the minimum values within the core of the adhesive.

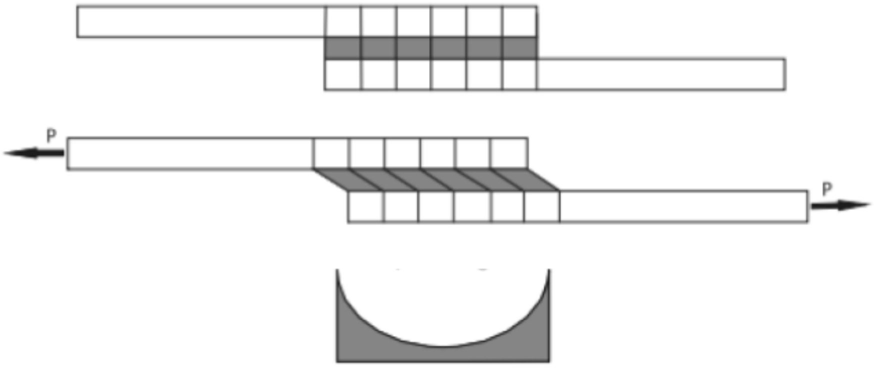

Figure 9 – Representation of unloaded specimen (up), loaded specimen (middle) and adhesive shear stress distribution (down) [4].

Goland and Reissner's [10] developed Volkersen method considering that the load applied on each adherend is not collinear, as represented in Figure 10, therefore creating a bending moment that promotes the joint transverse deflection. The displacements are no longer proportional to the load, resulting in a geometrical non-linearity. Overall, the analytical results are very similar with Volkersen method in regard to the shear stresses. However, this upgraded formulation also allows the determination of peel stresses.

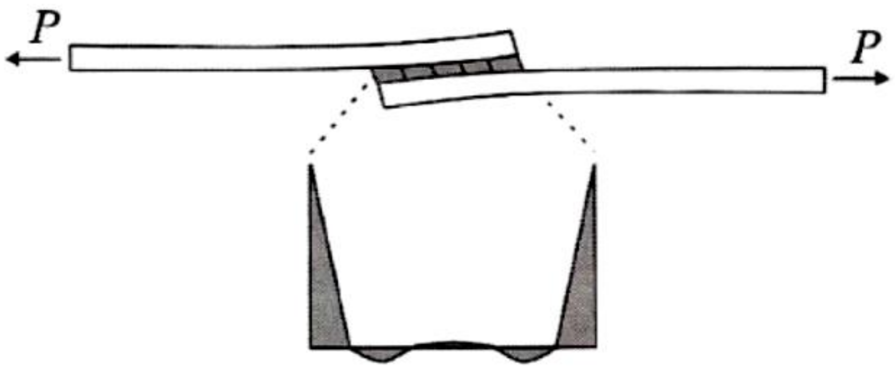

Figure 10 - Peel stress distribution representation considering Goland and Reissner's approach [4].

Hart-Smith analysis [11] goes further away and considers that, beyond elastic deformation, the adhesive and adherend are also subjected to plastic deformations, represented in Figure 11. This method establishes that the adhesive plasticity enhances the strength of a joint in comparison with an elastic analysis since, when the material plasticizes, a stress redistribution occurs, in such way that the failure takes longer to manifest. The model, considered as elasto-plastic, reflected that the actual shape of the adhesive *P*-*δ* curve is less important than the area underneath, which represents the energy dissipation. Therefore, an elastic-perfectly plastic response was considered.

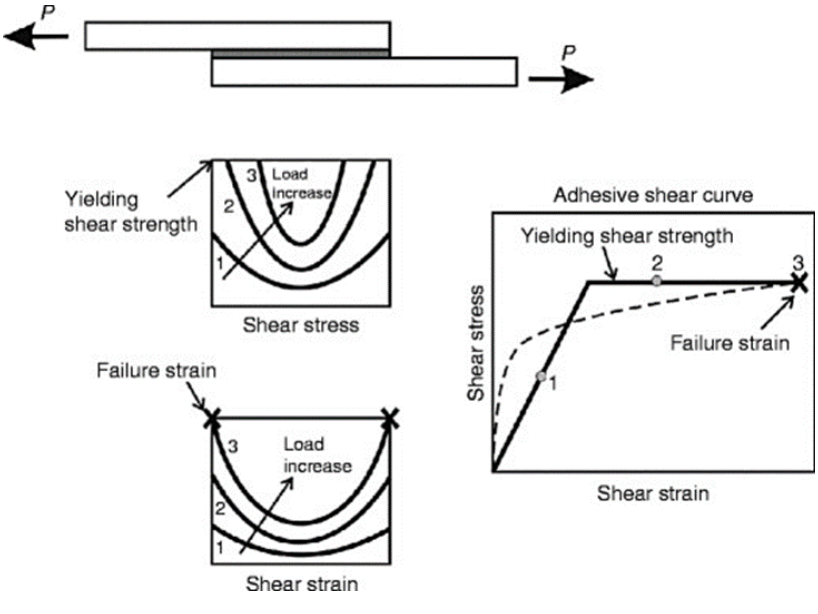

Figure 11 - Hart-Smith analysis [2].

Renton and Vinson investigations [12] increased the complexity of the Goland and Reissner's model, by using the balanced SLJ boundary conditions for the overlap bending moment. However, they included thermal strains into the formulation and the adhesive layer was modelled as an individual block. This model configuration enables the adhesive shear stress, at the edges of the overlap, to drop quickly to zero.

Ojalvo and Eidinoff [13] incorporated a complete description for the adhesive shear strain that allows for a linear variation across the adhesive thickness, without considering the adherend shearing. They also showed that shear stresses could feature a significant variation across the overlap, at the joint ends.

Allman [14] and Chen and Cheng [15], both considering two dimensional (2D) models based on the elastic theory, assumed a linear variation of peel stresses and constant shar stress across the adhesive thickness. Adams and Mallick [16], and then Zhao and Lu [17], developed models in which both adhesive and adherends are described as elastic media, being able to be applied to joints with thick adhesives, although analytical solutions for composite joints are very complex with this model [2].

Yang and Pang [18] further developed the SLJ model incorporating asymmetrical laminates, and all three stress components in the adhesive are obtained through Fourier series approach.

Analytical methods were further developed by several authors, not only for SLJ but also for other joint configurations. Despite the substantial advances in analytical methods, the design analysis for wider range of applications, capable of modelling non-linear adhesive behaviour, is still a major limitation for these methods. To overcome the analytical methods limitations, general structural analysis packages were developed, with the restriction of just one overlap region. Crocombe [19] was one of the pioneers that introduced the newly developed package, known as SAAS (Stress Analysis for Adhesive Structures), on which FE (Finite Element) principles were implemented [5].

2.2.2 Numerical methods

Numerical methods emerged from the need to predict the behaviour of new and complex adhesives, which require a high complex analysis that might require non-analytical solutions. Under these circumstances, numerical methods are the recommended methods to follow. The main strength prediction techniques among the numerical methods are: continuum mechanics, fracture mechanics, cohesive zone models, damage mechanics and the extended finite element method.

Continuum mechanic approach defines the maximum value of stress, strain or strain energy, predicted by FE analysis or analytical methods, and relates them with the corresponding material allowable values to access failure [20]. By ignoring all the other principal stresses, initially, the maximum principal stress was used for the strength prediction of brittle materials, since it is the major responsible for the failure of this type of materials. Adams et al. [21] used this criterion with success, thus consolidating the method. Concerning the criterion, special care must be taken, mainly due to the singular stresses at the re-entrance corners of the joint. Granted that, a small amount of rounding at the adherend corner eliminates the singularity point, thus redistributing the stresses in that area, with direct impact in the joint strength.

The fracture mechanics approach was developed in response to the limitations of the continuous mechanics approach, which assumes that the structure and its materials are continuous, due to the defects in the structure or in the two materials, namely, in the re-entrant corner, becoming a source of structural discontinuities. Thus, the fracture mechanics approach is well accepted since the stresses, calculated through the continuum mechanics approach, are singular at the crack tip.

Linear elastic fracture mechanics (LEFM) based approach had a great success some decades ago, though its application had limitations due to the material elastic behaviour restrictions. Furthermore, modern toughened adhesives often develop plastic zones even larger than the adhesive thickness, requiring a suitable approach to overcome the previous approach limitations. Barenblatt [22, 23] and Dugdale [24] developed the concept of cohesive zone to define damage under static load, at the cohesive process zone, ahead of the apparent crack tip. The cohesive zone model (CZM) approach was then improved and tested to simulate crack initiation and propagation even in composite delamination [25]. The CZM approach is based on spring [26] or more frequently cohesive elements [27], connecting 2D and 3D (three dimensions) elements of structures, thus being easily incorporated in FE software to model the fracture behaviour in several materials. The concept of the CZM approach is based on the presumption that the fracture can be artificially introduced in structures, in which the damage growth is permitted by the introduction of a potential discontinuity in the displacement field.

Damage mechanics approach is based, mainly, on a damage parameter, established to redefine the constitutive response of the materials, through decreasing stiffness or strength, aiming to recreate the severity of the damage in the material, during its loading. Several advanced studies have been conducted, reporting the damage parameter defined as a degradation property, often found in thin adhesive bonds [28], composite delaminations or matrix failure [29], where this parameter can be established as a damage evolution law to model pre-cracking damage or crack growth. The damage variables can be categorized in two main groups, one that predicts the amount of damage by redefinition of the material constitutive properties, and the other considering variables linked to a specific kind of damage, such as porosities. The damage mechanics approach defines the damage growth as a function of the load for static modelling [30] or cycling count for fatigue analysis [31]. Comparing with the fatigue analysis in CZM approach, the damage mechanics approach does not define a clear distinction between the fatigue initiation and propagation phases [28]. Nevertheless, it may be applicable if the damage is more widespread or the failure path is unknown [32].

The eXtended Finite Element Method (XFEM), recently developed, is an extension of the FE method whose fundamental features were firstly introduced in early 90s by Belytschko and Black [33]. Unlike CZM, XFEM does not require the crack to follow a predefined path. Instead, it simulates the crack onset and growth, through an arbitrary path, without the requirement of the mesh matching the geometry discontinuities, neither remeshing near the crack [34]. The concept is based on unit partition, which consists of the introduction of local enrichment functions for nodal displacements, to model crack growth and separation between crack faces [35]. As the crack grows, it constantly changes position and orientation, due to loading conditions and, in these circumstances, the XFEM algorithm defines the necessary enrichment functions for the nodal points of the FE around the crack path/tip. The damage law used in XFEM is based on the bulk strength of the materials for the initiation of damage and on the strain for the assessment of failure.

2.3 Fracture toughness tests

The performance of adhesives, whether in bulk form or mainly when applied into joints, relies on a set of properties generally divided as: physical, thermal and mechanical properties. Physical and thermal properties are connected, intrinsically, to the nature of the adhesive, while the assessment of the mechanical properties is based on performing tests [4].

Fracture toughness tests are carried out on bulk adhesive specimens and also on adhesively-bonded joints, for several purposes. Bulk adhesive specimens are often manufactured for the fracture toughness test as part of the product development and validation. The manufacturing process depends on the physical form of the adhesive, since the process features significant differences if the adhesive is provided in paste or adhesive film. Also, the process is strict and complex since voids or mold empty spaces are not acceptable [2].

Adhesively-bonded joints with an adhesive thickness range between 0.1 – 2.0 mm are preferred to study the fracture toughness. The adhesive, as a part of the cured joint, may feature different properties relative to the cured bulk specimen, mainly due to the cure process conditions, which may be different. Moreover, the properties change between adhesives in bulk and as a joint. The behaviour of the adhesive in a joint is affected by the adherends nearby, therefore limiting the size of the plastic zone forming at the crack tip, thus limiting the toughness of the joint. Testing adhesives as part of an adhesive joint system grants access to further analysis related with the potential locations of the failure path, as might be, for instance, cohesive in the adhesive, near the interface or through the adherend. These potential scenarios for the failure path, may result on different measured fracture resistance, thus making these studies indeed relevant. Cracks in bulk adhesive specimens always tend to grow under mode I tensile conditions. However, in adhesively-bonded joint specimens, the direction of the crack and consequent failure path is often constrained, resulting on cracks propagating under mixed mode and mode II loading conditions [2].

There are two traditional modes to which the adhesively-bonded joint is generally subjected during the loading conditions, mode I and mode II, characteristic of pure tensile and pure shear loadings, respectively, as shown in Figure 12.

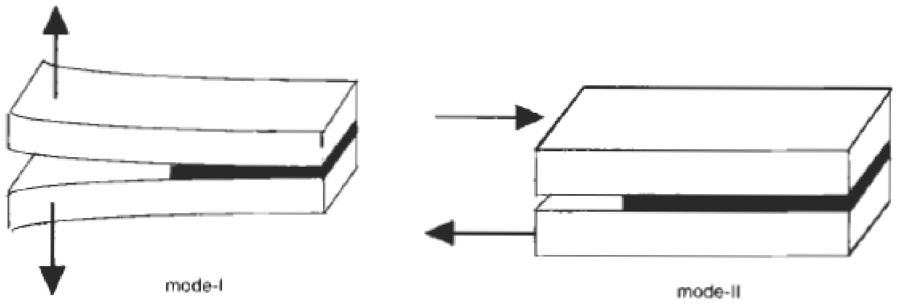

Figure 12 – Representation of pure model I (tensile) and pure model II (shear) [36].

In only a few applications, adhesively-bonded joints are subjected only to tensile or shear stresses. In practice, the combination of both stresses corresponds to the most common situation. The combination of mode I and II is generally defined as mixed mode, where both stresses, tensile and shear, are present in the adhesively-bonded joint, during loading conditions. The existence of a mixed mode loading condition significantly increases the complexity of the strength prediction of adhesively-bonded joints.

The mode III is related with the tearing loading to which the adhesively-bonded joint is subjected. However, this type of loading is not often used for common applications of the adhesively-bonded joints.

2.3.1 Tensile tests (pure mode I)

Mode I fracture resistance assessment of adhesive joints is mostly performed by the well-known and consolidated double cantilever beam (DCB) test, through the mode I energy release rate (G_{IC}) measurement. The test was originally developed and standardized by ASTM D3433-99 [37] and then improved, over the years, by BSI 2001 [38] and ISO 25217 [39] standards. The DCB adhesive joint test specimen consists of two adherends (double cantilevers) bonded together through a thin layer of adhesive forming the joint [2], as shown in Figure 13.

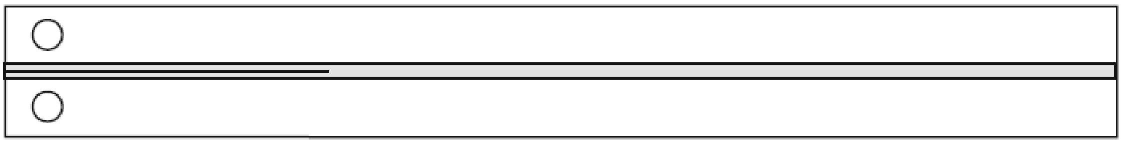

Figure 13 – Mode I DCB adhesive joint specimen [2].

The DCB configuration requires an initial crack length, defined as a_0, without adhesive. The setup of the DCB test needs a self-alignment fixture system, to ensure a uniaxial state of traction. The speed of the test, as the ASTM D3433-99 [37] standard describes, must be continuous one minute after the trial initiates, so that the pre-crack can develop. It is recommended a speed between 0.5 to 3 mm/min, depending on the joint geometry and material properties. While the trial is carried out, the load and displacement values are recorded for the correspondent length of the crack, defined as *a*, is correlated with the test data [4].

The analytical approach of Branco [40] for the DCB test was based on classic mechanics, where the adherends were considered as clamped beams to obtain the strain energy through the flexion and shear stress from both adherends. However, this approach was considered as limited due to the restrict beam movement, since it does not account for the rotation at the end of the crack. Kanninen [41], in order to incorporate the rotation effect into the formulation, used a beam model over an elastic foundation, known as corrected beam model, considering only the flexure stress. The thickness of the adherends, considering the metallic base material, is an important aspect to take into account, since in case of plasticization of the adherends during the test, which is a scenario to be avoided, the results become compromised. The ASTM D3433-99 standard [37] foresees the plasticization hypothesis and establishes, for uniform and symmetrical metallic adherends, a minimum thickness value based on the metal properties and adhesive strength [4].

There is also another test, normalized by the ASTM D3433-99 [37] standard, appropriate for the mode I fracture resistance assessment, which is the Contoured Double-Cantilever Beam (CDCB) test, also described as Tapered Double-Cantilever Beam (TDCB) test, represented in Figure 14. The main attribute of the CDCB test is the possibility to obtain the mode I energy release rate (G_{IC}) independently of the crack length (*a*). However, the complexity of the adherends manufacturing process is a clear disadvantage, if compared with the traditional DCB test, especially if the adherends have composite as base material [4].

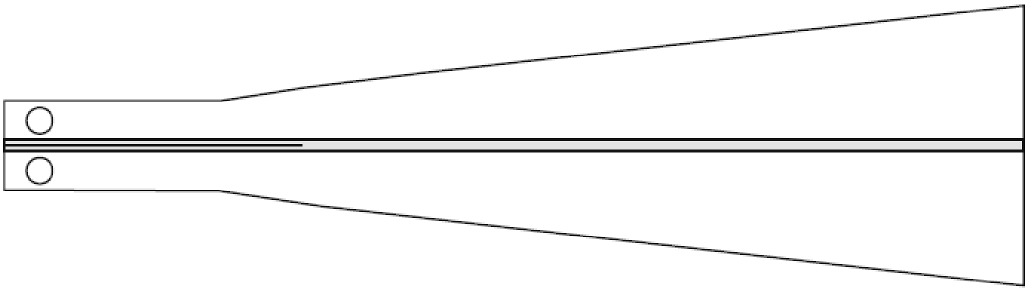

Figure 14 - Mode I TDCB adhesive joint specimen [2].

2.3.2 Shear tests (pure mode II)

Mode II fracture resistance assessment, unlike the mode I, is yet to be standardized, as for the moment, only scientific articles are available. The researches available are based on tests performed to characterize and evaluate the interlaminar mode II fracture, mainly in composite materials. As for the tests used in these studies, the highlight belongs to the End Notched Flexure (ENF) and other two less optimized test, the End Loaded Split (ELS) and the Four-Point End Notched Flexure (4ENF), are represented in Figure 15 [4].

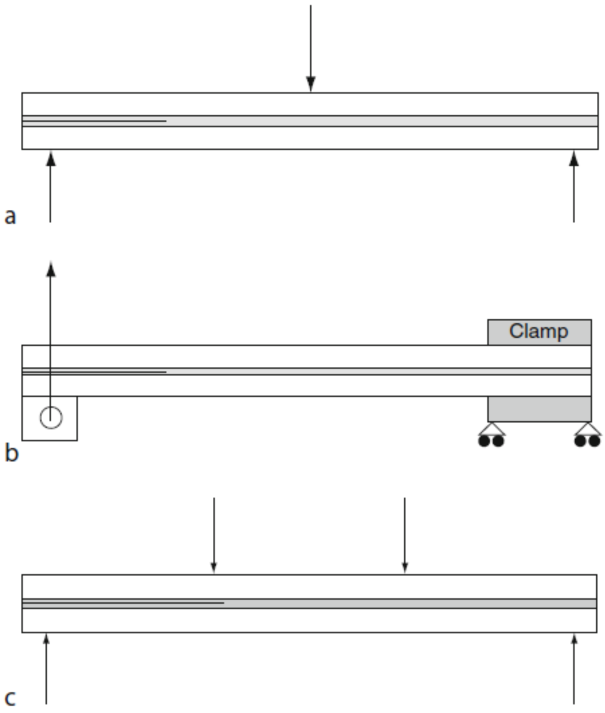

Figure 15 – Pure mode II shear tests: (a) ENF; (b) ELS; (c) 4ENF [2].

The ELS test features a few hindrances for the assessment of the mode II energy release rate (G_{IIC}), mainly due to large displacements, which are characteristic of the test, and sensitivity to tightening conditions. The 4ENF, being a more complex test, requires more sophisticated setup and monitoring devices. Moreover, it is also affected by friction in the pre-crack area. All these factors inevitably become obstacles to the application and development of the test. The ENF is certainly the most embraced test, among researchers, due to its simplicity and accuracy of the obtained data for the material characterization in mode II [4].

The analytical approach related with the ENF test is often based on the classic beam theory, where both adherends, at the crack region, act as independent beams, each one enduring half of the load applied [4].

The assessment of the G_{IIC} is still a difficult task, to be overcome, for all the designed tests, without exception. All mode II tests are limited by difficulties in measurement of a during the crack propagation. The localization of the crack propagation, developed by the shear stress and caused by crack growth without a clear opening, is very difficult to detect. Another major limitation of the fracture assessment in mode II is related with the dimensions, often not negligible, of the fracture process zone (FPZ). The FPZ is defined as the area of damaged material, through inelastic processes, for instance, microfracture or microstrain, and is located at the crack end. Furthermore, the energy release at the FPZ may not be neglected. In these scenarios, an equivalent crack length should be considered [4].

Crack length monitorization difficulties plus FPZ hypothesis with non-negligible dimensions are definitively limitations that compromise the data analysis, thus resulting in inconsistent results. Still, alternative approaches on how to handle the data have been developed and the concept of equivalent crack introduced. This new method of data processing does not require the measurement of the crack length during its propagation, which solves one of the major issues, and it is based only on the material flexibility [4].

2.4 Single-Leg Bending (SLB) test

Adhesively-bonded joints are often subjected to the combination of tensile and shear stresses, which is defined as mixed mode stress state. Fracture resistance assessment tests need to consider this combination of mode I and II, however they are yet to be standardized. New tests have been developed through advanced researches, from where the Mixed-Mode Flexure (MMF) test resulted, which has similarities with the ENF test. Another alternative test, based on the traditional DCB, is the Asymmetric DCB (ADCB) test which, through different adherend thickness, develops the combination of modes I and II. However, the most relevant test is certainly the SLB test which, compared to the other two, is the one featuring more potential for the fracture resistance assessment considering the mixed mode [4].

2.4.1 Test characterization

The SLB test, as previously introduced, was designed to assess the fracture resistance under mixed-mode conditions. The SLB specimen consists of two adherends, with different lengths, being the upper adherend longer than the lower, both bonded together parallelly through an adhesive, as depicted in Figure 16. During the specimen preparation, the a_0 is defined and introduced into the specimen end.

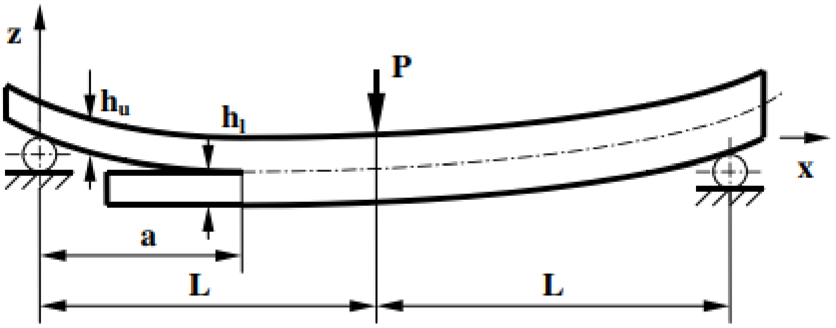

Figure 16 - SLB test geometry representation [42].

Several geometrical parameters of the SLB specimen may be configured depending on the application, for instance, the adherends thickness, which can be different between the upper and lower adherend, adhesive thickness, and length and width of the adherends. However, there are recommendations, related to the specimen design, which should be considered. For example, the ratio between the initial crack length and the distance between the roller and the applied load (*L*) must be over 70% (≥ 70/100), thus establishing a sufficient length for accurate data gathering and avoiding unstable crack propagation [43].

In which regards to the test itself, the specimen is supported by two rollers, one of which is in contact with the upper adherend and the other with the lower adherend. The load is applied in the upper adherend, at centre span, thus developing compression stresses over the adherend, decreasing along way through the thickness of the adhesive and lower adherend. During the test, *a* is measured from the centreline of the leftmost roller till the crack tip (Figure 16), and it is registered until the crack reaches the loading line. At this point, the test is considered as finished due to the interference caused in the G_{IC} and G_{IIC} readings by the compression stresses.

The SLB test is considered as an approachable test that does not require complex procedures nor equipment since, for adhesive laboratories, the three-point bend fixtures are more common than the carriages often used to perform, for instance, ELS tests. Nonetheless, for the methods that require the measurement of the crack length, which must be accurate for the assessment of the energy release rate, a camera with high resolution is necessary. Otherwise, misreading the crack length data could compromise the accuracy of the results. Another important aspect to be reckoned is the beam foreshortening scenario. This test should use rollers instead of fixed supporters, especially when testing flexible adherends, otherwise the frictional sliding of the adherends over the supports may introduce undesirable interference into the results, thus reducing the compliance of the specimen at higher deflexions [44].

2.4.2 Methods to estimate the fracture toughness

Through advanced adhesive studies, several methods for fracture toughness assessment were developed. The traditional method considers the measurement of the crack length, and there are several possible models, depending on the configuration and application of the joint. Yet, due to the inherent difficulty in measuring the crack length, a new method has been developed that considers the equivalent crack length, thus avoiding its measuring. Recently, a new method defined as *J*-integral method was developed and offers a new approach to the fracture toughness assessment.

2.4.2.1 Methods that require the crack length monitoring

There are several models developed, yet, only five will be demonstrated. These models are differentiated by the analytical approach to estimate the G_{IC} and G_{IIC}. Moreover, some methods using the same analytical approach may have different simplifying assumptions and complexity.

2.4.2.1.1 Model 1 – Oliveira et al.

The method behind Oliveira et al. [45] model is based on the classic beam theory and it results in obtaining the complete *R* curve. According to the Timoshenko beam theory, the compliance equation of the specimen is obtained through the strain energy:

$$U = \int_0^L \frac{M_f^2}{2E_L I} dx + \int_0^L \int_{-h}^{h} \frac{\tau^2}{2\mu_{LR}} B dy dx \,, \tag{1}$$

where M_L is defined as the bending moment, I as the second moment of area and

$$\tau = \frac{3}{2}\frac{V_i}{A_i}\left(1 - \frac{y^2}{c_i^2}\right), \tag{2}$$

considering A_i, c_i and V_i as the cross-section area, half-thickness of the beam and the transverse load of the segment *i* ($0 \le x \le a$, $a \le x \le L/2$ or $L/2 \le x \le L$), respectively.

By the Castigliano theorem, the beam compliance at the loading point for *a*, is defined as

$$C = \frac{28a^3 + L^3}{32E_L Bh^3} + \frac{3(a+L)}{20\mu_{LR} Bh}. \tag{3}$$

The initial crack length (a_0) and the beam compliance (C_0) can be used in Eq. (3) to assess the flexural modulus:

$$E_f = \left(C_0 - \frac{3(a_0 + L)}{20\mu_{LR}Bh} \right)^{-1} \frac{28a_0^3 + L^3}{32Bh^3}. \tag{4}$$

Based on this approach, the measurement of the longitudinal modulus for each specimen is no longer required.

The fracture toughness assessment, in mixed mode conditions, can be established by the Irwin-Kies [46] equation:

$$G_T = \frac{P^2}{2B}\frac{dC}{da}, \tag{5}$$

which, for SLB test, gives

$$G_T = \frac{21P^2a_{eq}^2}{16E_fB^2h^3} + \frac{3P^2}{10\mu_{LR}B^2h}. \tag{6}$$

Considering the partitioning method, which is based on the beam theory, proposed by Szekrényes and Uj [42], the mixed mode components, mode I and II, can be defined as:

$$G_I^{SLB} = \frac{12P^2a_{eq}^2}{16E_fB^2h^3} + \frac{3P^2}{10\mu_{LR}B^2h}, \tag{7}$$

$$G_{II}^{SLB} = \frac{9P^2a_{eq}^2}{16E_fB^2h^3}. \tag{8}$$

2.4.2.1.2 Model 2 – Szekrényes and Uj

Through the linear beam theory, which considers the concept of transversal shear and the effects of an elastic base, Szekrényes and Uj [42] deduced the energy release rate for both mixed mode components, mode I and II, thus establishing the model for the SLB specimen. The beam compliance is obtained based on the studies of Ozdil et al. [47] from where the following expression was deduced, for the ENF specimen, applying the Timoshenko beam theory:

$$C = \left[\frac{2L^3d_{11,2} + a^3\left(d_{11,1} - d_{11,2}\right)}{12} + \frac{2La_{55,2} + a\left(a_{55,1} - a_{55,2}\right)}{4k} \right], \tag{9}$$

wherein *k* is the estimated value for the shear correction factor, defined as 5/6. By differentiating the beam compliance, function of the crack length, the mixed mode fracture toughness can be defined, generally, as

$$G_{I/II} = \frac{P^2}{2b}\frac{dC}{da}, \tag{10}$$

thus, resulting into

$$G_{I/II} = \frac{P^2}{8b}\left[a^2\left(d_{11,1} - d_{11,2}\right) + \frac{\left(a_{55,1} - a_{55,2}\right)}{k}\right]. \tag{11}$$

The bending and shear beam compliances of the cracked and uncracked portions of unidirectional and symmetrical SLB specimen can be written as:

$$d_{11,1} = \frac{12}{bh^3E_{11}}\;;\; d_{11,2} = \frac{3}{2bh^3E_{11}}\;;\; a_{55,1} = \frac{1}{bhG_{13}}\;;\; a_{55,2} = \frac{1}{2bhG_{13}}. \tag{12}$$

Considering the already deduced Eq. (11) with the bending and shear beam compliance factors, defined in Eq. (12), the simplified fracture toughness expression can be defined as

$$G_{I/II} = \frac{21P^2a^2}{4b^2h^3E_{11}} + \frac{P^2}{4b^2hkG_{13}} + \frac{P^2a^2}{4b^2h^3E_{11}}\left[5.42\left(\frac{h}{a}\right)\left(\frac{E_{11}}{E_{33}}\right)^{\frac{1}{4}} + 2.45\left(\frac{h}{a}\right)^2\left(\frac{E_{11}}{E_{33}}\right)^{\frac{1}{2}}\right]. \tag{13}$$

Moreover, in which regards the mode-partitioning concept, the mode-mixity analysis is based on Williams [48] method, improved by combining the effects of traverse shear and the Winkler-Pasternak foundation analysis [47, 49]. However, only unidirectional specimens with a midplane crack may be considered for further analysis. The beam compliance expressions for the upper and lower arms, represented in Figure 17, are:

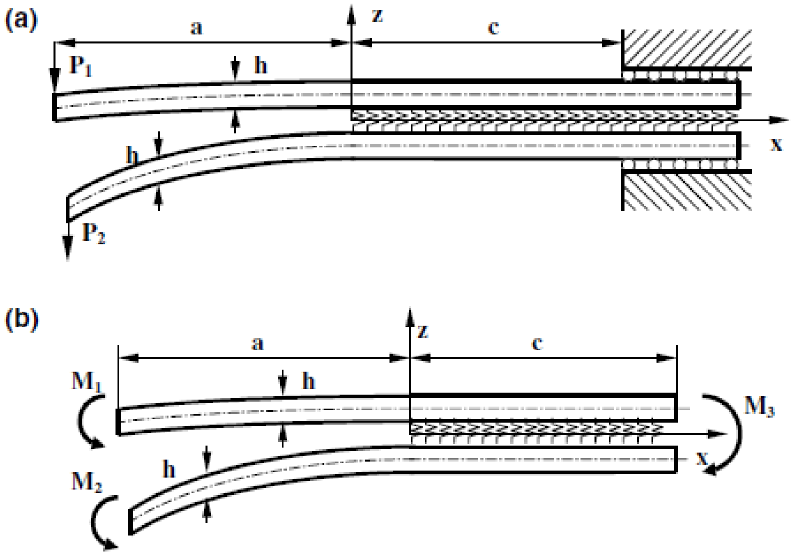

Figure 17 - Reduction scheme for mixed mode partitioning [42].

$$C_1 = \frac{7a^3 + L^3}{2bh^3 E_{11}} + \frac{\left(L^3 - a^3\right)P^2}{2bh^3 E_{11} P_1} + \frac{L\left(P_1 + P_2\right) + a\left(P_1 - P_2\right)}{bhkG_{13} P_1} + \frac{a^3\left(P_1 - P_2\right)}{2bh^3 E_{11} P_1} f_{W1}, \tag{14}$$

and

$$C_2 = \frac{7a^3 + L^3}{2bh^3 E_{11}} + \frac{\left(L^3 - a^3\right)P_1}{2bh^3 E_{11} P_2} + \frac{L\left(P_1 + P_2\right) + a\left(P_2 - P_1\right)}{bhkG_{13} P_2} + \frac{a^3\left(P_2 - P_1\right)}{2bh^3 E_{11} P_2} f_{W1}, \tag{15}$$

where

$$f_{W1} = 2.71\left(\frac{h}{a}\right)\left(\frac{E_{11}}{E_{33}}\right)^{\frac{1}{4}} + 2.45\left(\frac{h}{a}\right)^2\left(\frac{E_{11}}{E_{33}}\right)^{\frac{1}{2}} + 1.11\left(\frac{h}{a}\right)^3\left(\frac{E_{11}}{E_{33}}\right)^{\frac{3}{4}}. \tag{16}$$

The fracture energies yield, deduced through Eq. (10), can be expressed as:

$$G_1 = \frac{21P_1^2 a^2}{4b^2 h^3 E_{11}} - \frac{3P_1 P_2 a^2}{4b^2 h^3 E_{11}} + \frac{P_1\left(P_1 - P_2\right)}{4b^2 hkG_{13}} + \frac{P_1\left(P_1 - P_2\right)a^2}{4bh^3 E_{11}} f_{W2}, \tag{17}$$

and

$$G_2 = \frac{21P_2^2 a^2}{4b^2 h^3 E_{11}} - \frac{3P_1 P_2 a^2}{4b^2 h^3 E_{11}} + \frac{P_2\left(P_2 - P_1\right)}{4b^2 hkG_{13}} + \frac{P_2\left(P_2 - P_1\right)a^2}{4bh^3 E_{11}} f_{W2}, \tag{18}$$

where

$$f_{W2} = 5.42\left(\frac{h}{a}\right)\left(\frac{E_{11}}{E_{33}}\right)^{\frac{1}{4}} + 2.45\left(\frac{h}{a}\right)^2\left(\frac{E_{11}}{E_{33}}\right)^{\frac{1}{2}}. \tag{19}$$

Considering

$$M_1 = P_1 a\,,\ M_2 = P_2 a \text{ and } M_3 = M_1 + M_2\,, \tag{20}$$

as bending moments at the crack tip, the sum of Eq. (17)and (18) can be written as

$$G_T = \frac{21\left(M_1^2 + M_2^2\right) - 6M_1 M_2 + \left(M_1 - M_2\right)^2\left(f_T + f_{W2}\right)}{4b^2 h^3 E_{11}}, \tag{21}$$

wherein

$$f_T = \frac{1}{k}\frac{E_{11}}{G_{13}}\left(\frac{h}{a}\right)^2. \tag{22}$$

Ducept et al. [50] proposed the decomposition of the equivalent bending moments as

$$M_1 = M_I + M_{II} \text{ and } M_2 = \alpha M_I + \varphi M_{II} . \tag{23}$$

Considering a hypothetical scenario of pure mode II, where the upper and lower specimens arms have the same curvature,

$$\frac{12M_{II}}{bh^3E_{11}} = \frac{12\varphi M_{II}}{bh^3E_{11}} , \tag{24}$$

from which ϕ is defined as 1. Therefore, combining the Eq. (23) into (21), grants the separation of the term, containing the product M_IM_{II}

$$G^*_{I/II} = \frac{9M_IM_{II}\left(1+\alpha\right)}{b^2h^3E_{11}} . \tag{25}$$

To cancel this term, α is defined as -1, which enables the definition of both component modes, I and II:

$$G_I = \frac{M_I^2\left(12 + f_T + f_{W2}\right)}{b^2h^3E_{11}} \tag{26}$$

and

$$G_{II} = \frac{9M_{II}^2}{b^2h^3E_{11}} . \tag{27}$$

Thus rearranging the Eq. (23), the following equations can be established:

$$M_I = \left(\frac{M_1 - M_2}{2}\right) \text{ and } M_{II} = \left(\frac{M_1 + M_2}{2}\right). \tag{28}$$

According to Eq. (26) and (27), it is reasonable to assume that the transverse shear and the elastic foundations only contributes for the mode I component due to the fact that the transverse shear does not change the curvature of the unidirectional specimen arms.

As for the SLB specimen application, the reduced bending moments at the crack tip are

$$M_1 = 0 \text{ and } M_2 = \frac{Pa}{2} , \tag{29}$$

therefore, using the Eq. (26) and (27), the G_I^{SLB} and G_{II}^{SLB} can be expressed as

$$G_I^{SLB} = \frac{12P^2a^2}{16b^2h^3E_{11}} + \frac{P^2}{16b^2hkG_{13}} + \frac{P^2a^2}{16b^2h^3E_{11}}\left[5.42\left(\frac{h}{a}\right)\left(\frac{E_{11}}{E_{33}}\right)^{\frac{1}{4}} + 2.45\left(\frac{h}{a}\right)^2\left(\frac{E_{11}}{E_{33}}\right)^{\frac{1}{2}}\right] \tag{30}$$

and

$$G_{II}^{SLB}=\frac{9P^2a^2}{16b^2h^3E_{11}}\,. \tag{31}$$

2.4.2.1.3 Model 3 – Ye Zhu

The Zhu [51] approach is based on the Szekrényes and Uj [42] method, which considers the Euler-Bernoulli and Timoshenko beam theories, combined with the Winkler-Pasternak foundation analysis, the Saint-Venant effect analysis at the crack tip and a crack tip shear deformation analysis to assess the compliance of a SLB specimen, with an initial crack length, at the middle plane of the adhesive. The beam compliance equation can be expressed as:

$$\begin{aligned}C=&\frac{7a^3+2L^3}{8bh^3E_{11}}+\frac{a+2L}{8bhkG_{13}}+\frac{a^3}{8bh^3E_{11}}\left[0.98\left(\frac{h}{a}\right)\left(\frac{E_{11}}{E_{33}}\right)^{\frac{1}{2}}+0.43\left(\frac{h}{a}\right)^2\left(\frac{E_{11}}{E_{33}}\right)\right]\\&+\frac{1}{\pi}\frac{3a^2}{4bh^2E_{11}}\left(\frac{E_{11}}{E_{33}}\right)^{\frac{1}{2}}\frac{a^3}{8bh^3E_{11}}\left[\begin{aligned}&5.07\left(\frac{h}{a}\right)\left(\frac{E_{11}}{E_{33}}\right)^{\frac{1}{4}}+8.58\left(\frac{h}{a}\right)^2\left(\frac{E_{11}}{E_{33}}\right)^{\frac{1}{2}}\\&+2.08\left(\frac{h}{a}\right)^3\left(\frac{E_{11}}{E_{33}}\right)^{\frac{3}{4}}\end{aligned}\right]\end{aligned} \tag{32}$$

where the component modes, I and II, are given by

$$G_{I}^{SLB}=\frac{12P^2a^2}{16b^2h^3E_{11}}\left[\begin{aligned}&1+0.85\left(\frac{h}{a}\right)\left(\frac{E_{11}}{E_{33}}\right)^{\frac{1}{4}}+0.71\left(\frac{h}{a}\right)^2\left(\frac{E_{11}}{E_{33}}\right)^{\frac{1}{2}}\\&+0.32\left(\frac{h}{a}\right)\left(\frac{E_{11}}{E_{33}}\right)^{\frac{1}{2}}+0.1\left(\frac{h}{a}\right)^2\left(\frac{E_{11}}{E_{33}}\right)\end{aligned}\right] \tag{33}$$

and

$$G_{II}^{SLB}=\frac{9P^2a^2}{16b^2h^3E_{11}}\left[1+0.22\left(\frac{h}{a}\right)\left(\frac{E_{11}}{E_{33}}\right)^{\frac{1}{2}}+0.048\left(\frac{h}{a}\right)^2\left(\frac{E_{11}}{E_{33}}\right)\right]. \tag{34}$$

2.4.2.1.4 Model 4 – W.S. Kim et al.

Kim et al. [52] analyzed a bi-material SLB specimen, represented in Figure 18, to assess the interfacial toughness of composite/metal bonding.

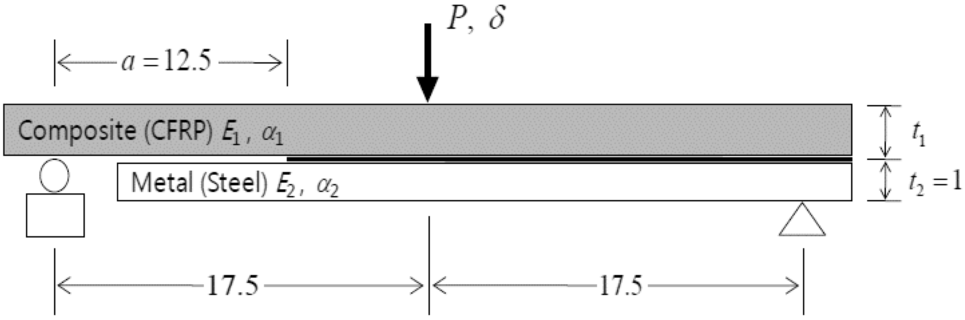

Figure 18 - Schematic representation of the bi-material SLB test [52].

In order to obtain the energy release rate (G_c), the beam compliance method approach was based on the Irwin-Kies equation [46], expressed in Eq. (5), although, instead of using the beam theory to derive the $C = f(a)$ relationship, the bending and shear effect at the crack tip are considered between the relationship of the beam compliance and the crack length through experimental determination. Normalizing the beam compliance and the crack length as E_1BC and a/t_1, respectively, combining with the traditional form of $C = f(a)$ relationship, $C = k(a + \Delta a)^3$, can be rearranged as:

$$\frac{a}{t_1} = \alpha\left(E_1BC\right)^{\frac{1}{3}} + \beta\,, \tag{35}$$

where α and β are constants that are obtained experimentally. Substituting Eq. (35) into Eq. (5), the toughness can be expressed as:

$$G_c = \frac{3}{2t_1}\left(\frac{P_c}{B}\right)^2 \frac{\left(E_1BC\right)^{\frac{2}{3}}}{\alpha E_1}. \tag{36}$$

Since the SLB specimen has dissimilar adherends, the differences between both materials thermal expansion coefficient may introduce thermal residual stresses to the specimen. Therefore, the residual stresses, which contribute to the energy release rate (G_T), need to be considered for the overall energy release rate, expressed as:

$$G = G_{mech} + G_T + G_{\mathrm{int}}\,, \tag{37}$$

where G_{int} is another influence factor for the overall energy release rate that results from the thermal and mechanical load interaction. These additional terms where established by Nairn [53] and are based on the beam theory and linear elastic fracture mechanics, which can be written as:

$$G_T = \frac{1}{2}\frac{E_1t_1\Delta\alpha^2\Delta T^2\left(1+R\lambda^3\right)}{1+R\lambda\left(4+\lambda\left(6+\lambda\left(4+R\lambda\right)\right)\right)} \tag{38}$$

and

$$G_{\text{int}} = \frac{3Pa\Delta T\Delta\alpha\left(R\lambda^2(1+\lambda)\right)}{Bt_1\left(1+R\lambda\left(4+\lambda\left(6+\lambda\left(4+R\lambda\right)\right)\right)\right)}, \tag{39}$$

where $\Delta\alpha=\alpha_1-\alpha_2$, $R=E_1/E_2$ and $\lambda=t_1/t_2$.

Decomposing the 3-point bending load, applied to the crack tip of the SLB specimen, represented in Figure 19, into pure opening (G_I) and pure sliding (G_{II}), the overall energy release rate can be expressed as:

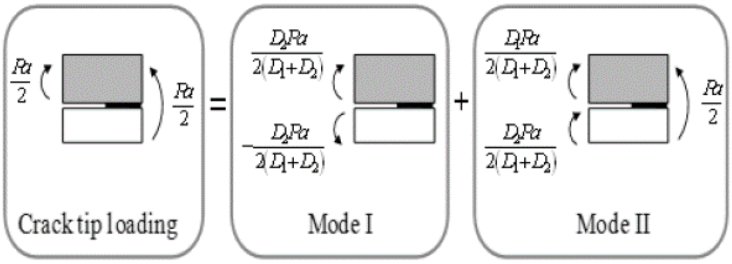

Figure 19 - Loading mode decomposition at the crack tip of a SLB specimen [52].

$$G = G_I + G_{II}\,. \tag{40}$$

G_I and G_{II} can be obtained by the beam theory as follow:

$$G_I = \frac{P^2a^2}{8B}\left(\frac{D_2^2}{\left(D_1+D_2\right)^2}\left(\frac{1}{D_1}+\frac{1}{D_2}\right)\right) \tag{41}$$

and

$$G_{II} = \frac{P^2a^2}{8B}\left(\frac{1}{\left(D_1+D_2\right)}-\frac{1}{D}\right), \tag{42}$$

where $D_1=E_1I_1$ and $D_2=E_2I_2$ for the upper and lower beam, respectively, and $D=(EI)_{eff}$ for the bonded beam section.

2.4.2.1.5 Model 5 – da Silva et al.

da Silva et al. [54] proposed an SLB test data analysis method based on the Szekrényes and Uj [42] method, where the energy release rates, G_I and G_{II}, were calculated considering the beam theory, according with the following expressions:

$$G_I = \frac{12P^2a^2}{16b^2h^3E}\left[1+0.55\left(\frac{h}{a}\right)+0.31\left(\frac{h}{a}\right)^2+0.32\left(\frac{h}{a}\right)\left(\frac{E}{G_s}\right)^{\frac{1}{2}}+0.1\left(\frac{h}{a}\right)^2\left(\frac{E}{G_s}\right)\right] \tag{43}$$

and

$$G_{II}=\frac{9P^2a^2}{16b^2h^3E}\left[1+0.218\left(\frac{h}{a}\right)\left(\frac{E}{G_s}\right)^{\frac{1}{2}}+0.048\left(\frac{h}{a}\right)^2\left(\frac{E}{G_s}\right)\right]. \tag{44}$$

As for the deviation between both methods, in regard with the mode-partitioning concept proposed by Szekrényes and Uj [42], da Silva et al. [54] defined different constant coefficients for each term of both equations, G_I and G_{II}, based on the experimental data analysis.

2.4.2.2 Methods based on an equivalent crack length

The crack length parameter, monitored during the course of the fracture test, is one of the most important terms of the conventional methods to estimate the fracture toughness, although it is also one of the most difficult to obtain with the required accuracy, due to the presence of a fracture process zone ahead of the crack tip. To surpass these difficulties, an equivalent crack length was developed, based on the specimen compliance and on the beam theory, named as Compliance Based Beam Method (CBBM) [55].

2.4.2.2.1 Compliance-Based Beam Method (CBBM)

The CBBM method considers the Timoshenko beam theory as its analytical basis, where the equation for the beam compliance, at the loading point for a given a, can be written as:

$$C=\frac{7a^3+2L^3}{8E_1Bh^3}+\frac{3(a+2L)}{20G_{13}Bh}. \tag{45}$$

To assess the flexural modulus (E_f), which aims to replace E_1, the initial crack length (a_0) and the initial beam compliance (C_0) are used in Eq. (45), thus rewriting as:

$$E_f=\left(C_0-\frac{3(a_0+2L)}{20G_{13}Bh}\right)\frac{7a_0^3+2L^3}{8Bh^3}. \tag{46}$$

Eq. (45) can also be used, considering the equivalent crack length during propagation, through a compliance function (a_e=$f(C)$), measured during the course of the test, that requires a cubic equation resolution. The simplified form of the equation can be represented as:

$$a_e=\left(\frac{1}{6B}\right)A-\frac{2h}{A}, \tag{47}$$

where *A* can be obtained through

$$A=\left[\left(-180C+12\sqrt{3\left(\frac{4h^3+27C_3^2B}{B}\right)}\right)B^2\right]^{\frac{1}{3}} \tag{48}$$

and C_3 by

$$C_3=\frac{2I^3}{32E_fBh^3}+\frac{6L}{20G_{13}Bh}-C\,. \tag{49}$$

Considering Eq. (5), the fracture toughness in mixed-mode can be obtained through:

$$G_T^{SLB}=\frac{21P^2a_e^2}{16E_fB^2h^3}+\frac{3P^2}{40G_{13}B^2h}\,. \tag{50}$$

In accordance with Szekrényes and Uj [42], the G_I^{SLB} and G_{II}^{SLB}, regarding to the energy release rate, can be expressed as:

$$G_I^{SLB}=\frac{3P^2a_e^2}{4E_fB^2h^3}+\frac{3P^2}{40G_{13}B^2h} \tag{51}$$

and

$$G_{II}^{SLB}=\frac{9P^2a_e^2}{16E_fB^2h^3}\,. \tag{52}$$

2.4.2.3 *J-integral method*

Rice [56] developed the *J*-integral method in 1968, aiming to characterize the strain concentration near cracks and notches. His original formulation, for the *J*-integral, can be expressed as:

$$J=\int_C\left(Wn_k-\sigma_{ij}u_{i,k}n_j\right)ds\,, \tag{53}$$

where Wn_k is the strain energy density, σ_{ij} the stress tensor, u_i the displacement vector, n_j the outward normal vector of the contour *C*, represented in Figure 20, and *ds* an element of arc length along *C*. This formulation considers a homogeneous body of linear or non-linear elastic material free of body forces, subjected to a 2D deformation field. Afterwards, the method was reformulated so it could also consider not only orthotropic composite materials but also in three-dimensional deformation fields, where the J_k vector was defined as follows:

$$J_k = \int_C \left(W n_k - \sigma_{ij} u_{i,k} n_j \right) ds + \int_A \left(W \delta_{k3} - \sigma_{i3} u_{i,k} \right)_{,3} da\ ,\ k = 1,2 \tag{54}$$

and

$$J_3 = \int_C \left(W_3 n_1 - \sigma_{3j} u_{3,1} n_j \right) ds\ , \tag{55}$$

where δ_{ij} is the Kronecker tensor and *A* the area enclosed by *C*.

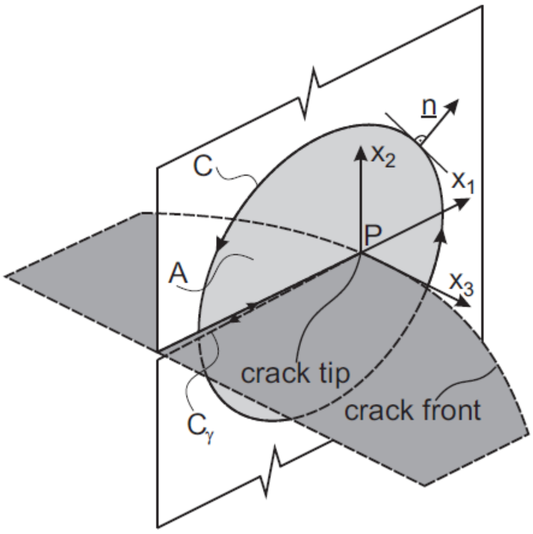

Figure 20 - Reference system for the 3D *J*-integral [57].

The contour *C* includes the crack tip and its integration is performed in a counter clock wise direction, as represented in Figure 20. If static conditions are considered, the *J*-integral is equivalent to the energy release rate (*G*). The *J*-integral is an effective method when the relation between the strain energy (*U*) and the work of external forces (W_f), function of *a*, are difficult to determine the energy release rate (*G*), according with Griffith original fracture model:

$$G = \frac{\partial U}{\partial A} - \frac{\partial W_F}{\partial A}\ . \tag{56}$$

The *J*-integral method is being applied to several tests, such as mode I, mode II and mixed mode, which combines both modes. One of the mixed mode tests for which the *J*-integral is applicable is the SLB test. According to Figure 21, the SLB specimen's lower adherend is not subjected to any sort of load, meaning that it is reasonable to calculate both modes, I and II, individually.

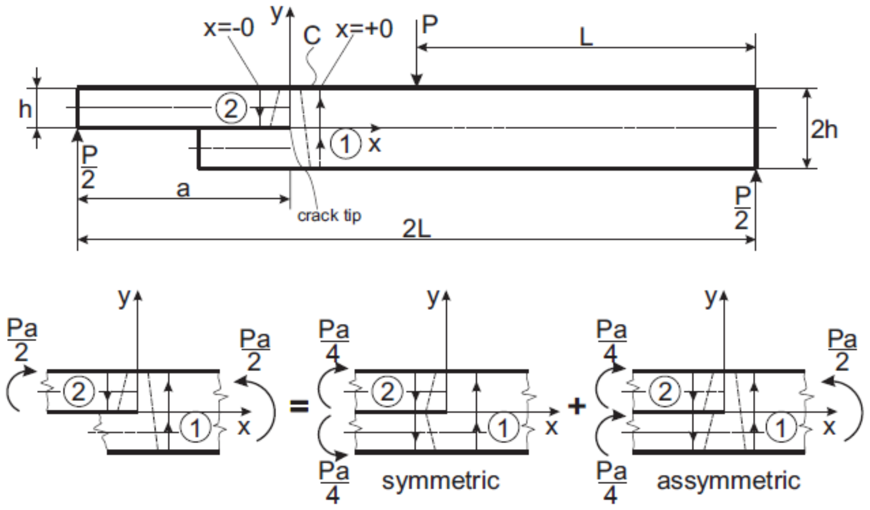

Figure 21 - Stress decomposition and integration path for the SLB specimen [57].

Shivakumar and Raju [58] proposed a mode decomposition method that considers the separation between the displacement and the strain components into symmetrical and asymmetrical parts. The method was later revised by Rigby and Aliabadi [59] and, since then, it has been successfully validated by several researchers.

Decomposing the stress state of the SLB specimen, considering the hypothesis of DCB load conditions, where the bending moment is defined by *Pa/*2, and an ENF specimen, the analytical model can be simplified, as represented in Figure 22.

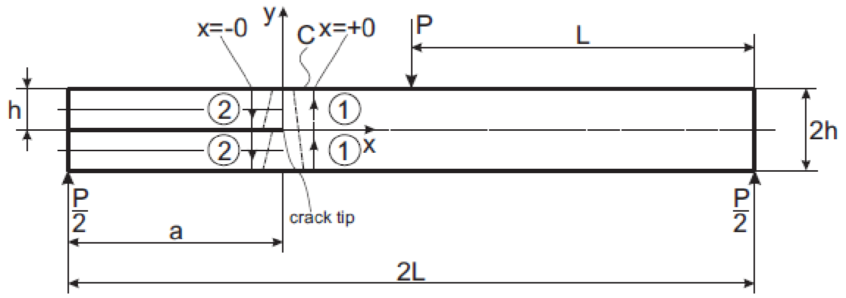

Figure 22 - Integration path for ENF specimen [57].

Through this model simplification, the method proposed by Shivakumar and Raju [58] can be considered as equivalent to the global method of Williams [48]. The final deduced equations for the energy release rate components, using *J*-integral method, can be expressed as:

$$J_I = \frac{12P^2a^2}{16b^2h^3E} \tag{57}$$

and

$$J_{II} = \frac{9P^2a^2}{16b^2h^3E}. \tag{58}$$

Thus, the energy release rate equation, in mixed mode conditions, can be expressed as:

$$J_{I/II} = \frac{21P^2a^2}{16b^2h^3E}. \tag{59}$$

Ji et al. [1] proposed an alternative formulation of the *J*-integral method, for the assessment of the energy release rate in mixed mode, considering a traditional SLB specimen. For the formulation to be effective, several conditions need to be ensured, for instance: the adherends and the adhesive material must behave linearly and non-linearly elastic, respectively, during the course of the fracture test. Also, the loading process must be continuous, without sudden unloading's, in order to promote a cohesive failure and ensure the plastic deformation of the adhesive interlayer to behave non-linearly.

The analytical background of the formulation proposed by Ji et al. [1] was based on Ouyang et al. [60] researches, where the governing equations can be expressed as:

$$\frac{D_2D_1}{\left(D_1+D_2\right)}\frac{d^4w}{dx^4} = \frac{\xi_1 - \dfrac{\delta'''}{\tau'}}{\xi_2 - \dfrac{\delta'''}{\tau'}}\sigma\left(w\right) \tag{60}$$

and

$$\delta'' + \left(\frac{h_1}{2D_1}Q_1 + \frac{h_2}{2D_2}Q_2\right) = \left(\frac{h_1^2}{4D_1} + \frac{h_2^2}{4D_2} + \frac{1}{A_1} + \frac{1}{A_2}\right)\tau, \tag{61}$$

where w and δ are the normal separation and the tangential slip, respectively, between the bottom fiber of the upper beam and the top fiber of the lower beam, σ and τ are the normal and shear interface stresses, h_i the thickness of the beam, where the index i refers to both beams of the specimen (i=1,2), A_i and D_i are the axial and bending stiffness of the beam i per unit of width considering a plane strain condition, and the Q_i is the shear force applied to the beam i. The simplifying parameters ξ_1 and ξ_2 can be obtained as follows:

$$\xi_1 = \frac{1}{A_1} + \frac{1}{A_2} + \frac{\left(h_1+h_2\right)^2}{4\left(D_1+D_2\right)} \tag{62}$$

and

$$\xi_2 = \frac{h_1^2}{4D_1} + \frac{h_2^2}{4D_2} + \frac{1}{A_1} + \frac{1}{A_2} . \tag{63}$$

The combination of normal separation, tangential split, normal stress and shear stress, represented in the Eq. (60), presuppose that, not only the fracture mixed mode manifest simultaneous but are also intrinsically coupled.

If the two beams forming the bonded adhesive joint are identical, the following relationships may be considered:

$$D_1 = D_2 = D ,\ h_1 = h_2 = h \text{ and } \xi_1 = \xi_2 , \tag{64}$$

thus, the Eq. (60) and (61) can be simplified as:

$$\frac{D}{2}\frac{d^4w}{dx^4} = \sigma(w) \tag{65}$$

and

$$\delta'' + \frac{h}{2D}(Q_1 + Q_2) = \left(\frac{h^2}{2D} + \frac{2}{A}\right)\tau , \tag{66}$$

where, for global analysis convenience, the shear forces of the respective beams (*Q1* and *Q2*) are summed, thus establishing the resultant shear forces on the bonded joint (*QT*). Therefore, Eq. (66) can be simplified as:

$$\delta'' + \frac{h}{2D}Q_T = \left(\frac{h^2}{2D} + \frac{2}{A}\right)\tau . \tag{67}$$

The governing equations, simplified into Eq. (65) and (67), represent the mode I peeling behaviour and mode II shear behaviour, respectively. Through analytical operations, the energy release rate for both components of the mixed mode can be deduced. Ouyang et al. [60] defined the J_I, expressed as:

$$J_I(w_0) = \int_0^{w_0} \sigma(w)\,dw = \frac{Q_T}{2}\theta_P , \tag{68}$$

where Θ_P is the relative rotation between the two adherends at the loading line and w_0 is the local normal separation between the two adherends at the cross-section of the crack tip. As for the SLB specimen application, considering the loading at middle span of the adherend, resulting into P=2Q_T, the J_I can be expressed as:

$$J_I(w_0) = \int_0^{w_0} \sigma(w)\,dw = \frac{P}{4}\theta_P . \tag{69}$$

As for the J_{II}, Ouyang et al. [60] defined an equation expressed as:

$$J_{II}\left(\delta_0\right)=\int_0^{\delta_0}\tau\left(\delta\right)d\delta=\frac{\frac{1}{2}\left(\frac{h}{D}\right)^2 Q_T^2 a^2+\frac{hQ_T}{2D}\delta_0}{\frac{2}{A}+\frac{h^2}{2D}}, \qquad (70)$$

where δ_0 is the local tangential slip between the two adherends at the cross-section of the crack tip.

J-integral theory enables the assessment of the interfacial normal stress (σ) and tangential stress (τ), also defined on specialty literature as t_n and t_s, respectively, through the following equations:

$$\sigma\left(w\right)=\frac{\partial J_I\left(w_0\right)}{\partial w_0}=\frac{\partial\left\{\frac{1}{4}P\theta_P\right\}}{\partial w_0} \qquad (71)$$

and

$$\tau\left(\delta\right)=\frac{\partial J_{II}\left(\delta_0\right)}{\partial\delta_0}=\frac{\partial\left\{\frac{\frac{1}{2}\left(\frac{ha}{2D}\frac{P}{2}\right)^2+\frac{h}{2D}\frac{P}{2}\delta_0}{\frac{2}{A}+\frac{h^2}{2D}}\right\}}{\partial\delta_0}. \qquad (72)$$

Moreover, Eq. (71) and (72) allow for the deduction of the cohesive laws for both tensile and shear modes, respectively. Afterwards, the cohesive laws may be used for strength prediction of bonded joints.

2.4.2.3.1 Mechanical sensors for parameter estimation

Considering the *J*-integral formulation for the SLB specimen proposed by Ji et al. [1], there are several parameters, experimentally obtained, that are required for the assessment of the energy release rate of both mixed mode components.

The middle span load applied and specimen displacement data are recorded, as a function of the elapsed time from the beginning of the test. This data is used for the establishment of the *P*-δ curve, thus assessing the joint strength.

Both adhesive layer deformation parameters, given by the separation of the adherends, w_0 and δ_0, defining the local normal separation and local tangential slip between the two adherends at the cross-section of the crack tip, respectively, can be experimentally recorded through a Linear Variable Differential Transformer (LVDT) displacement sensor [61].

The relative rotation between the two adherends at the loading line (Θ_P) can be measured with the assistance of a shaft encoder for epoxy adhesives or with the combination of both shaft encoder and two tilt sensors for polyurethane adhesives [61].

These sensors feature high accuracy and resolution for recording precise data. Furthermore, the measurement of *a* is performed in real-time, during the course of the test. Is presented in Figure 23, an example of an application of LVDT and shaft encoder for a DCB specimen.

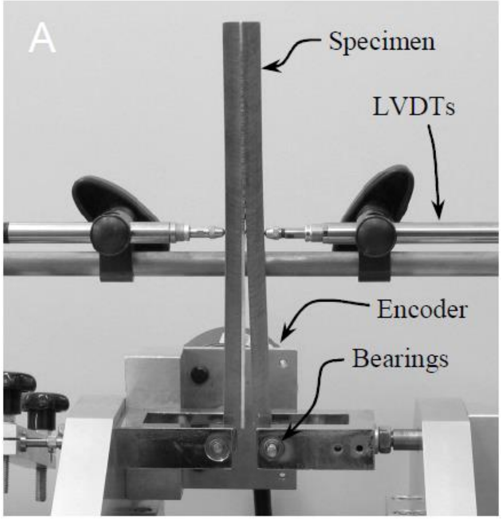

Figure 23 – Mechanical sensor for parameter estimation in a DCB specimen [61].

2.4.2.3.2 Optical sensors for parameter estimation

The parameters required for the assessment of the energy release rate of both mixed mode components, considering the work of Ji et al. [1], can also be estimated through optical sensors. 3D Digital Image Correlation (DIC) systems provide full-field strain and out-of-plane displacement data for hundreds of points for one specimen, being this feature its main advantage over the conventional instrumentation systems [62].

The DIC system is an advanced, image based, with non-contact, full-field deformation measurement technique capable of analysing materials subjected to thermal, mechanical or variable environmental loadings, shown in Figure 24. It monitors the movement of naturally occurring phenomena or an applied surface pattern load to the specimen on the course of the mechanical test. Complete 3D surface measurements can be obtained through stereoscopic camera configurations [62].

Regarding the procedure, first a reference image is captured at zero loading condition, coinciding with zero strain. Then, several digital images are recorded, considering constant time intervals, for instance each 5 seconds, during the specimen loading. After the acquisition of the digital images, the area of interest is selected and divided into discrete pixel blocks, with a resolution of, for instance, 4 pixels per millimetre, featuring a minimum number of distinct surfaces. Moreover, each subset of the area of interest, should have a distinguished signature pattern [62].

The distortion signature patterns, from image to image, are minimized with the use of a correlation algorithm, based on the sum of square differences of grey pixel values. Furthermore, the strain values are then derived from the deformations [62].

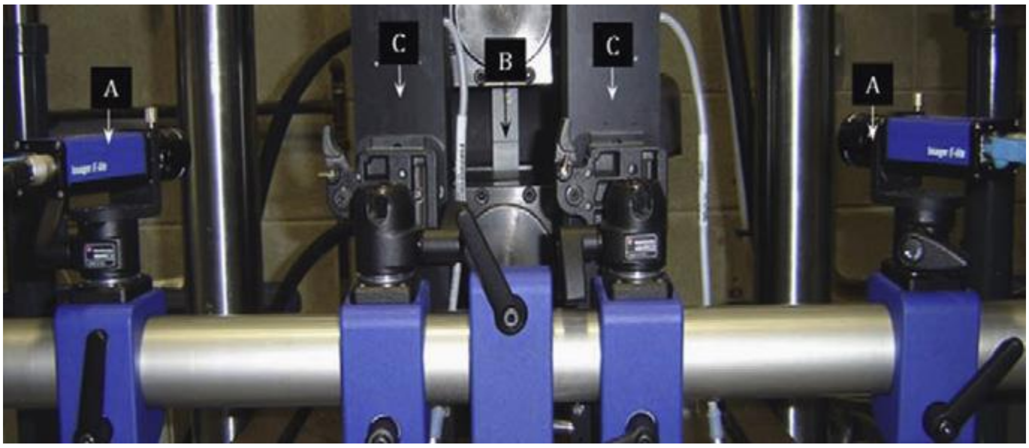

Figure 24 - DIC equipment setup for SLJ specimen [62].

THESIS DEVELOPMENT

3 THESIS DEVELOPMENT

3.1 Experimental work

The experimental work was elaborated taking into account several specifications defined for the development of the thesis. Foremost, it was intended to test an adhesively-bonded joint in which the base material of the adherends was composite. Three adhesives with different properties were tested in order to understand their impact on the adhesively-bonded joint performance. The chosen adhesively-bonded joint design was the SLB geometry, which is capable of developing combined stresses of tensile and shear, establishing the mixed mode, recreating the often service operational conditions. The specimen manufacturing process and test procedure were conducted based on previous researches due to the lack of test standardization.

3.1.1 Materials

The adhesively-bonded joint is always manufactured based on two main materials, the adherends and the adhesive, notwithstanding its geometry. Both materials feature dissimilar properties, each with different functions in the overall adhesively-bonded joint performance. The option of obtaining numerous combinations of different properties, from both dissimilar materials, increases significantly the range of application of adhesively-bonded joints, whether for different environments or loading conditions.

3.1.1.1 Adherends

The adherends were manufactured in composite material, created from a unidirectional carbon-epoxy pre-preg (SEAL® Texipreg HS 160 RM; Legnano, Italy). The pre-preg was supplied in roll form, with a thickness of 0.15 mm. To obtain the adherends thickness of 3 mm, defined during the adhesively-bonded joint design, 20 layers of carbon-epoxy pre-preg were cut with the adherends dimensions, hand-lay-up and cured in a hot-plates press for 1 hour at 130 °C and pressure of 2 bar [63]. The elastic-orthotropic properties of a unidirectional lamina for similar curing conditions are shown in Table 1.

Table 1 - Elastic orthotropic properties of a unidirectional carbon-epoxy ply aligned in the fibers direction (x-direction; y and z are the transverse and through-thickness directions, respectively [63]

E_x = 1.09E+05 MPa	ν_{xy} = 0.342	G_{xy} = 4315 MPa
E_y = 8819 MPa	ν_{xz} = 0.342	G_{xz} = 4315 MPa
E_z = 8819 MPa	ν_{yz} = 0.380	G_{yz} = 3200 MPa

3.1.1.2 Adhesives

The adhesively-bonded joint experimental test programme considered three dissimilar structural adhesives in order to understand the behavior of the adhesively-bonded joint during the test, when it presents different properties, referring to the kind of structural adhesive used. The structural adhesives tested were: the brittle epoxy Araldite® AV138, the ductile epoxy Araldite® 2015 and the ductile polyurethane Sikaforce® 7752. Their mechanical and toughness properties were characterized in previous researches by Campilho et al. [64-66] and Faneco et al. [67]. Overall, all the structural adhesives were two-part adhesives, which combined the resin with a hardener, and featured low viscosity to ensure an easier application on the adherends [63].

3.1.1.2.1 Araldite® AV138

The structural epoxy adhesive Araldite® AV138 is produced by Huntsman Advanced Materials. It exhibits a brittle behavior notwithstanding its high strength, as shown in Figure 25 and Table 2. It is also considered as an adhesive capable of joining several materials such as metal, composite or polymer [64].

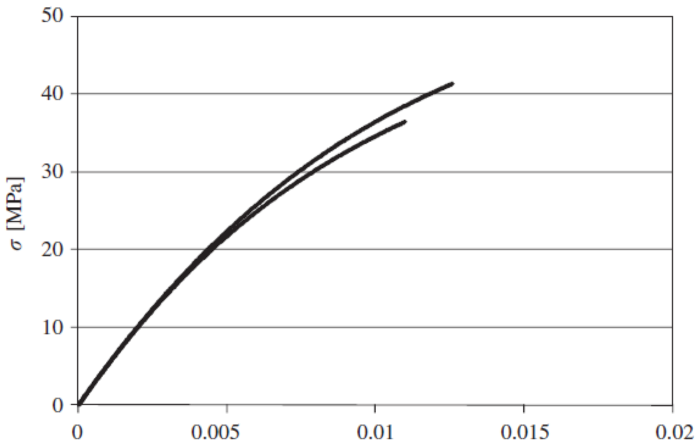

Figure 25 - Araldite® AV138 experimental σ-ε curves estimated by bulk specimens [66].

Being a two-part adhesive, the Araldite® AV138 is supplied in two separated recipients, shown in Figure 26, where one contains the thermoset resin AV138 and the other the hardener HV998. Both materials are mixed together manually in compliance with the weight proportions, in accordance with the adhesive specification. The mixture proportion is 100 g of resin to 40 g of hardener, considering an accuracy of ±5%. Characteristically, this adhesive is a thixotropic gap filling paste that features low gas emissions and volatile loss, and cures under temperatures below 5 °C.

Figure 26 - Structural adhesive Araldite® AV138 [68].

Due to its brittleness, the correct application of the Araldite® AV138 is crucial since it is considered to be extremely fragile and sensitive to manufacturing defects resulting in great deviations between the specimens [66].

Table 2 - Structural adhesive Araldite® AV138 properties [66].

Properties	Araldite® AV138
Young´s modulus, E [GPa]	4.89±0.81
Poisson´s ratio, ν	0.35*
Tensile yield stress, σ_y [MPa]	36.49±2.47
Tensile failure stress, σ_f [MPa]	39.45±3.18
Tensile failure strain, ε_f [%]	1.21±0.10
Shear modulus, G [GPa]	1.56±0.01
Shear yield strength, τ_y [MPa]	25.10±0.33
Shear failure strength, τ_f [MPa]	30.20±0.40
Shear failure strain, γ_f [%]	7.80±0.70
Toughness in tension, G_{Ic} [N/mm]	0.20**
Toughness in shear G_{IIc} [N/mm]	0.38**

* Manufacturer’s value

** Estimated value

3.1.1.2.2 Araldite® 2015

The structural adhesive Araldite ® 2015 is also produced by Huntsman Advanced Materials. It is considered as a balanced adhesive, with decent strength, but lower ultimate strength compared to the Araldite® AV138, and decent ductility, capable of enduring large plastic displacements before failure. Generally, a redistribution of the stresses arises in areas where the stresses are concentrated which frequently are located at the edges of the overlap end of the adhesively-bonded joints [64].

Figure 27 shows the cartridges, containing the adhesive, used for the application of the adhesive, previously mixed, according with the adhesive specifications.

Figure 27 - Structural adhesive Araldite® 2015 [68].

The bond strength and the adhesively-bonded joints durability are two key aspects to be reckoned, which have direct impact in the performance during its application, specifically for this adhesive, since it depends on an adequate surface treatment. The adherend surfaces to be bonded should be clean with solvent wiping, like acetone. Moreover, its preparation may also include the combination of several finishing processes such as: mechanical abrading, chemical cleaning and acid etching [3].

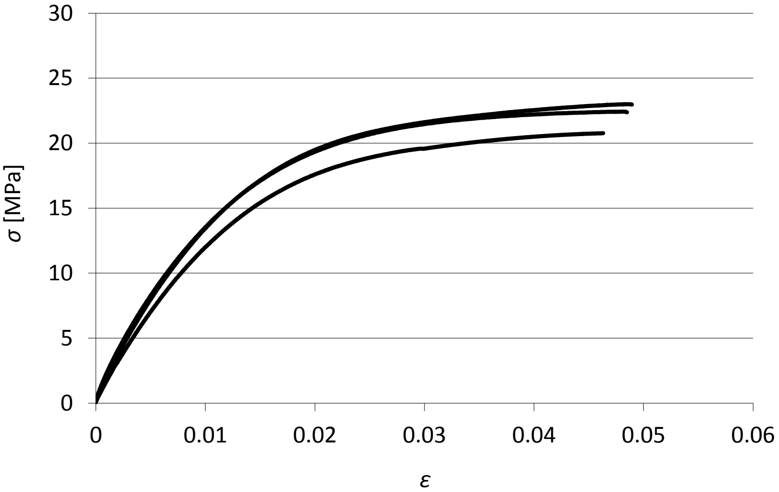

Figure 28 - Araldite® 2015 experimental σ-ε curves estimated by bulk specimens [64].

Analyzing the Araldite® 2015 σ-ε curves and mechanical properties, depicted in Figure 28 and Table 3, respectively, it is evident that the shear failure strain is way higher, almost six times above the Araldite® AV138 value. Yet, the tensile and shear failure strength of the Araldite® AV138 is twice the value of the Araldite® 2015. Therefore, the Araldite® 2015, being the most ductile adhesive, allows the stresses distribution at the stress concentration area, which is often located at the sharp edges of the overlap, due to the adhesively-bonded joint asymmetry / distinct deformation of the adherends along the overlap [64].

Table 3 - Structural adhesive Araldite® 2015 properties [64].

Properties	Araldite® 2015
Young´s modulus, E [GPa]	1.85±0.21
Poisson´s ratio, ν	0.33*
Tensile yield strength, σ_y [MPa]	12.63±0.61
Tensile failure strength, σ_f [MPa]	21.63±1.61
Tensile failure strain, ε_f [%]	4.77±0.15
Shear modulus, G [GPa]	0.56±0.21
Shear yield strength, τ_y [MPa]	14.60±1.3
Shear failure strength, τ_f [MPa]	17.9±1.8
Shear failure strain, γ_f [%]	43.9±3.4
Toughness in tension, G_{Ic} [N/mm]	0.43±0.02
Toughness in shear G_{IIc} [N/mm]	4.70±0.34

* Manufacturer’s value

3.1.1.2.3 Sikaforce® 7752

The structural polyurethane adhesive Sikaforce® 7752 is produced by Sika. It is the most ductile adhesive, comparing with both Araldite® AV138 and Araldite® 2015.

Figure 29 - Structural adhesive Sikaforce® 7752 [68].

The Sikaforce® 7752 is a thixotropic structural adhesive that uses a polyol resin, incorporated with charges, and a hardener based on isocyanate, shown in Figure 29. It features low gas emissions and volatile loss, and high temperature resistance. Concerning the adhesive preparation, to comply with the adhesive specification, the mixing proportion must be 100 g of resin to 20 g of hardener. It cures under room temperature, exhibits good environmental and chemical exposure resistance, high impact resistance and improved flexibility at low temperatures. It is also considered as an adhesive capable of joining several materials such as metal, ceramic or wood [67].

Analyzing the Sikaforce® 7752 σ-ε curves and mechanical properties, shown in Figure 30 and Table 4, respectively, it is clear that it has the lowest tensile and shear failure strength comparing with both Araldite® adhesives. Nonetheless, it has the highest ductility, which ensures a large plastic displacement before failure, thus resulting in a high adhesively-bonded joint strength [67].

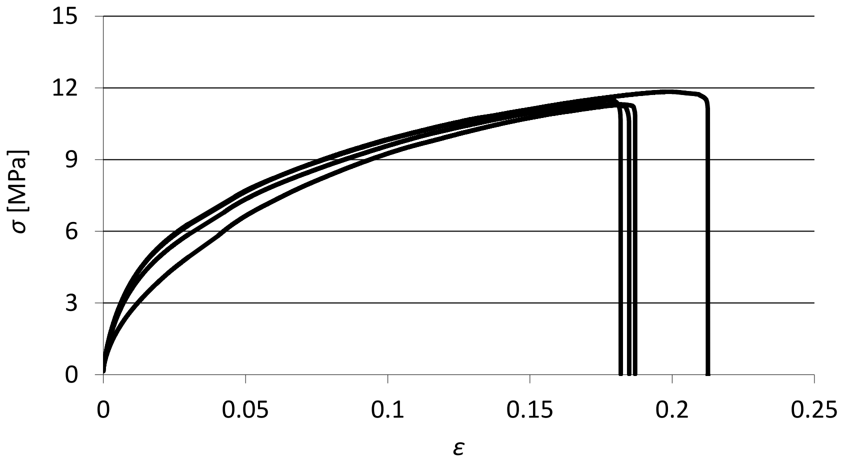

Figure 30 - Sikaforce® 7752 experimental σ-ε curves estimated by bulk specimens [67].

Table 4 - Structural adhesive Sikaforce® 7752 properties [67].

Properties	Sikaforce® 7752
Young´s modulus, E [GPa]	0.49±0.09
Poisson´s ratio, ν	0.30*
Tensile yield strength, σ_y [MPa]	3.24±0.48
Tensile failure strength, σ_f [MPa]	11.48±0.25
Tensile failure strain, ε_f [%]	19.18±1.40
Shear modulus, G [GPa]	0.19±0.01
Shear yield strength, τ_y [MPa]	5.16±1.14
Shear failure strength, τ_f [MPa]	10.17±0.64
Shear failure strain, γ_f [%]	54.82±6.38
Toughness in tension, G_{Ic} [N/mm]	2.36±0.17
Toughness in shear G_{IIc} [N/mm]	5.41±0.47

* Manufacturer's value

3.1.2 Specimens' fabrication

The materials are considered as important parameters that directly affect the performance of the adhesively-bonded joint, for a given application. However, its performance also relies on other parameters with significant impact, such as the specimens' fabrication. The adhesively-bonded joint dimensions, especially the ones related with the bond overlap, like the width of the adherends or the adhesive thickness, have a huge impact on the adhesively-bonded joint strength. Moreover, the specimens' fabrication meticulous bonding procedure, if not strictly controlled, could result on critical failures during the course of the test, like for example premature failures. These failures might be caused due to, for instance, lack of surface preparation or defective application of the adhesive.

3.1.2.1 SLB geometry

For the adhesively-bonded joint experimental test programme, the selected specimen's geometry for the testing was the SLB. This geometry allows for an adhesively-bonded joint toughness assessment under mixed mode conditions, which was the objective of the overall programme. The SLB specimen geometry was established based on two requirements. The first was the compliance of the 70/100 ratio between a_0 and L. This criterion is considered as an experimental rule for good practices, which was already tested and validated by several researchers [63]. The second requirement was the acknowledge of the limitations related with the manufacturing process, mainly due to the moulds' availability, restricting the specimens' final dimensions.

The specimen geometry dimensions represented in Figure 31 are listed in Table 5, where h represents the adherends thickness, a_0 the initial crack length, L the distance between the centerline of the rollers at the edges of the joint and the loading line, halfway between the upper adherend, t_A the adhesive thickness and B the width of the adherends.

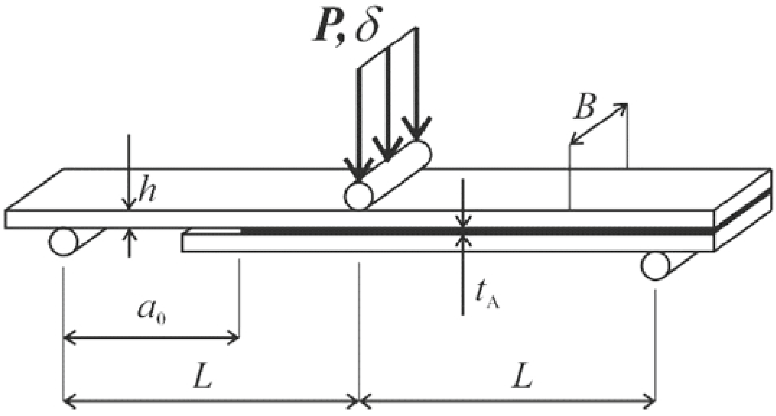

Figure 31 - Geometry of the SLB specimen [63].

Table 5 - Dimensions of the SLB specimen [63].

h	3 mm
a_0	87.5 mm
L	125 mm
t_A	1 mm
B	15 mm

The overall thickness of the adhesively-bonded joint specimen can be defined as h_t and it had a value of 7 mm. Due to the SLB geometry, the upper adherend was manufactured with 280 mm length, whereas the lower adherend was cut to 200 mm [63].

3.1.2.2 Fabrication process

For the experimental test programme of the adhesively-bonded joint, 7 specimens were manufactured for each adhesive type, from 3 composite plates of 300 x 300 mm² with 3 mm thickness. Each plate was constructed from 15 mm thick pre-preg roll layers, stacked unidirectionally until the thickness of 3 mm was reached [68].

The stacking process required heat application for the pre-preg resin to activate, and pressure between each pre-preg layer application, as shown in Figure 32, until the plate stacking process was completed. During the overall staking process, the existence of air bubbles in between the pre-preg layers was meticulous inspected, since these are considered as one of the major cause of failure, related to the manufacturing process of an adhesively-bonded joint [68].

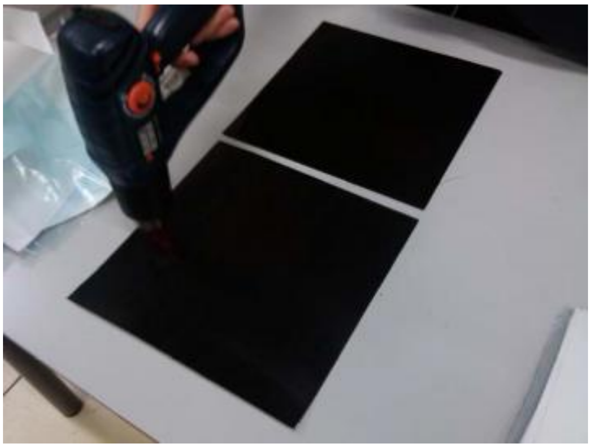

Figure 32 - Heat application over a pre-preg layer [68].

Subsequently, the composite plates were then inserted inside a mold, one at a time, which was then placed inside a hot plate press, under 3 bar constant pressure, in accordance with the thermal cycle represented in Figure 33 [68].

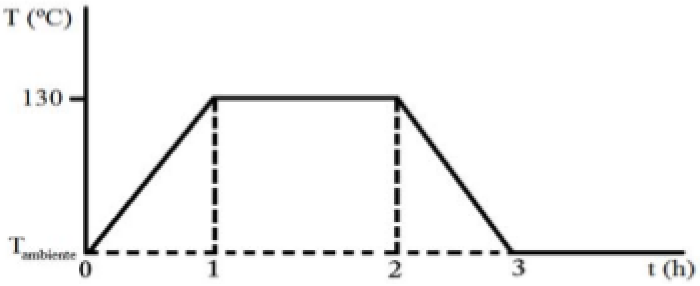

Figure 33 - Used thermal cycle for the composite plates [68].

After the thermal cycle, at which the plates were subjected for three hours, the desired properties for the adherends were reached. These were then cut according to the geometry preconized for each adherend. Next, the adherends' bonding surfaces were prepared through abrasive techniques to increase the adhesion and the contact surface, and also cleaned with acetone for removal of harmful elements of the bonding process [68].

For the adhesively-bonded joints, the thickness of the adhesive is an important parameter to be ensured under strict tolerances. Therefore, spacers were manufactured to guarantee non-deviations from the preconized thickness. Moreover, the crack tip spacers were also responsible to introduce the initial crack length in the adhesive, since the other edge of the adhesive should not feature cracks. The spacer responsible for introducing the initial crack length was constructed by three bonded metal layers, considering that two of them featured 0.45 mm and the other, in between them, 0.10 mm thickness. The latter, offset from the other two spacers, representing the initial crack length, acted as a blade. The spacer that only needed to ensure the thickness was manufactured in bulk form with 1 mm thickness [68].

With the adherends and spacers manufactured, the bonding process was then initiated. A dedicated bonding platform was used, which contained precisely the adherends locations. Firstly, the longer adherends were positioned on the platform and then the spacers placed over them, properly coated with a release agent. The adhesive was then applied in the pre-defined bonding surface, followed by the adhesively-bonded joint assembly. A uniform manual pressure was applied to drain the excess material and to ensure that the spacers were in service. In parallel, positioning shoes were manufactured and bonded to the edge of the longer adherends [68].

The last stage of the bonding process was the application of positioning clamps, coincident with the spacers position, to apply constant pressure during the curing process of the adhesive, shown in Figure 34 [68].

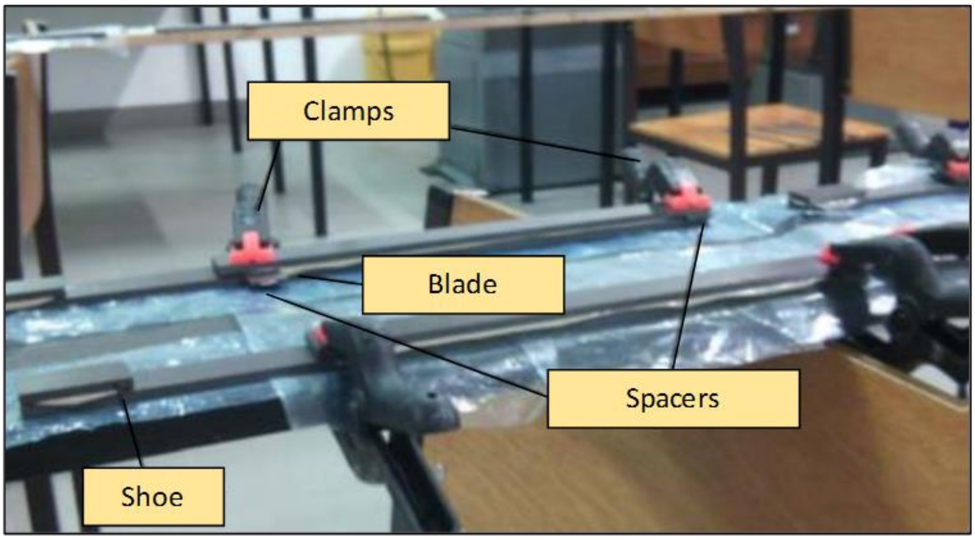

Figure 34 - Platform used for the bonding process [68].

3.1.2.3 *Preparation for testing*

With the adhesive bonding procedure completed, the test specimens remained in a curing process, which depended on the type of adhesive applied. The curing timings were:

- Araldite® AV138: 72 h;
- Araldite® 2015: 72 h;
- Sikaforce® 7752: 120 h.

After the curing process was completed, the spacers applied at the beginning of the bonding process were removed. The test specimens, at this stage, feature enough stiffness to be prepared for testing. The adhesive excess was removed manually and then, a grindstone was used to remove the excess adhesive at the edges of the test specimen. A slight chamfer or round geometry could induce deviations of the final results therefore, every specimen was carefully grinded evenly, as shown in Figure 35. Finally, the test specimens were cleaned with acetone [68].

Figure 35 - Test specimen appearance after finishing operations [68].

Afterwards, a pre-crack was introduced into the test specimen, through a small load, to separate both adherends, where the crack was intended to initiate. The distance between the centerline of the leftmost roller till the pre-crack tip, also known as a_0, was registered before the specimens testing and the values are shown in Table 6.

Table 6 - Initial crack length (a_0) values, for each test specimen, in mm [68].

Specimen No.	Araldite® AV138	Araldite® 2015	Sikaforce® 7752
1	85.60	88.39	85.98
2	85.63	85.60	88.51
3	84.54	85.40	85.82
4	86.87	84.67	88.61
5	104.36	88.96	87.17
6	86.40	88.52	86.70
7	91.45	86.80	85.30

The overall measured values of a_0 were in accordance with the projected value of approximately 87.50 mm, depicted in Table 5. However, specimen 5 from the Araldite® AV138 behaved differently from the rest, with a higher pre-crack propagation, which could be related to the adhesive brittle behavior and the manual crack propagation process before the test is initiated [68].

Before initiating the experimental tests, the final preparation was to glue a paper scale into the specimens, as shown in Figure 36, to photograph record *a* propagation during the course of the test.

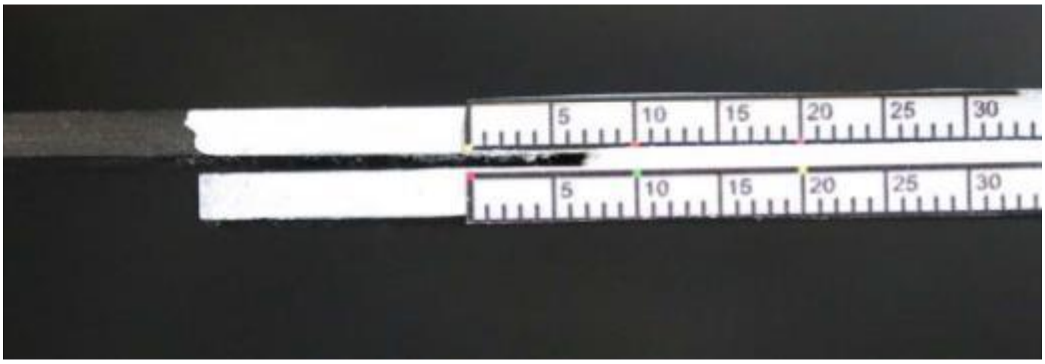

Figure 36 - Specimen appearance before the experimental test [68].

3.1.3 Specimens' testing

The experimental tests were performed on seven specimens for each kind of adhesive, considering the same experimental conditions. The experimental results were obtained by Santos and Campilho [63] and were then analyzed in the scope of this thesis.

3.1.3.1 Test conditions

For the experimental testing programme, an electro-mechanic testing machine Shimadzu AG-X 100 with a loading cell of 100 kN was used, shown in Figure 37. Data resulting from the experimental test, namely loading (P) and displacement (δ), were recorded on a data acquisition equipment, with an acquisition frequency of 4 Hz, and were treated in a graph form, from which the P-δ curves were obtained.

3.1.3.2 Optical method

During the course of the experimental tests, a photograph equipment was used, Canon EOS 70D with 20 MP, to record the propagation of a, from the start to finish of the test, as shown in Figure 37. Due to the dimensional magnitude of the crack, keeping the equipment stable, through special mounting devices, and ensuring high illumination on the specimen, so the pictures taken could feature high quality, were important aspects considered during the setup of the overall optical equipment, before initiating the experimental tests.

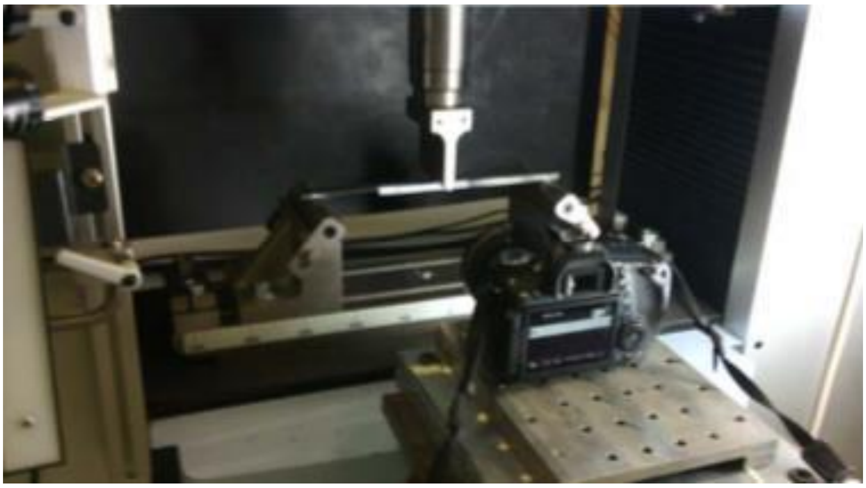

Figure 37 - SLB specimen testing conditions [68].

3.1.3.3 Testing procedure

The preparation of the experimental tests was initiated with the positioning of the testing specimens on a three-point bending test equipment. The specimens were accurately aligned so that the axis of the loading punch and the symmetry line of the test specimens remained collinear, before starting the test.

Thereafter, the loading punch was then regulated to a height close to the upper surface of the test specimen, again ensuring the collinearity between the axis of the loading punch and test specimen, in order to optimize the experimental test time.

With the specimen properly positioned, the photographic equipment was installed such that, during the course of the test, all the deformed shape of the specimen can fit in the image recorded by the equipment, knowing that the greater the displacement of the loading punch, the greater the deformation of the specimen.

Afterwards, with all the equipment prepared for the beginning of the experimental test, the speed of the test was established based on the type of adhesive tested and framed in a quasi-static test superposition, in order to eliminate viscoelastic effects. The speed of the loading punch used, by adhesive, was:

- Araldite® AV138: 0.35 mm/min;
- Araldite® 2015: 0.80 mm/min;
- Sikaforce® 7752: 3 mm/min.

During the course of the experimental test, the photograph equipment recorded pictures in between time intervals of 5 s until the end of the trial. The experimental test was considered as completed as soon as the crack length reached the loading line of the punch or until failure of the adhesive.

3.2 Numerical work

The purpose of the numerical analysis was to recreate the experimental test results through mixed-mode criteria and cohesive laws capable of representing the selected adhesives behaviour. Furthermore, after validating the cohesive laws, these may be applicable for strength prediction of bonded joints for the selected adhesives. The simulations were performed based on the Finite Element Method (FEM), considering the CZM approach.

3.2.1 Numerical conditions

The preconized software to perform the FEM analysis was Abaqus®. An appropriate and generally used tool, FEM based, with CZM modules incorporated, for strength prediction of adhesively-bonded joints which, in this specific work, is applied to SLB specimen trials.

The SLB specimen was modelled in as a two-dimensional solid, represented in Figure 38, for computing time optimization, since the differences to three-dimensional modelling were residual. The analysis carried out was non-linear geometrical.

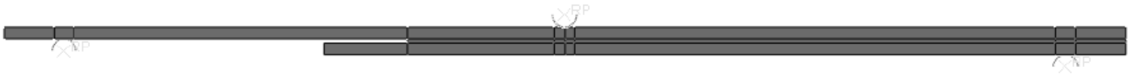

Figure 38 - SLB specimen model.

The mesh was applied with two different elements, depending on the material characteristics. The adherends were modelled with plane-strain four-node quadrilateral solid finite elements (CPE4 from Abaqus®) and the adhesive with four-node cohesive elements (COH2D4 from Abaqus®) with linear softening [63].

The optimization of the mesh was performed through different refinements, depending on the areas of interest of the specimen, knowing in advance which are the critical zones. Figure 39 represents the overall specimen meshing with different refinements.

Figure 39 - Overall SLB specimen meshing.

Along the thickness, the adherends' mesh features 6 elements with size grading effects, being the regions near the adhesive layer and near the cylinders contact surface more refined. The adhesive layer mesh, on the other hand, has a single element through its thickness. Lengthwise, the mesh features high refinement in the crack propagation area and near the support cylinders, with 0.20 mm and 0.05 mm length, respectively [63]. Figure 40 demonstrates the areas where the high refinement was applied.

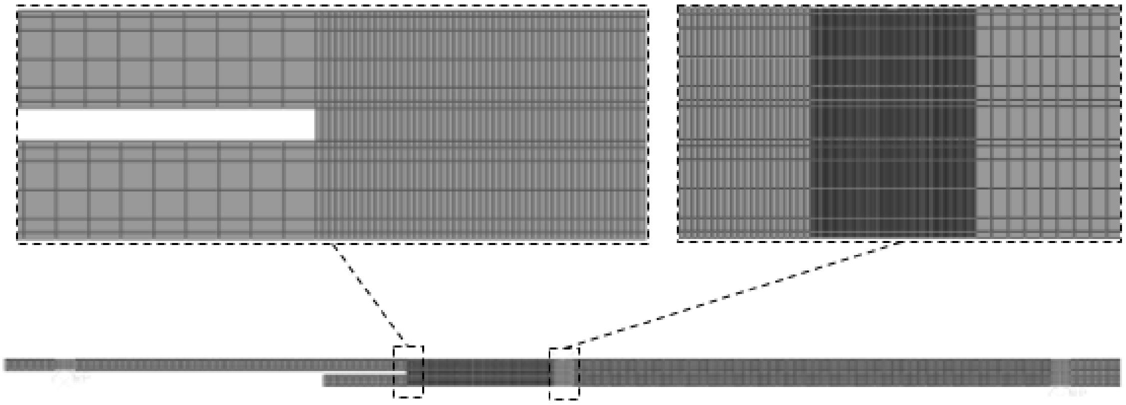

Figure 40 - SLB specimen regions where high refinement meshing was applied.

Furthermore, bias effects were considered to grant variations of the FEM elements' size, to achieve higher refinement in the areas with higher stress concentrations. This feature optimized the overall meshing process, therefore improving the computing time of the simulation, without jeopardizing the results precision [63].

The boundary conditions were established in several forms, based on the specimen experimental behaviour, during the course of the test. The two supporting cylinders were fixed in the *xy* plane, the loading cylinder restricted in the horizontal direction (*x*) and the overall specimen model, also restrained in the horizontal direction (*x*), in an intermediate reference point, to avoid rigid body movement deviations. The load was applied at half-span of the specimen, through a loading cylinder, in the vertical direction and downward, based on a prescribed displacement [63]. Overall boundary and loading conditions are represented in Figure 41.

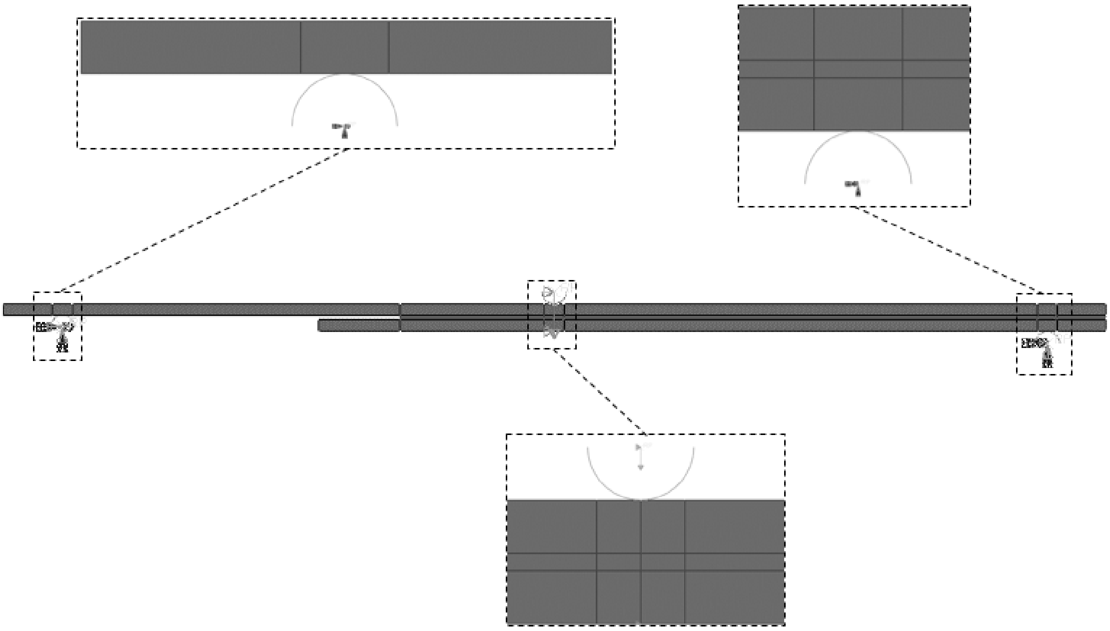

Figure 41 - SLB specimen overall boundary and loading conditions application.

The contact conditions were defined between the adherends and the adhesive layer, at the initial crack zone. Moreover, between the contacting cylinders and adherends surfaces, the contact conditions were established to prevent interpenetration and ensure the free sliding, without friction [63]. The interaction type established was surface-to-surface contact for the overall specimen. Its properties consisted of frictionless tangential behaviour and hard contact for normal behaviour. The Figure 42 identifies the locations were the contact conditions were applied.

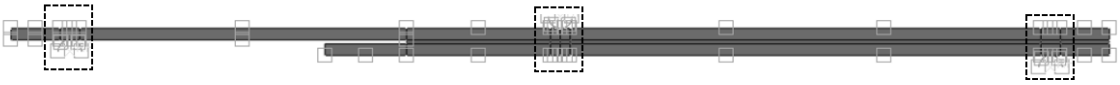

Figure 42 - Overall SLB specimen contact conditions.

Three numerical models were designed for each specimen, each one considering different types of adhesives, based on the experimental specimens, by introducing several specific parameters as, for instance, the measured value of the a_0. The defined CZM, for the numerical analysis, featured a triangular shape with average values of G_{IC} and G_{IIC} acquired from DCB and ENF tests. The values of t_n^0 and t_s^0 were approximated to the data proposed by Santos and Campilho [63].

3.2.2 Cohesive model formulation

There are several cohesive law formulations, considering different shapes, which are based on the type of adhesive behaviour or the established interface in simulation, for achieving accurate results [69]. These formulations have been developed over the years in shapes, such as: triangular [70], linear parabolic [71], exponential [72], polynomial [73] and trapezoidal [74], being the triangular shape the most used.

3.2.2.1 Triangular model

The triangular law is considered as an approachable formulation, mainly due to its simplicity, the few parameters required and results accuracy for most of the experimental conditions.

The homologous nodes of cohesive elements are linked through the tensile and shear relations between the stresses and relative displacements represented in Figure 43, in which the CZM approach is based. These relationships enable to replicate the elastic behavior up to t_n^0 in tension or t_s^0 in shear and subsequent softening, until the full degradation of the material properties, resulting in the model failure [63].

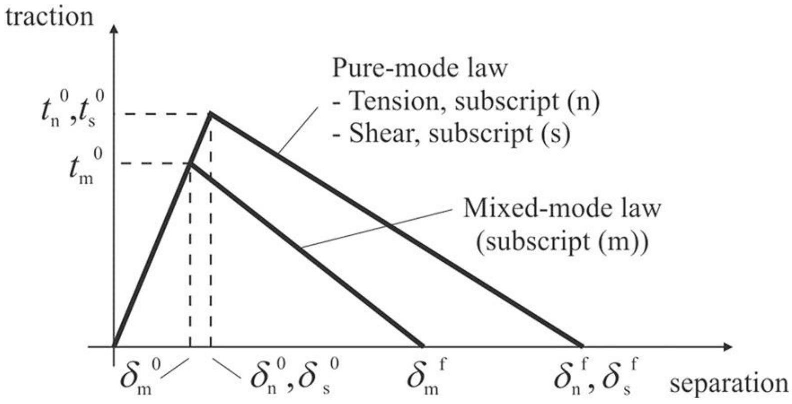

Figure 43 - Traction separation law with linear softening law from Abaqus® [63].

The shape of the softening portion of the CZM law may be configured to ensure the behavior of different materials or interfaces compliance [74]. The areas under the tensile and shear separation laws are equal to G_{IC} and G_{IIC}, respectively. In pure mode loading conditions, when the stresses are released in the respective damage law, the damage grows until a specific integration point is reached. In mixed loading conditions, the combined tension and shear stresses are obtained through stress and energetic criteria [27, 63].

The triangular law, represented in Figure 43, initially features a linear elastic behaviour under a specific relative displacement, followed by a linear degradation trend. The elastic behaviour of the triangular law is established through a constitutive matrix (***K***), which considers the stiffness parameters and related stresses (***t***) and strains (***ε***) along the interface (Abaqus® 2013). The matrix is defined as:

$$\boldsymbol{t} = \begin{Bmatrix} t_n \\ t_s \end{Bmatrix} = \begin{bmatrix} K_{nn} & K_{ns} \\ K_{ns} & K_{ss} \end{bmatrix} . \begin{Bmatrix} \varepsilon_n \\ \varepsilon_s \end{Bmatrix} = \boldsymbol{K\varepsilon}\,, \tag{73}$$

where t_n and t_s are the current tensile and shear stresses, respectively, while ε_n and ε_s are the corresponding strains. For thin adhesive layers, a reasonable approximation may be established considering [64]

$$K_{nn} = E \text{ , } K_{ss} = G_{xy} \text{ and } K_{ns} = 0 . \tag{74}$$

There are several damage initiation formulations already developed, for instance, the quadratic nominal stress criterion, considered by Moreira and Campilho [75], which provided accurate results. This criterion can be expressed as (Abaqus® 2013)

$$\left\{ \frac{\langle t_n \rangle}{t_n^0} \right\}^2 + \left\{ \frac{t_s}{t_s^0} \right\}^2 = 1 , \tag{75}$$

where the Macaulay brackets, $\langle \ \rangle$, empathize that a pure compressive state that does not initiate damage [63].

As soon as the mixed mode cohesive strength (t_m^0) is achieved, as represented in Figure 43, through Eq. (75), the material stiffness begins to degrade until the separation of the homologous nodes take place. The complete separation is generally estimated through a linear power law form, for failure in pure mode, by considering the power law exponent $\alpha = 1$ (Abaqus® 2013)

$$\left(\frac{G_I}{G_{IC}} \right)^{\alpha} + \left(\frac{G_{II}}{G_{IIC}} \right)^{\alpha} = 1 . \tag{76}$$

3.3 Results

The fracture toughness assessment of the adhesively-bonded joint was performed by correlation of the experimental and numerical data, for the three kinds of adhesives. The *J*-integral method, proposed by Ji et al. [1], which is an alternative formulation from the Williams [48] global method, was used to interpret the data, in order to evaluate the fracture toughness of the adhesive.

3.3.1 *J*-integral analytical parameter estimation

The *J*-integral based alternative formulation of Ji et al. [1] has three important parameters: Θ_p, w_0 and δ_0. These parameters can be obtained, during the course of the test, through mechanical and optical sensors such as LVDT and DIC, respectively. However, in this work, these parameters were determined analytically by using a vector and geometric analytical analysis based on numerical measurements.

3.3.1.1 Relative rotation between two beams at the loadline (Θ_P)

The relative rotation between the two adherends at the loading line is a parameter required to determine J_I and σ, through Eq. (69) and (71), respectively. The formulation requires the parameter to be set in radians (rad), although it is recommended to convert also in degrees (°) for a clear interpretation of the adherends behavior during the course of the test. Concerning the vector analytical approach to determine Θ_P, two vectors were defined, *u* and *t*. Both vectors are colinear with the adherends thickness at the leftmost edge of the specimen, near the loading line, resultant from the roller. The former is confined between the virtual points E and F, in which the latter is established between the virtual points G and H, as expressed by Eq. (77) and (78), and shown in Figure 44.

$$\vec{u} = \left(F_x - E_x, F_y - E_y, F_z - E_z\right), \tag{77}$$

$$\vec{t} = \left(H_x - G_x, H_y - G_y, H_z - G_z\right). \tag{78}$$

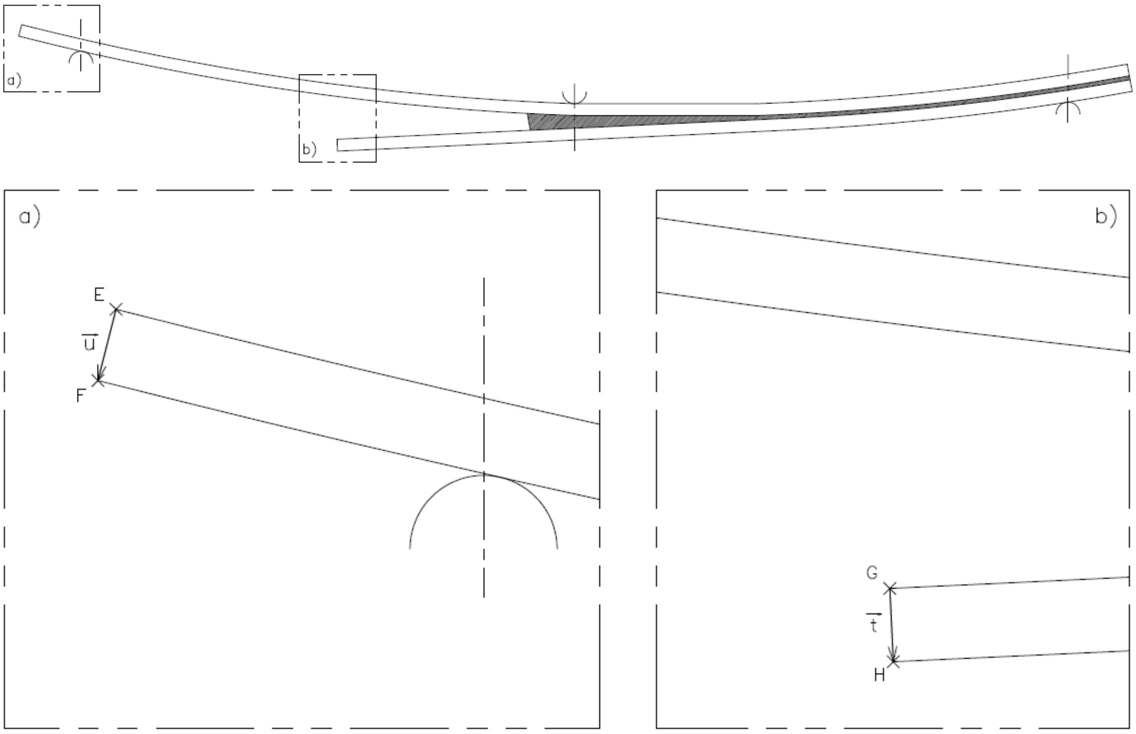

Figure 44 - Vector representation for Θ_P determination during the course of the test. a) upper adherend vector; b) lower adherend vector.

Furthermore, in order to relate both vectors, the vectoral product between the vectors *u* and *t* results in the vector *s*, expressed as:

$$\vec{s} = \vec{u} \wedge \vec{t} \text{ and} \tag{79}$$

$$\left|\vec{s}\right| = \sqrt{s_x^2 + s_y^2 + s_z^2} = \left|\vec{u}\right| \cdot \left|\vec{t}\right| \cdot \sin\left(\theta_P\right). \tag{80}$$

Therefore, rearranging the Eq. (80) in order to Θ_P, results in:

$$\theta_P = \arcsin\left(\frac{|\vec{s}|}{|\vec{u}|\cdot|\vec{t}|}\right). \tag{81}$$

Figure 45 shows the relative rotation between the two adherends at the loading line.

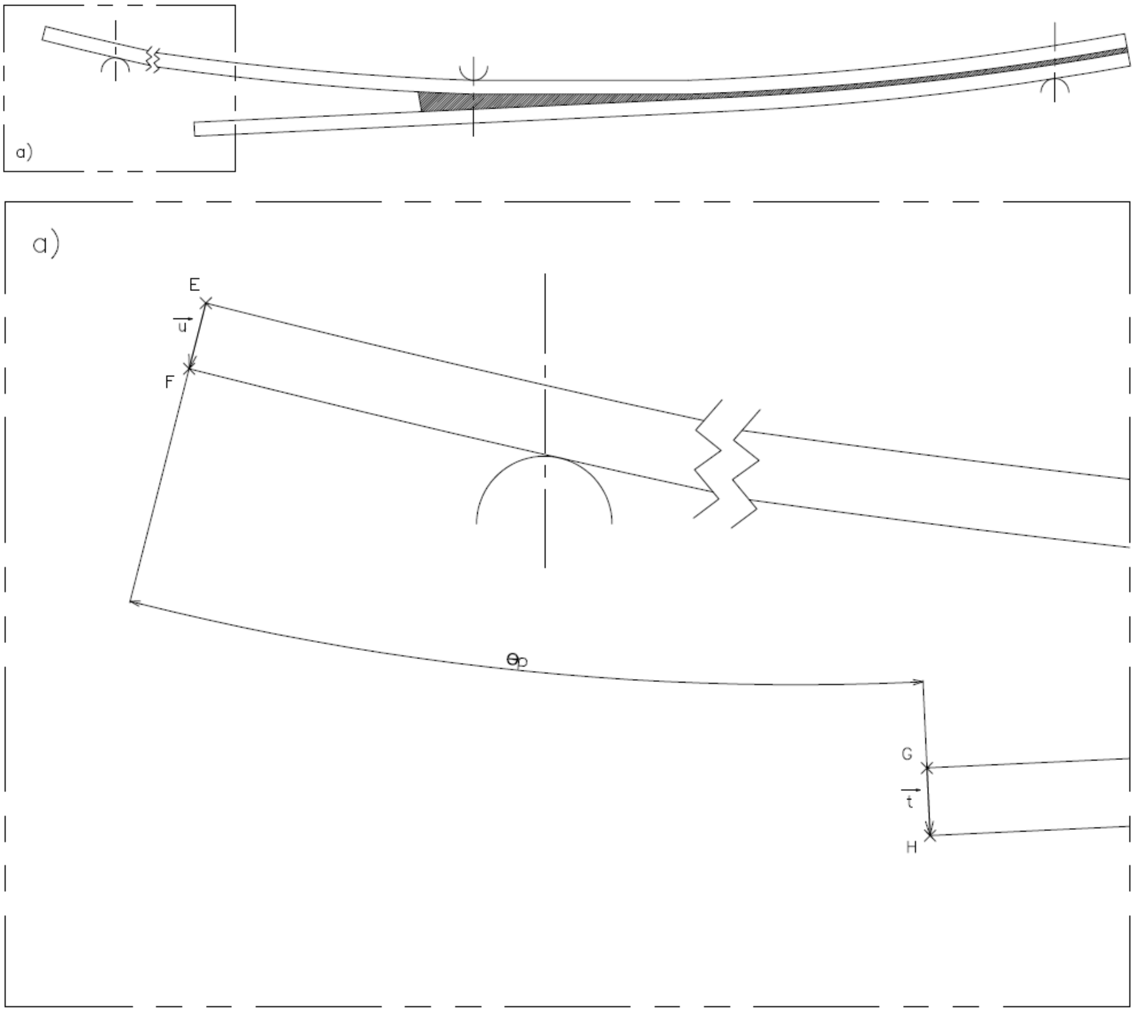

Figure 45 - Θ_P estimation through vectoral analytical approach, during the course of the test.

With this approach, the J_I values were in accordance with Santos [68] previous research, therefore, validating the vectoral approach.

3.3.1.2 Local normal separation between the two adherends at the cross-section of the crack tip (w_O)

The local normal separation is also referred in the literature as the normal separation between the bottom fiber of the upper beam and the top fiber of the lower beam. It is a parameter required to estimate J_I and σ by Eq. (69) and (71), respectively. To determine w_O, three virtual points were defined: A at the leftmost vertex of the upper fiber of the adhesive thickness, A’ immediately after point A to the rightmost side and B at the leftmost vertex of the lower fiber of the adhesive layer thickness (Figure 46).

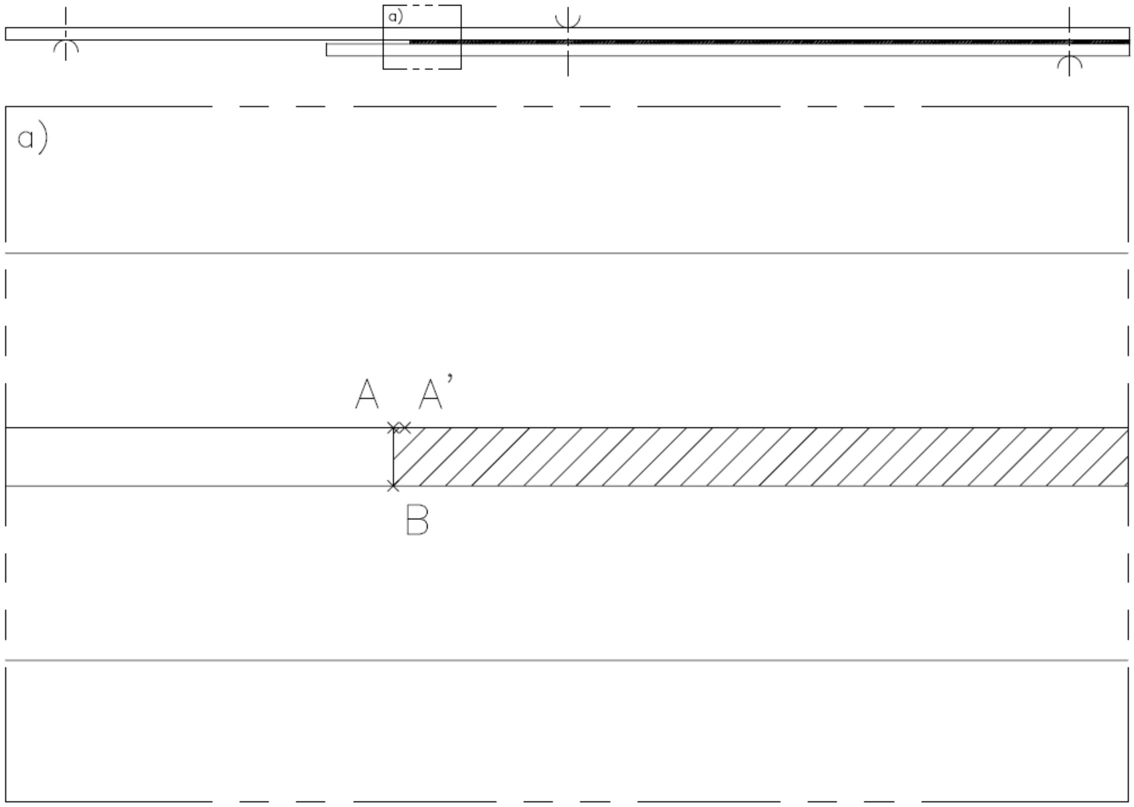

Figure 46 - Virtual points: A, A' and B for w_0 determination at the beginning of the test.

A line segment ($y = mx + b$) was established between the virtual point $A:\left(A_x, A_y\right)$ and $A':\left(A_x', A_y'\right)$ as $\overline{AA'}$. The slope (*m*) of the line segment $\overline{AA'}$ was obtained though:

$$m = \frac{\left(A_y - A_y'\right)}{\left(A_x - A_x'\right)}. \tag{82}$$

Furthermore, *b* as the value of *y* when *x* = 0, was obtained through:

$$b = A_y' - \left(m \cdot A_x'\right). \tag{83}$$

The chosen formulation for the minimum distance from a point to a line was:

$$d = \frac{ax_1 + by_1 + c}{\sqrt{a^2 + b_2}}. \tag{84}$$

Rewriting the line segment $\overline{AA'}$ equation according with Eq. (84) results in:

$$\overline{AA'}: y_1 = mx_1 + b \Rightarrow mx_1 - y_1 + b = 0, \tag{85}$$

and considering the virtual point $B:\left(B_x, B_y\right)$ as $B:\left(x_1, y_1\right)$, *d* may be expressed as:

$$d=\frac{mx_1-y_1+b}{\sqrt{m^2+\left(-1\right)^2}}. \qquad (86)$$

Therefore, the local normal separation between the two adherends at the cross-section of the crack tip, considering the adhesive thickness (t_A), was determined as (Figure 47):

$$w_0=d-t_A. \qquad (87)$$

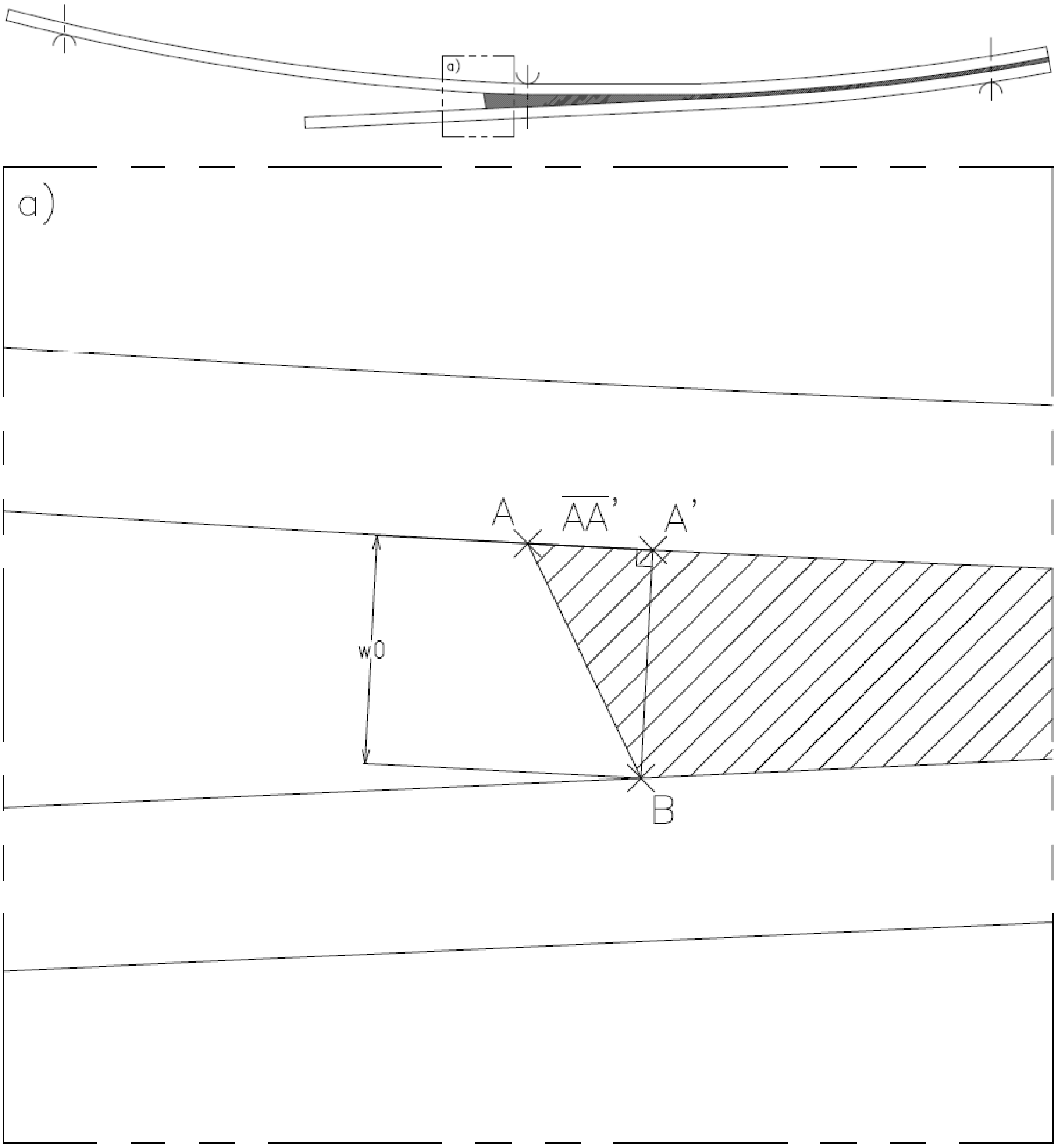

Figure 47 - w_0 estimation through geometric analytical approach, during the course of the test.

3.3.1.3 Local tangential slip between the two adherends at the cross-section of the crack tip (δ_0)

The local tangential slip is also referred, in the specialty literature, as the tangential slip between the bottom fiber of the upper beam and the top fiber of the lower beam. It is a parameter that directly influences J_{II} and τ, through Eq. (70) and (72), respectively.

The δ_0 parameter was analytically obtained by a geometrical approach, similarly to w_0. Three virtual points were established (A, A' and B), as represented in Figure 46. A line segment $\overline{AA'}$ was defined with *m* obtained through Eq. (82).

A line segment perpendicular to $\overline{AA'}$ was considered, expressed as:

$$\perp \overline{AA'}: y_1 = -\frac{1}{m}x_1 + b', \tag{88}$$

and the value of *b'*, defined by y_1 when $x_1 = 0$, deduced into:

$$b' = y_1 + \frac{x_1}{m}. \tag{89}$$

Following the Eq. (84) formulation for the minimum distance from a point to a line, rearranging the Eq. (88) accordingly, resulted into:

$$\perp \overline{AA'}: y_1 = -\frac{1}{m}x_1 + b' \Rightarrow \frac{1}{m}x_1 + y_1 - b' = 0, \tag{90}$$

and considering the virtual point $B:(B_x, B_y)$ as $B:(x_1, y_1)$, *d* may be expressed as:

$$d = \frac{\frac{1}{m}x_1 + y_1 - b'}{\sqrt{\left(\frac{1}{m}\right)^2 + 1^2}}. \tag{91}$$

Therefore, the distance between $\perp \overline{AA'}$ and $B:(B_x, B_y)$ represents the tangential slip between the adherends at the cross-section of the crack tip (δ_0), as shown in Figure 48:

$$\delta_0 = d \tag{92}$$

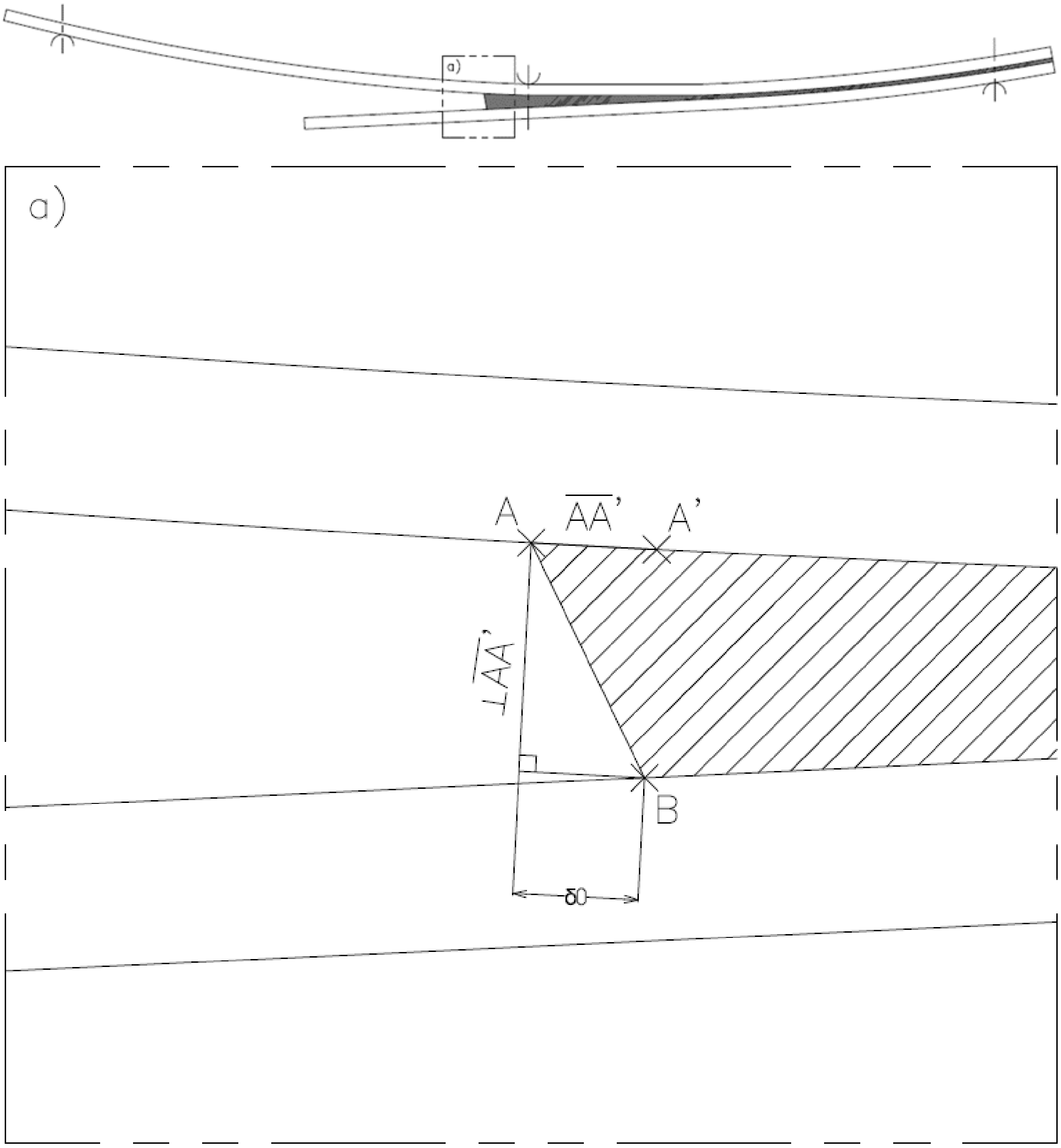

Figure 48 - δ_0 estimation through geometric analytical approach, during the course of the test.

3.3.2 Fracture analysis

The fracture analysis of each kind of adhesive was performed based on several graphical representations. Seven specimens were experimentally tested and numerically simulated for each kind of adhesive. The P-δ curves were obtained through experimental trials. The combination of the R curves, from the mode I and II, which were obtained by correlation of experimental and analytical parameters such as a, J_I and J_{II}, respectively. Furthermore, for one specimen, two formulations were used to obtain the R curves, Ji et al. [1] and Williams [48], in order to understand the deviations, between both approaches. The fracture envelope was obtained, considering the analytical parameters J_I and J_{II}. Lastly, both tensile and shear cohesive laws were estimated.

3.3.2.1 Araldite® AV138

The Araldite® AV138 adhesive, as previously referred in section 3.1.1.2.1, has a brittle behaviour. Therefore, it was expected, at the beginning of the numerical work, to achieve the lowest energy release rate value, independently of the mode, along the crack length, if compared with the other two kinds of adhesives.

3.3.2.1.1 J_C estimation

The J_C estimation, for mode I and II, was preceded by the experimental trials, from which the *P*-*δ* curves were obtained, as represented in Figure 49.

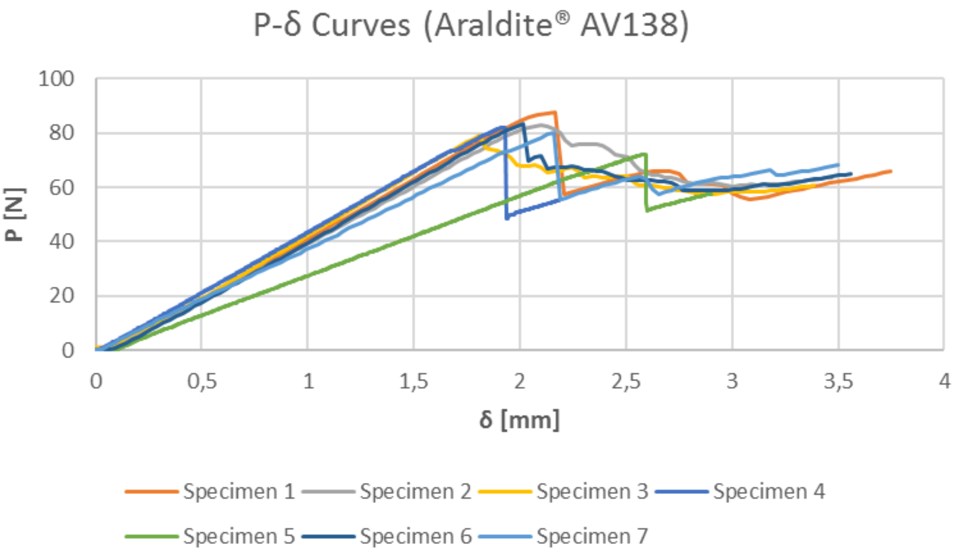

Figure 49 - Araldite® AV138 specimens *P-δ* curves.

By analysing the *P*-*δ* curves, it is possible to identify a linear pattern in the behaviour of the specimens up to a given value of *δ*, approximately in between 1.8 and 2.2 mm, coincident with the steep slope of the curve, with the exception of specimen 2, which does not evidence a clear slope, and instead a slight load decrease, immediately after the maximum load is achieved. This curve phenomenon is related with the crack propagation initiation, which significantly decreases the load of the specimen, denoting a brittle failure behaviour of the adhesive. However, it becomes nearly constant during the crack propagation.

The slope of the *P*-*δ* curves, up to the maximum load value of each specimen, is quite similar, which indicates that, in relation to stiffness, these feature similar behaviors, with the exception of specimen 5, whose slope is clearly lower, thus resulting in a lower value of the maximum load. On the other hand, the displacement, where the maximum load value is achieved, is higher in comparison with the other specimens, although this difference is not related with the lower stiffness but instead with the value of a_0, which is higher than for the other specimens.

Through Table 7 and Figure 49, it is possible to estimate that, considering the specimen 5 as excluded for the analysis, the specimens feature a maximum load value above 80 N for a short range of displacement, between 1.8 to 2.2 mm.

Table 7 - Maximum experimental values of P and δ for the Araldite® AV138.

Specimen No.	δ_{Pmax} [mm]	P_{max} [N]
1	2.17	87.77
2	2.10	82.76
3	1.81	79.00
4	1.92	82.16
5	2.60	72.15
6	2.01	83.38
7	2.16	80.20
Average	2.11	81.06
Standard deviation	0.23	4.46

After obtaining the experimental results, these were analyzed in order to estimate J_C, in modes I and II. The analysis was based on Ji et al. [1] approach, previously discussed in section 2.4.2.3, and represented through the specimens *R* curves.

Moreover, J_C was also estimated for mode I and II, based on Williams [48] approach, although only for one specimen, to understand and identify the differences between both formulations.

Figure 50 represents the *R* curves for mode I and II of a representative specimen, considering the Ji et al. [1] approach. By analyzing the *R* curves, it is possible to identify two geometrically similar curves, however, they feature different magnitudes. The mode I curve shows a higher energy release rate, during the crack propagation, than in mode II. This means that, under identical mixed mode conditions, the mode I, caused by tensile stresses, is not the major responsible for the failure of the adhesively-bonded joint, but the mode II, caused by shear stresses, since under these conditions, the energy release rate is lower, thus reducing the fracture toughness of the adhesively-bonded joint.

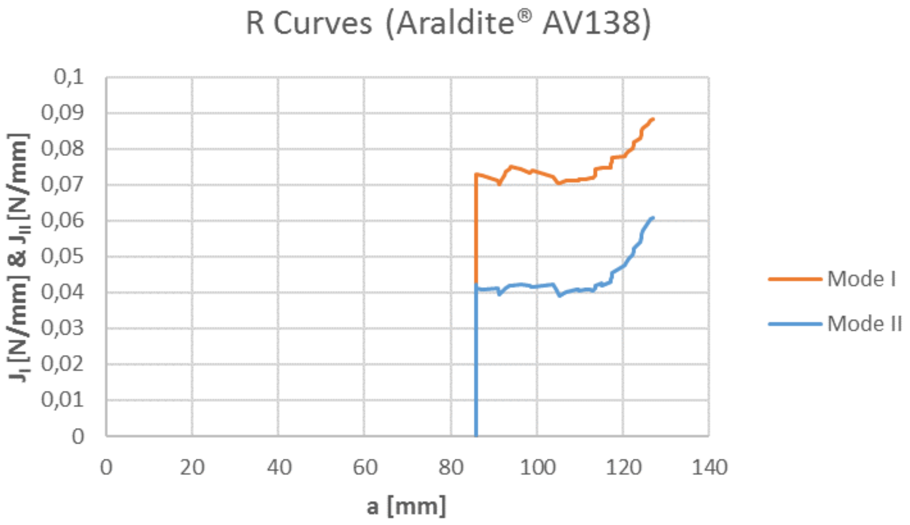

Figure 50 - Araldite® AV138 *R* curves obtained through Ji et al. [1] approach, relative to the specimen 2.

The *R* curves start at a pre-defined value of *a*, where the energy release rate instantaneously increases due to the crack propagation initiation. Thereafter, it remains nearly constant, creating a horizontal baseline, for a given interval (85 ≤ *a* ≤ 115), coinciding with the propagation of the crack. The horizontal baseline indicates that the adhesive features a stable behavior during the crack propagation.

Furthermore, for the assessment of J_I and J_{II}, it was only considered the horizontal baseline area of the *R* curve which is indicative of a crack propagation with constant J_I and J_{II}. These values are shown in Table 8 for all tested specimens.

Table 8 - Average values of J_I and J_{II} for the Araldite® AV138.

Specimen No.	J_I [N/mm]	J_{II} [N/mm]
1	0.0704	0.0422
2	0.0723	0.0411
3	0.0620	0.0372
4	0.0633	0.0410
5	0.0696	0.0431
6	0.0671	0.0426
7	0.0708	0.0439
Average	0.0679	0.0416
Standard deviation	0.0040	0.0022

According to Table 8, it is possible to verify that the J_I presents higher results than J_{II}, which confirms the SLB high preponderance for mode I. The low standard deviation for both mode I and II confirms the good repeatability of the specimens during the tests.

For the analysis of the *R* curves, the Williams [48] method was also considered. However, only for one specimen, this being the specimen 2. The *R* curves resulting from this method are shown in Figure 51 .

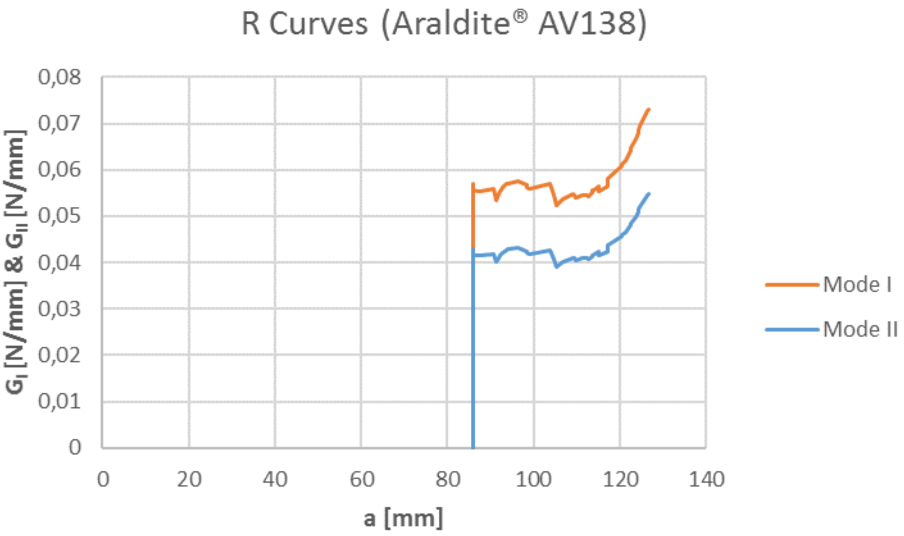

Figure 51 - Araldite® AV138 *R* curves obtained through Williams [48] method, relative to the specimen 2.

By analyzing the *R* curves of Figure 51 in comparison with Figure 50, it is possible to identify similarities in the overall shape of the curves. The mode II curves are almost identical. However, the mode I curves feature a magnitude difference despite its geometrical similarities. The horizontal baseline from the mode I curve (Figure 50) sits in between $0.07 \leq J_I \leq 0.08$, while in Figure 51 the mode I curve sits in between $0.04 \leq G_I \leq 0.05$. These deviations in the results can be justified by the different formulation between both methods. Ji et al. [1] method approaches the J_I assessment by only considering the load applied to the specimen during the course of the test and the relative rotation between both adherends at the loading line, as referred in section 2.4.2.3, without considering the material properties, such as the Young modulus of the adherend (*E*), or even other geometrical parameters from the SLB specimen, such as the adhesive thickness. Therefore, this magnitude deviation between J_I and G_I might be acceptable.

3.3.2.1.2 Fracture envelope

The overall J_C estimated results, for each specimen, are summarized in Figure 52. According to Figure 52, it is possible to confirm that the values referred to mode II feature a smaller absolute fluctuation than mode I, which is in accordance with the standard deviation differences as expressed in Table 8. The mode II line is almost horizontal while the mode I features some oscillations, resulting in a higher standard deviation. Nonetheless, it is possible to notice a consistency on the results, related with the JI and JII values. When, for the same specimen, the JI is higher, the JII is also higher, although with different value magnitudes. The exception is the specimen 2 since when the line of mode I trends upwards while, for mode II, it trends downwards. Moreover, comparing the consistency between both lines, it is possible to conclude that the crack propagation during the course of the test is smoother under mode II than mode I. Therefore, it is also possible to assume that shear stresses, under these circumstances, are more harmful than tensile stresses.

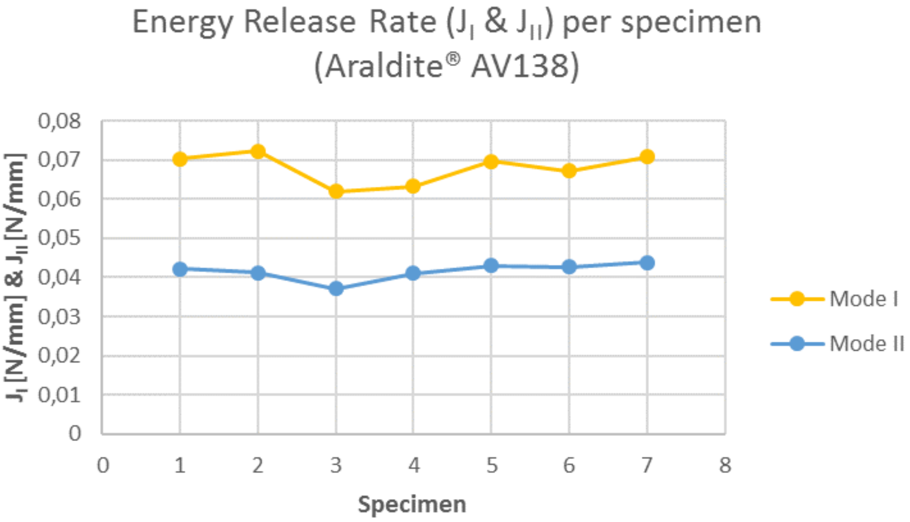

Figure 52 - Araldite® AV138 J_C estimation summary per specimen.

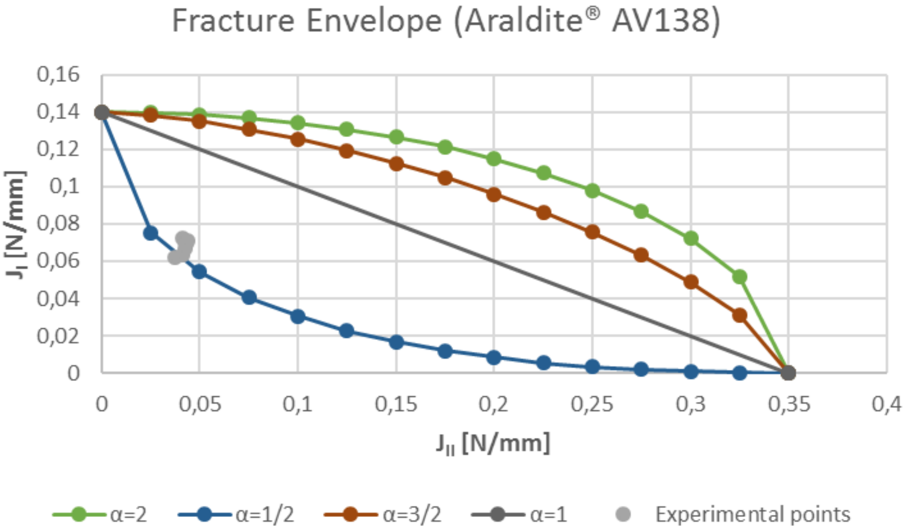

Figure 53 - Araldite® AV138 fracture envelope.

The fracture envelope, shown in Figure 53, was created based on the formulation from the Eq. (76) where several power law exponents (α) were considered. Furthermore, the

J_{IC} and J_{IIC} parameters were estimated through previous researches [63]. Analysing the fracture envelope from Figure 53, it is possible to verify that the experimental points, for all the specimens, are near each other, featuring low scatter. Moreover, these experimental points are also approximately near the power law exponent α=1/2. Therefore, it is acceptable to consider this parameter suitable for the crack propagation criterion, regarding the Araldite® AV138.

3.3.2.1.3 Cohesive law

The cohesive laws were obtained for mode I and II. The analytical formulation considered was based on Eq. (71) and (72). The cohesive laws are represented in Figure 54 and Figure 55. The values of t_n^0 and t_s^0, for each specimen, are expressed in Table 9.

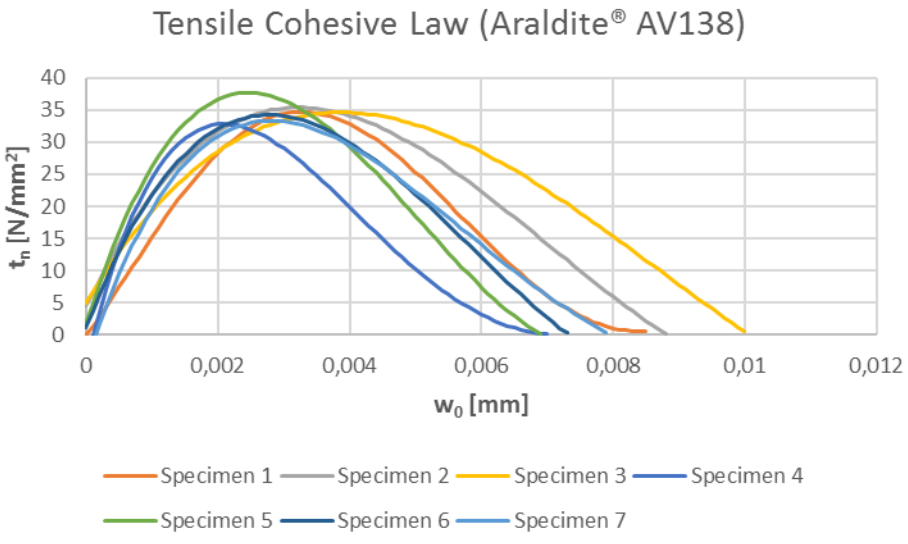

Figure 54 - Araldite® AV138 tensile cohesive law.

According to Figure 54, it is plausible to assume that the curves associated with each specimen resemble the concept of the triangular law, referred in section 3.2.2.1. It is also possible to see that the average tensile stress sits approximately around 35 N/mm², with the exception of the specimen 4 and 5, although the deviation between the maximum and minimum values is less than 5 N/mm², as it can be confirmed in Table 9. Regarding the w_0 at maximum load, when the maximum tensile stress is achieved, it does not significantly deviate between specimens, with the exception again of specimens 4 and 5. However, after the maximum tensile stress is reached, every curve features its own behaviour, resulting on different w_0 values after the adhesively-bonded joint failure. These unique behaviours are related with the degradation of each adhesive, which is also connected to the specimen manufacturing process.

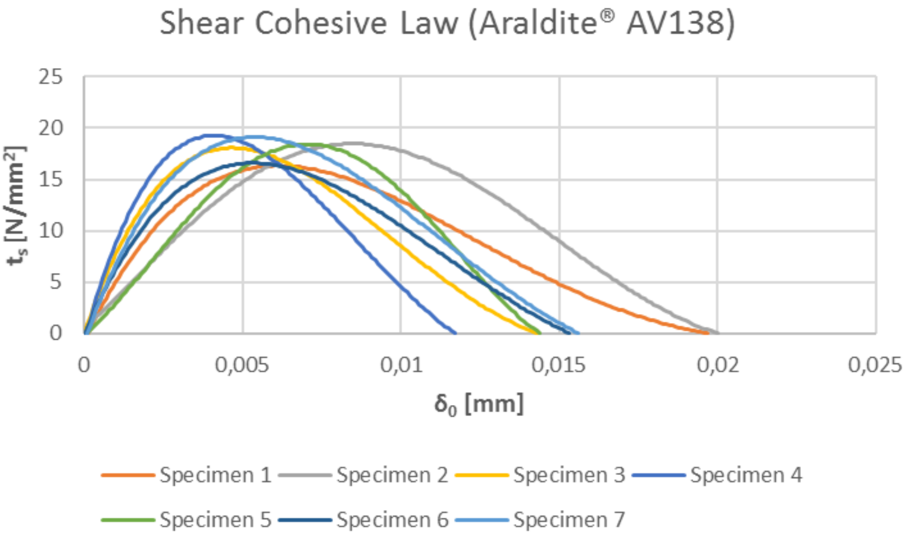

Figure 55 - Araldite® AV138 shear cohesive law.

Analyzing Figure 55, it is possible to identify geometrical resemblance between the shear and tensile cohesive law curves, although with different magnitudes. The shear stresses are almost twice lower than the tensile stresses, whereas the δ_0 at maximum load is nearly twice higher under shear conditions, as it can be confirmed in Table 9. This means that shear stresses develop during a longer displacement of the adhesive at the cost of a lower stress intensity. Despite this fact, the J_{II} values are lower than J_I.

Table 9 - Maximum values of t_n and t_s for the Araldite® AV138.

Specimen No.	t_n^0 [N/mm²]	w_0* [mm]	t_s^0 [N/mm²]	δ_0* [mm]
1	34.71	0.0033	16.33	0.0061
2	35.39	0.0032	18.48	0.0085
3	34.63	0.0039	18.07	0.0047
4	32.82	0.0021	19.28	0.0041
5	37.69	0.0025	18.43	0.0071
6	34.22	0.0028	16.60	0.0053
7	33.31	0.0028	19.12	0.0054
Average	34.68	0.0029	18.04	0.0059
Standard deviation	1.47	0.0005	1.07	0.0014

* At maximum load

In summary, based on Table 9, it is possible to conclude that, for the Araldite® AV138 adhesive, the t_n^0 value corresponds to approximately twice the t_s^0, whereas the inverse is valid for the parameters w_0 and δ_0 at maximum load, respectively.

3.3.2.2 Araldite® 2015

The Araldite® 2015 adhesive, as previously described in section 3.1.1.2.2, is a very well-balanced adhesive that features decent stiffness and ductility properties. As a result, it is expected that its behaviour sits in-between the Araldite® AV138 and Sikaforce® 7752. For all the analysis performed, the Araldite® 2015 adhesive will certainly be sitting in between, as a middle range adhesive.

3.3.2.2.1 J_C estimation

The first approach to the Araldite® 2015 adhesive, in order to evaluate its performance, when subjected to fracture conditions, was through the experimental *P*-*δ* curves, represented by the Figure 56, obtained for all the specimens.

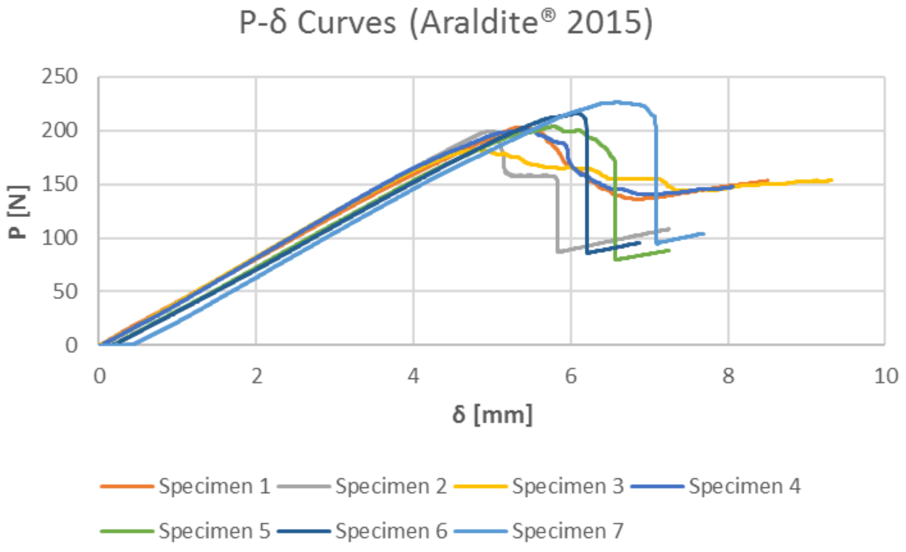

Figure 56 - Araldite® 2015 specimens *P*-*δ* curves.

Considering the *P*-*δ* curves, from the Figure 56, it is possible to identify three distinct behaviours among the seven specimens tested. The specimens 5, 6 and 7 feature a behaviour characteristic of ductile adhesives with the maximum loading value being reached at high displacement values but followed by an abrupt vertical slope, coincident with failure of the adhesive layer. On the other hand, specimens 1, 3 and 4 present an opposite behaviour, characteristic of brittle adhesives, since the maximum loading value is lower and it is reached for a lower value of displacement. Moreover, after failure of the adhesive, the loading value does not decrease abruptly but instead gradually. For the specimen 2, although its curve resembles a ductile behaviour, mainly due to the steep slopes, the maximum load value and displacement at which this value occurs are much lower than compared to the specimens 5, 6 and 7. Therefore, it is reasonable to consider it as a combination of ductile and brittle behaviours, similarly to the overall purpose of the Araldite® 2015 adhesive.

However, even considering that the overall geometry of the curves is dissimilar, in the initial phase of the experimental test, it is possible to identify a similar pattern among all of them. This pattern consists of a constant slope until the maximum load is reached, which means that all of the specimens featured equal stiffness.

Through Table 10 it is possible to confirm the fluctuation associated with the Araldite® 2015 adhesive, at the level of the maximum load and maximum displacement, in order to group the specimens that presented ductile and brittle behaviour.

Table 10 - Maximum experimental values of P and δ for the Araldite® 2015.

Specimen No.	δ_{Pmax} [mm]	P_{max} [N]
1	5.38	202.83
2	4.99	199.48
3	4.84	181.99
4	5.41	200.78
5	5.79	203.37
6	6.06	215.59
7	6.60	226.08
Average	5.58	204.30
Standard deviation	0.57	12.75

In summary, the Araldite® 2015 adhesive, due to its intermediate characteristics and properties, undergoes failure with minor plasticization. The fluctuation of the values obtained, evident in the values of the standard deviation and in the P-δ curves, are natural and expected in view of experimental procedure.

The second approach, followed by the assessment of the P-δ curves, was the analysis of the R curves, represented in Figure 57, where J_I and J_{II} were obtained through Ji et al. [1] method and a through the experimental digital recording, shown in section 3.1.2.3. For the analysis of the R curves, specimen 7 was chosen, as example, to characterise the adhesively-bonded joint performance. Based on the R curves from Figure 57, it is possible to identify a clear similarity between the mode I and II curves, although with different magnitudes. Due to the nature of the Araldite® 2015 adhesive, the horizontal baseline feature is not well defined throughout the test, which means that the crack propagation did not develop under stable conditions. In the absence of a clear horizontal baseline, the energy release rate, for both modes, was considered at the initial segment of the curves, when the slope of the curves began to decrease. The average values of J_I and J_{II}, registered on the unwell defined horizontal baseline, are represented in Table 11.

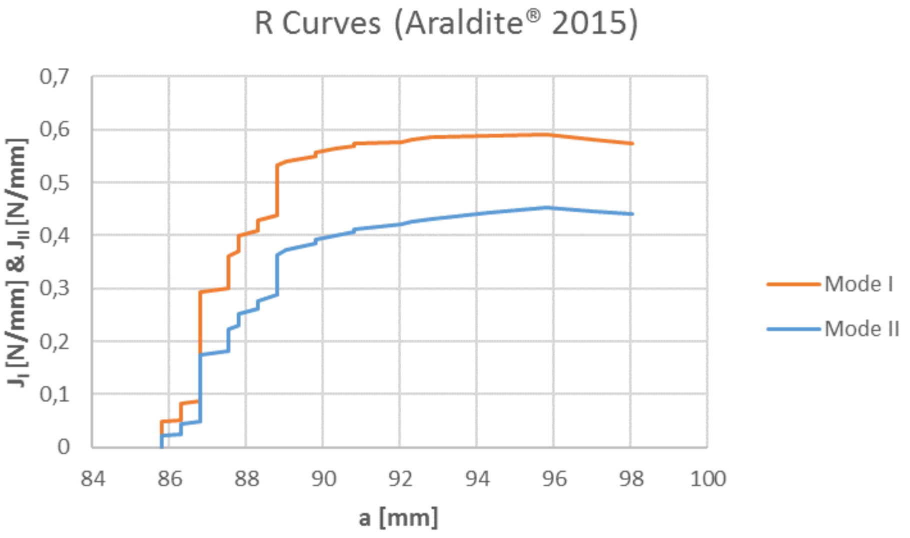

Figure 57 - Araldite® 2015 *R* curves obtained through Ji et al. [59] approach, relative to the specimen 7.

Table 11 - Average values of J_I and J_{II} for the Araldite® 2015.

Specimen No.	J_I [N/mm]	J_{II} [N/mm]
1	0.3878	0.2828
2	0.3716	0.2809
3	0.3791	0.2678
4	0.3882	0.2899
5	0.3986	0.3033
6	0.3837	0.2873
7	0.3677	0.2300
Average	0.3824	0.2774
Standard deviation	0.0098	0.0217

In summary, based on Table 11, it is possible to confirm that the mode I results are higher than mode II, which is line with the expected trend of SLB test, being more preponderant to tensile stresses. The standard deviation magnitudes translate the consistency of the specimens behaving similarly.

In order to consolidate the previous results, the global Williams [48] method was considered, as a comparison term between the two *J*-integral formulations, to obtain the J_I and J_{II}. In conjugation with the experimental values of *a*, it was possible to obtain the *R* curves, shown in Figure 58, referent to the specimen 7.

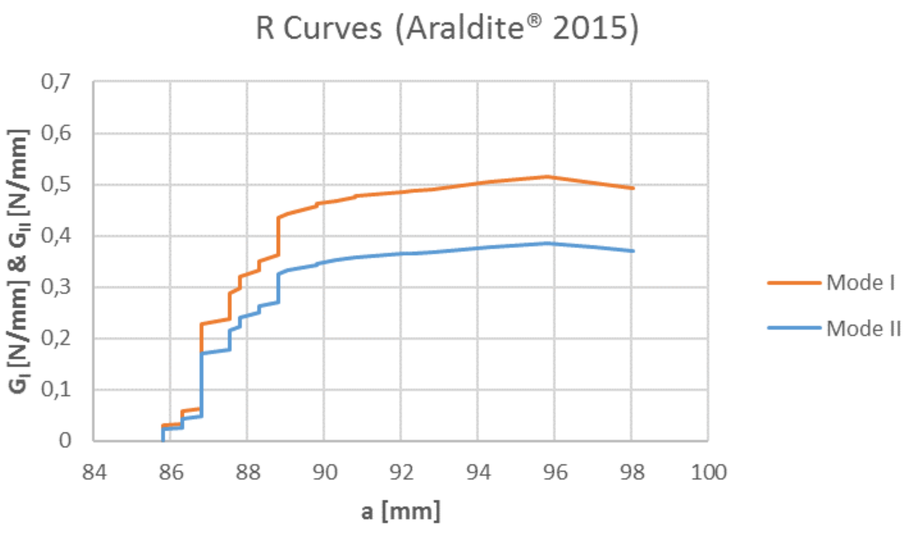

Figure 58 - Araldite® 2015 *R* curves obtained through Williams [47] method, relative to the specimen 7.

Through the *R* curves from Figure 58, it is possible to identify a clear resemblance in shape, comparing with the *R* curves from Figure 57. The main difference is the magnitude of the energy release rates of the mode I (J_I and G_I) and mode II (J_{II} and G_{II}). This magnitude deviation, which for this adhesive is not substantial, might be related with the *J*-integral formulation parameters, once the Ji et al. [1] method considers the specimens geometrical dimensions, that change during the course of the test, and the Williams [48] method considers mainly the material properties. Nonetheless, the repeatability of the energy release rate results, between both approaches, is very acceptable and consolidates the overall fracture analysis.

3.3.2.2.2 Fracture envelope

The graphical representation of the J_I and J_{II} values, related to the Araldite® 2015 adhesive, based on Table 11, is represented in Figure 59. Based on Figure 59, considering as an exception the segment of line connecting the specimens 2 and 3, it is possible to verify that the line segments have a slope, of different intensities, with the same direction, between the mode I and II. Furthermore, the fluctuation of the energy release rate is quite acceptable and if the J_{II} value of the specimen 7 was higher, above 0.25 N/mm, the results would be even more stable. Therefore, it is reasonable to consider that the overall specimens presented consistent results.

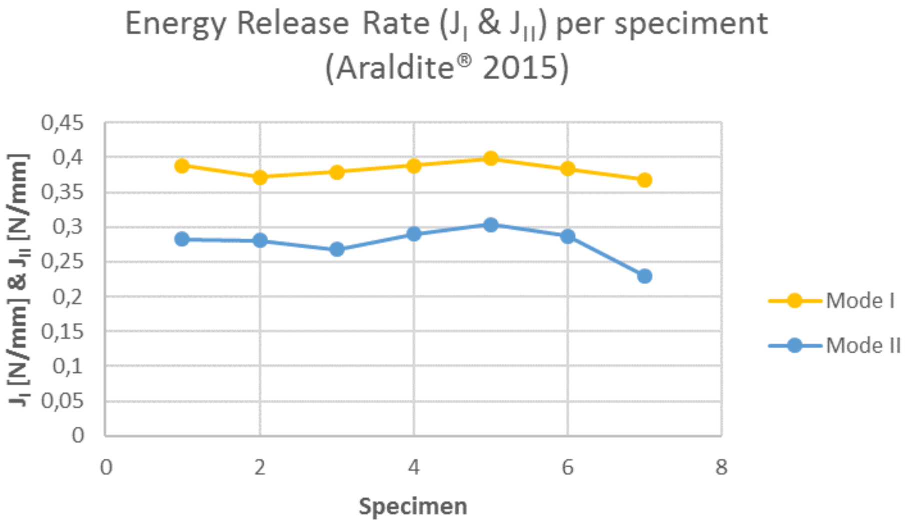

Figure 59 - Araldite® 2015 J_C estimation summary per specimen.

The fracture envelope, shown in Figure 60, aims to identify the most appropriate power law exponent (*α*) for the Araldite® 2015 adhesive. It is presented through a graphical representation, which relates the J_I and J_{II} values of each specimen in the form of experimental points. The segment of line that divides the envelope was established in past scientific research [63], while the curves, referent of *α*, around the segment of line, were obtained through the Eq. (76).

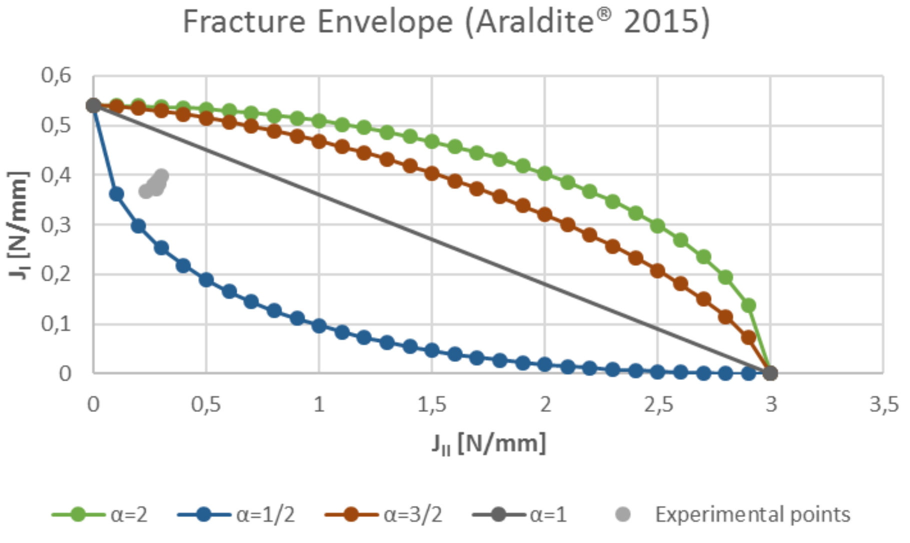

Figure 60 - Araldite® 2015 fracture envelope.

Based on Figure 60, it is possible to identify that all the experimental points, for each specimen tested, have a relatively low dispersion, which is in agreement with the stability and consistency of the energy release rate values for the mode I and II.

Moreover, it is also possible to identify that all these experimental points are presented in the lower part of the envelope, below the line segment, relatively near to the power law exponent α=1/2. In this way, it is possible to define that the power law exponent α=1/2 corresponds to the most appropriate solution for the Araldite® 2015 adhesive.

3.3.2.2.3 Cohesive law

The analysis of the cohesive laws, for both modes I and II, corresponds to one of the fundamental points for the assessment of the fracture toughness of adhesively-bonded joints, which in this case are composed by the Araldite® 2015 adhesive. These laws are based on the energy release rate that, through differential equations Eq. (71) and (72), develops in t_n and t_s. Combining these last parameters with the values of w_0 and δ_0, obtained through Eq. (87) and (92), referred in section 3.3.1, the cohesive laws can be represented in graphical form, as they are shown in Figure 61 and Figure 62.

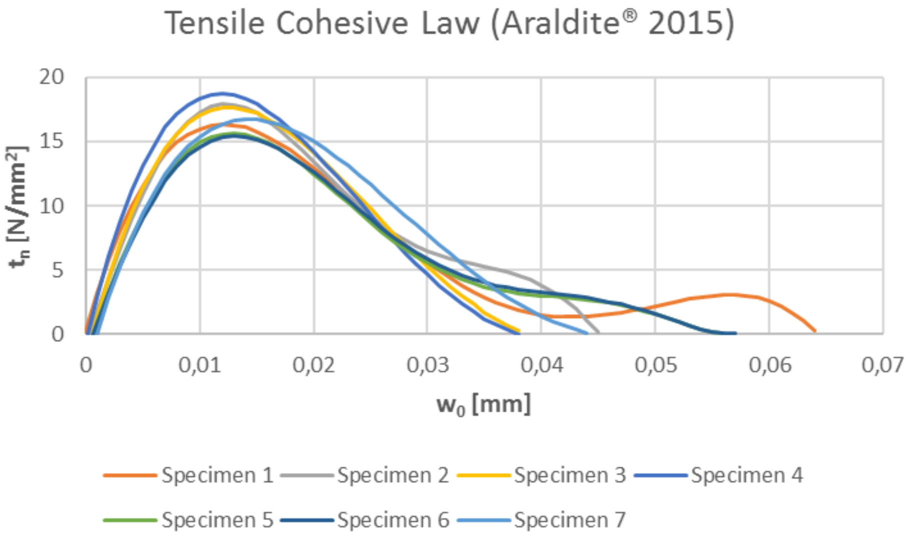

Figure 61 - Araldite® 2015 tensile cohesive law.

Based on the data of Figure 61, it is possible to visually identify the triangular model resemblances. Moreover, the curves related to each specimen behave fairly consistently throughout the overall test. In the initial stage, where the specimen behaviour is linear elastic, all feature a similar pattern, where the slope intensity of each curve defines the maximum t_n value, associated to a lower w_0 at maximum load. After the maximum t_n value is achieved, the curves began its degradation trend that, in accordance to the triangular model should be linear, like for instance the specimen 4, until the adhesive failure. However, since in this stage the regime is mainly plastic, the behaviour becomes somewhat random. The specimen 1 clearly evidences this phenomenon since just before the adhesive failure, the t_n value increases, enhancing the adhesive durability through a longer w_0.

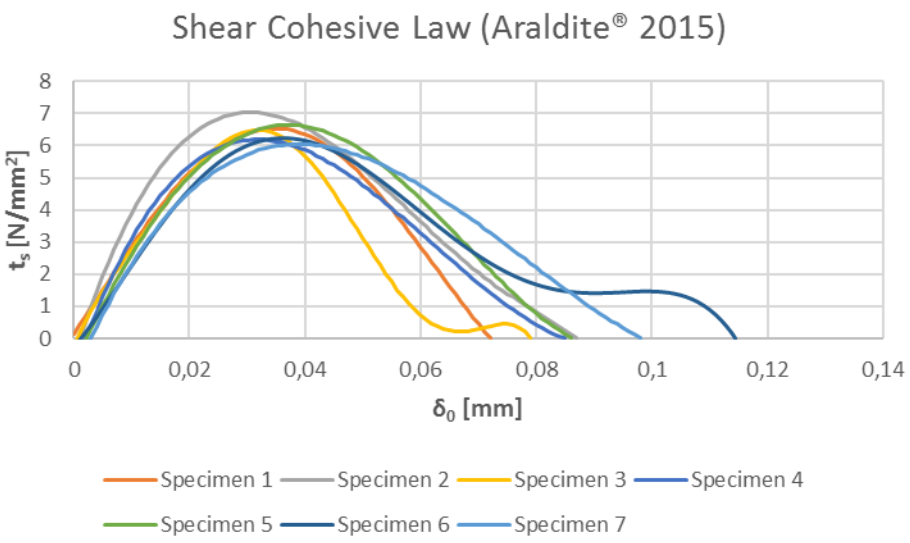

Figure 62 - Araldite® 2015 shear cohesive law.

Analysing Figure 62, related with the shear cohesive laws, it is possible to identify similarities on the shape of the curves, when comparing to Figure 61. Both laws resemble the pre-defined triangular model where the main difference between them is in the magnitude of the curves. At the initial stage, coincident with the linear elastic regime, all the curves, with the exception of specimen 2, feature an approximately similar slope intensity, thus resulting in consistent t_s values. The higher this value, the greater the slope intensity and the smaller the δ_0 at maximum load. Specimen 2 is distinct from the other curves mainly due to the high slope intensity, hence it is the specimen that has the highest t_s value. In the second half of the curves, where the degradation trend initiates, the curves behave differently due to the plastic regime that the adhesive features, after the maximum t_s is achieved. Some curves, such as that of specimen 1, behave linearly until the failure of the adhesive. In other curves, like that of specimen 3, just before failure, the adhesive resists and endures the shear stress for an additional displacement (δ_0).

Table 12 summarizes the overall data, related to the t_n^0 and t_s^0 with the w_0 and δ_0 at maximum load, respectively for all the specimens tested. Through Table 12, it is possible to interpret all the results from the cohesive laws, for both maximum tensile and shear stresses, where t_n^0 is more than the double of t_s^0 due to the higher SLB test preponderance for mode I. Furthermore, the standard deviation values, related to t_n^0 and t_s^0, are relatively low, which is in line with the specimen's consistency during the SLB test. The displacements, w_0 and δ_0 at maximum load, are inversely related to t_n^0 and t_s^0, respectively. The higher the value of maximum t_n^0, the lower the value of w_0, and this proportionality is also valid for t_s^0 and δ_0, respectively.

Table 12 - Maximum values of t_n and t_s for the Araldite® 2015.

Specimen No.	t_n^0 [N/mm²]	w_0* [mm]	t_s^0 [N/mm²]	δ_0* [mm]
1	16.31	0.0120	6.54	0.0350
2	17.87	0.0120	7.04	0.0310
3	17.60	0.0130	6.48	0.0320
4	18.71	0.0120	6.19	0.0320
5	15.62	0.0130	6.64	0.0370
6	15.42	0.0130	6.23	0.0360
7	16.71	0.0140	6.04	0.0390
Average	16.89	0.0127	6.45	0.0346
Standard deviation	1.13	0.0007	0.31	0.0028

* At maximum load

3.3.2.3 Sikaforce® 7752

The Sikaforce® 7752 adhesive, previously described in detail in section 3.1.1.2.3, presents as its main feature the ductility. This characteristic is far superior to the two other adhesives tested, especially the Araldite® AV138 adhesive, whose behaviour is brittle. Therefore, this adhesive is expected to exhibit high load resistance applied in line with a high displacement, resulting from the ductility of the adhesive. Hence, the energy release rate should also be quite high, for both mode I and II, during crack propagation.

3.3.2.3.1 J_C estimation

In order to characterize the fracture toughness of the Sikaforce® 7752 adhesive, an analysis was first performed on the P-δ curves, represented in Figure 63, resulting from the experimental trials. Based on the results of Figure 63, it is possible to identify that all the curves, referring to the test specimens, present similar behaviors, therefore similar stiffness. In an initial phase, the curves feature a linear behavior between the load and the displacement and, after the maximum load value has been reached, the load drops steeply, practically vertical, coincident with the adhesively-bonded joint failure.

Throughout the experimental results, expressed in Table 13, two specimens present slight deviations related to the load and displacement, namely specimens 4 and 6, whose values of maximum load and displacement, for the same instant, distance themselves from the average values. However, the difference is not significant in such way that it is necessary to discard these specimens for the analysis. In general, the experimental results confirm the ductility of the adhesive and therefore, the values correspond to the expectations.

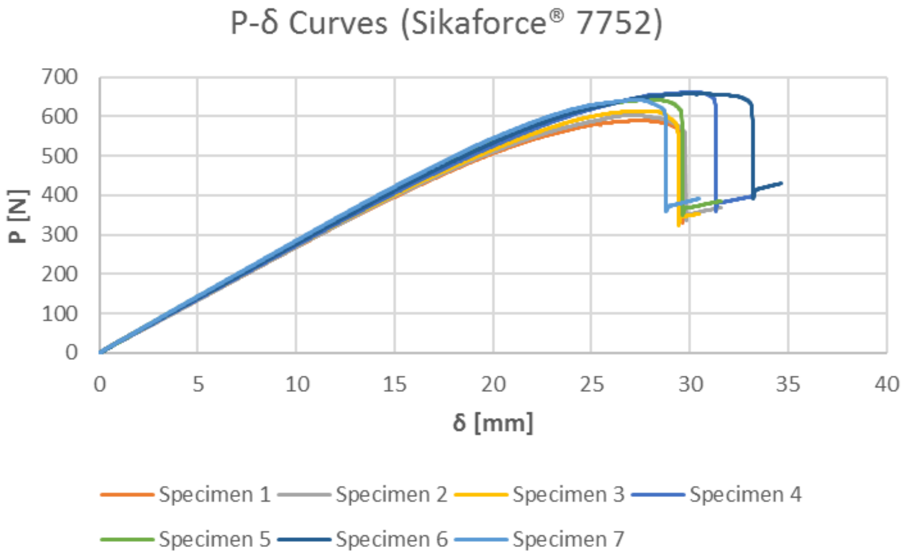

Figure 63 - Sikaforce® 7752 specimens *P-δ* curves.

Table 13 - Maximum experimental values of *P* and *δ* for the Sikaforce® 7752.

Specimen No.	δ_{Pmax} [mm]	P_{max} [N]
1	27.56	589.90
2	27.22	603.69
3	27.89	613.42
4	30.29	662.85
5	28.29	642.90
6	30.16	657.45
7	27.23	642.19
Average	28.38	630.34
Standard deviation	1.22	25.97

In summary, the reasonable low standard deviation value of *P* and *δ* confirms the similar behavior between the specimens. The adhesively-bonded joint endured high loading under a long period of displacement, averaging approximately 630 N and 28 mm, respectively.

After analyzing the experimental results through the *P-δ* curves, represented in Figure 63, the fracture toughness assessment of the Sikaforce® 7752 adhesive continued through the analysis of the *R* curves, for both mode I and II. The parameters J_I and J_{II} were obtained considering the Ji et al. [1] formulation and the parameter *a* measured on the specimen during the experimental trials, which combined, create the axis of the *R* curves. Figure 64 represents the *R* curve of specimen 2, used for reference.

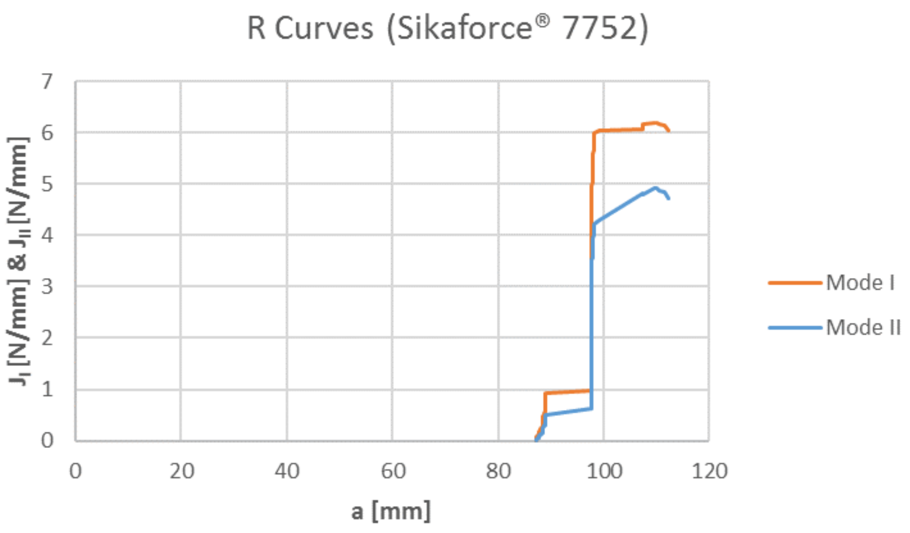

Figure 64 - Sikaforce® 7752 *R* curves obtained through Ji et al. [59] approach, relative to the specimen 2.

By evaluating the curve shown in Figure 64, it is possible to identify a characteristic behavior of the Sikaforce® 7752 adhesive, since a well-defined horizontal baseline is not evident in the curve. Instead, an abrupt transition is formed, with almost a vertical slope, of J_I and J_{II} for the same *a*. This behavior of the adhesive indicates that the crack propagation did not develop under constant J_I and J_{II} values. Furthermore, this effect is related to the high ductility of the adhesive, since it develops a plastically affected zone by propagating the crack of a considerable size, which in turn causes the effect of the loading punch to artificially increase the J_I and J_{II} values. Another common feature of the *R* curve is the different magnitudes between the mode I and II, being the mode I above the mode II.

Due to the adhesive behavior, considering that the horizontal baseline is not evident on the curves, the values of J_I and J_{II} were considered approximately at the crack propagation initial zone. These values are shown in Table 14. However, specimen 1 was discarded since, during the experimental trials, the specimen moved from the crack length recording device. Therefore, it was not possible to monitor the crack propagation during the overall experimental test.

Through Table 14 it is possible to confirm that the average mode I energy release rate is more relevant for the fracture toughness assessment, being approximately 3/4 higher than the mode II. However, the mode I feature higher standard deviation, being almost more than 2/3 considering the mode II.

Table 14 - Average values of J_I and J_{II} for the Sikaforce® 7752.

Specimen No.	J_I [N/mm]	J_{II} [N/mm]
1	-	-
2	3.4791	2.5633
3	3.5402	2.6488
4	3.2594	2.6720
5	3.3712	2.6110
6	3.3275	2.5158
7	3.4190	2.5203
Average	3.3994	2.5885
Standard deviation	0.1021	0.0659

As a term of comparison between different *J*-integral formulations, the Williams [48] method was used to determine the J_I and J_{II}, together with the parameter *a*, to obtain the *R* curves. The curves are represented in Figure 65, referent to specimen 2.

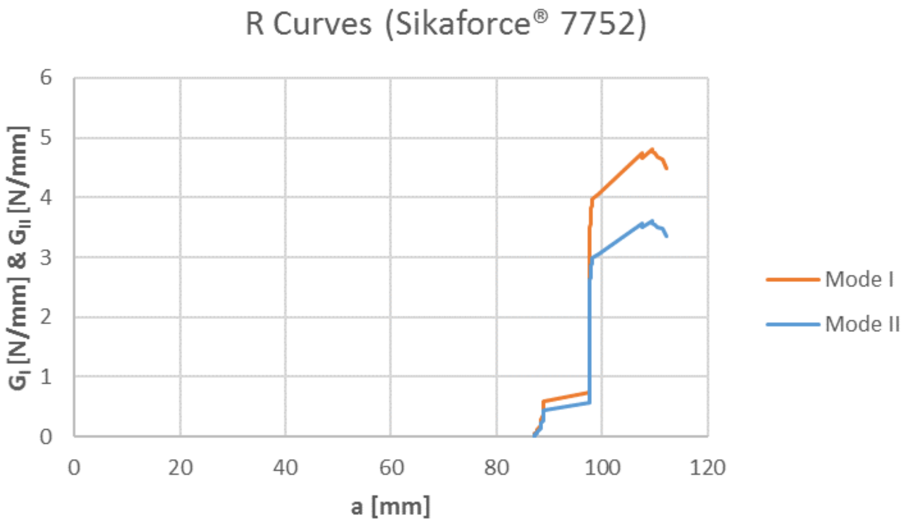

Figure 65 - Sikaforce® 7752 *R* curves obtained through Williams [47] method, relative to the specimen 2.

Based on the *R* curve of Figure 65, having as a comparison term the *R* curve from Figure 64, it is possible to evidence similarities and differences. Both *R* curves feature similar overall shapes, with a high slope, coincident with the initial crack propagation. Also, G_I is clearly higher than G_{II}. However, they differ in the energy release rate magnitude. Throughout the crack propagation, G_I and G_{II} presents approximately 1 N/mm less than J_I and J_{II}, respectively. This magnitude deviation might possibly be related with the formulation, especially for the mode I assessment, since Ji et al. [1] formulation does not include material properties nor SLB specimen parameters, when Williams [48] formulation does. However, the same cannot be applied for the mode II assessment since, both formulations consider the same parameters. Therefore, it is reasonable to assume that those parameters do not have significant impact on the formulation final result, for this ductile adhesive, and instead, the base formulation allows this magnitude deviation.

3.3.2.3.2 Fracture envelope

The values of J_I and J_{II}, referenced in Table 14, can be identified in Figure 66, for all the specimens tested, with the exception of specimen 1.

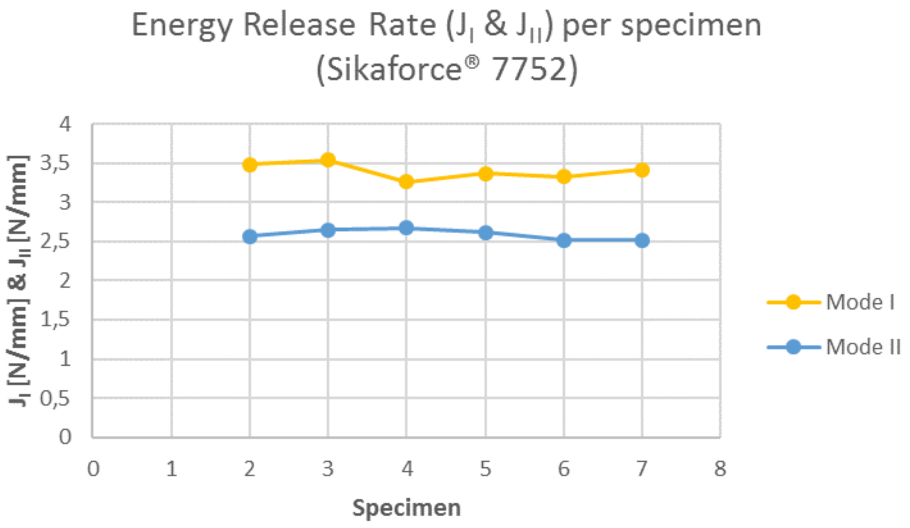

Figure 66 - Sikaforce® 7752 J_C estimation summary per specimen.

Figure 66 shows that it is possible to evidence that the energy release rate does not follow the same pattern between both modes. While the energy release rate increases from specimen 1 to specimen 2, for both modes, the same does not occur for the remaining specimens, especially when considering the behaviour of specimen 4. Specimen 4 features the minimum value of J_I for mode I, whereas for mode II, the value of J_{II} is the maximum recorded in all the specimens. Analysing each curve individually, from Figure 66, it is possible to confirm the standard deviation values from the Table 14. The low standard deviation values are graphically represented by an almost horizontal line, which links all the points referred to each specimen, with a small fluctuation. This means that the specimens behave similarly and the results obtained were consistent.

The fracture envelope represented in Figure 67 was created based on the J_I and J_{II} values, featured in Table 14 and graphically shown in Figure 66, as experimental points. The coordinates of the segment of line dividing the fracture envelope into two parts was established based on previous experimental works [63]. The curves were obtained through Eq. (76), considering three different power law exponents (α), which defines the geometry of the curves.

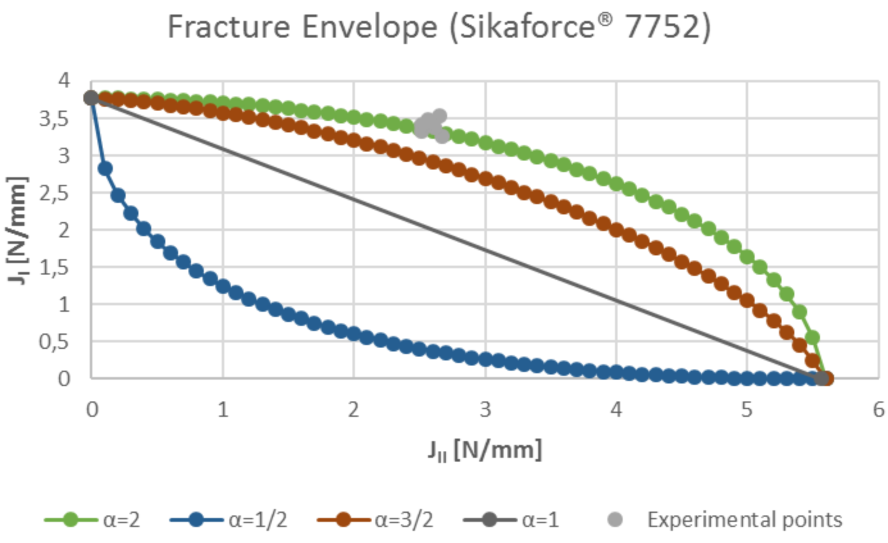

Figure 67 - Sikaforce® 7752 fracture envelope.

By analyzing the fracture envelope shown in Figure 67, it is possible to identify that the experimental points have a relatively small dispersion, demonstrating energy release rate consistency between all the specimens. Furthermore, the experimental points are approximately coincident with the curve referent to the power law exponent α=2. Therefore, it is reasonably to consider that this parameter represents the adhesive behavior and it is suitable for the Sikaforce® 7752 adhesive.

3.3.2.3.3 Cohesive law

The strength prediction of the adhesively-bonded joint was performed through the cohesive laws' representations shown in Figure 68 and Figure 69. In the ordinate axis, the t_n and t_s parameters were obtained through Eq. (71) and (72), considering the obtained results from section 3.3.2.3.1. The abscissa axis parameters, composed by w_0 and δ_0, were estimated through the Eq. (87) and (92), respectively. For this analysis, similarly to the J_C estimation, specimen 1 was not considered.

Analyzing the tensile cohesive laws depicted in Figure 68, it is possible to identify two distinct behaviors. Coincident with the initial crack propagation process, the tensile stress almost immediately reaches its maximum value, above 5 N/mm^2, for all specimens, considering a fluctuation approximately in between $5.3 \leq t_n \leq 6.2$ N/mm^2. After the maximum tensile stress is achieved, the curves feature a long decreasing trend, until failure of the adhesively-bonded joint, reaching the maximum w_0. This behavior is characteristic of ductile adhesives, which endures high stresses over a long period of deformations. However, the longest the deformation (w_0) at maximum load, the longest is the crack propagation and, considering the fluctuation of the curves in this stage, the crack might propagate, during the course of the test, under unstable conditions.

Furthermore, due to the two distinct behaviors, the typical triangular model shape is not clearly evident since the maximum t_n value is achieved at an early stage of w_0 and the minimum t_n value at a final stage of w_0.

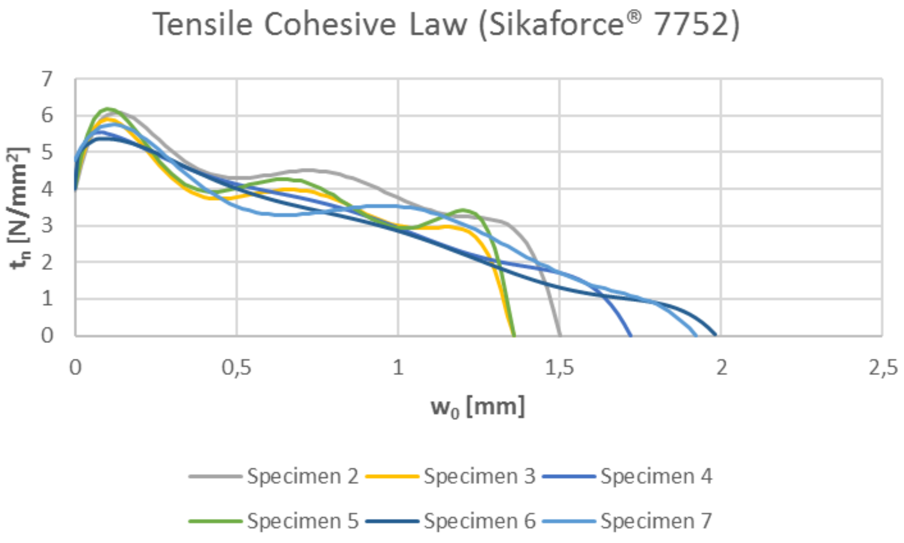

Figure 68 - Sikaforce® 7752 tensile cohesive law.

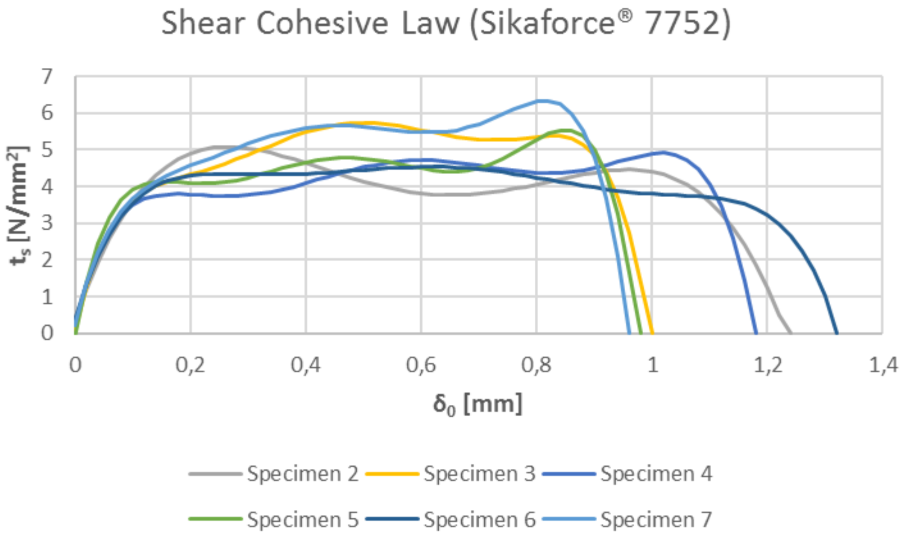

Figure 69 - Sikaforce® 7752 shear cohesive law.

According to Figure 69, it is possible to identify a set of curves with peculiar shapes, associated to the behaviour of ductile adhesives, when solicited to shear stresses. The existence of a predominant pattern is not evident and, instead, each specimen curve behaves differently. Moreover, none of the curves resembles the triangular model shape described in section 3.2.2.1 and the maximum shear stress is not recorded in the initial crack propagation stage but, instead, through the course of the test. The curves present, in an initial stage, an increasing trend and, in the final stage, a decreasing tendency of the shear stress. In this way, the curves present a behaviour approximately constant during these intervals, despite of the fluctuation, in some specimens very excessive, of the values of the shear stress. Due to the nature of the adhesive, t_s^0 may occur in an initial or final stage of the test, resulting in spread values of δ_0 at maximum load. The data associated with the cohesive laws are presented in Table 15.

Table 15 - Maximum values of t_n and t_s for the Sikaforce® 7752.

Specimen No.	t_n^0 [N/mm²]	w_0* [mm]	t_s^0 [N/mm²]	δ_0* [mm]
1	-	-	-	-
2	6.08	0.12	5.08	0.26
3	5.90	0.10	5.74	0.50
4	5.53	0.08	4.91	1.02
5	6.18	0.10	5.54	0.86
6	5.35	0.10	4.53	0.62
7	5.75	0.12	6.33	0.82
Average	5.80	0.10	5.36	0.68
Standard deviation	0.29	0.01	0.59	0.25

* At maximum load

Based on the data of Table 15 it is possible to verify that both tensile and shear stresses maximum values are within the same magnitude, however, these values are not reached in the same deformation instance since the average t_n^0 is registered at the initial stage (w_0=0.10 mm) and the t_s^0 in the middle stage (δ_0=0.68 mm) of the experimental test. Moreover, the standard deviation of the average t_s^0 is twice higher than t_n^0 value and the mode II deformation fluctuation is twenty-five times higher than mode I deformation. In summary, it is reasonable to consider that the crack propagation is more stable under mode I conditions with a lower fluctuation of the stresses during the course of the experimental test, since the nature of the Sikaforce® 7752 adhesive is mainly ductile.

3.3.3 Data analysis

The analysis of the results contemplates the comparison between the three adhesives studied: Araldite® AV138, Araldite® 2015 and Sikaforce® 7752. These were compared according to the topics described in section 3.3.2, namely P-δ curves, J_I and J_{II}, R curves, fracture envelopes, and cohesive laws. Furthermore, this data analysis also considers the comparison with the literature of Santos and Campilho [63] and Nunes and Campilho [76], specifically in regard to the energy release rate for both modes I and II, where the adhesives studied were the same.

The maximum load of the adhesively-bonded joint is directly related to the mechanical properties of the adhesive. Through Figure 70, it is possible to identify the distinct behaviour of each adhesive when submitted to an experimental SLB test. The P and δ values represent the strength and ductility, respectively, of the adhesive throughout the experimental trail.

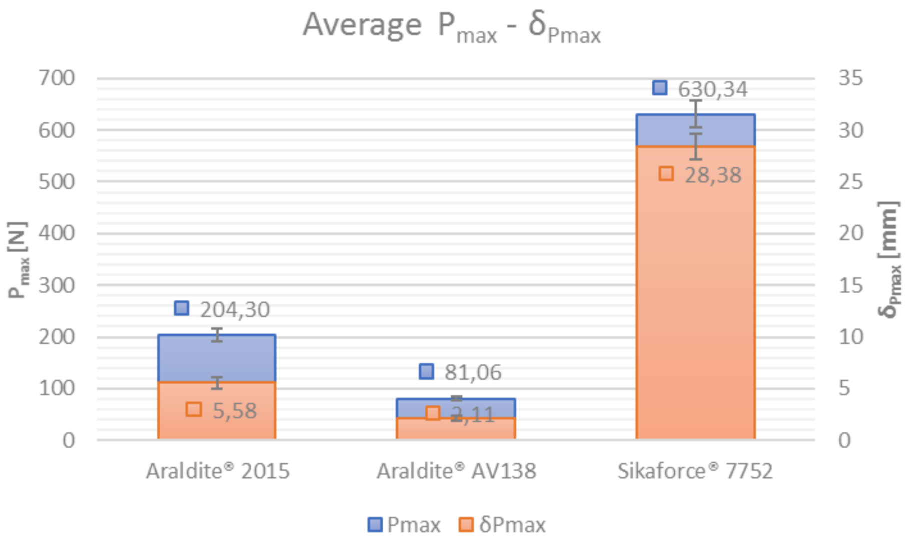

Figure 70 - Average P_{max} - δ_{Pmax} values for each adhesive tested.

Based on Figure 70, it is evident that the Sikaforce® 7752 adhesive outperforms the other adhesives due to its higher loading resistance, related to its ductile characteristic behaviour, whereas the Araldite® AV138 adhesive underperforms by a significant magnitude, due to its brittle behaviour. The Araldite® 2015 adhesive, which is considered as a middle term adhesive, sits in between the other two, with a performance improved over the Araldite® AV138 but far away from the Sikaforce® 7752. The δ_{Pmax} is clearly higher on the Sikaforce® 7752 adhesive than the rest, which is directly related to the adhesive ductile behaviour. On the other hand, the adhesive Araldite® AV138, which features a brittle behaviour, presents a much reduced δ_{Pmax}.

In regard to the energy release rate, the Figure 71 showcases the overall view of the three adhesives performance. It is possible to identify graphical similarities with the Figure 70, considering that, in both representations, the Sikaforce® 7752 adhesive features the higher strength and energy release rate, whereas the Araldite® AV138 adhesive features the lower values. The Sikaforce® 7752 adhesive, during the course of the experimental test, features high resistance to the tensile and shear stresses, translated into higher strength, throughout the displacement constant increase, which means that adhesive is gradually releasing energy for a long period of displacement. On the other hand, the Araldite® AV138, due to its brittle behaviour and lower displacement values, features a lower energy release rate, coincident with the premature failure of the adhesive. In general, the higher the adhesive ductility, the higher the energy release rate. The Araldite® 2015 adhesive, due to its nature, not being a native ductile of brittle adhesive, features results in between the other two adhesives.

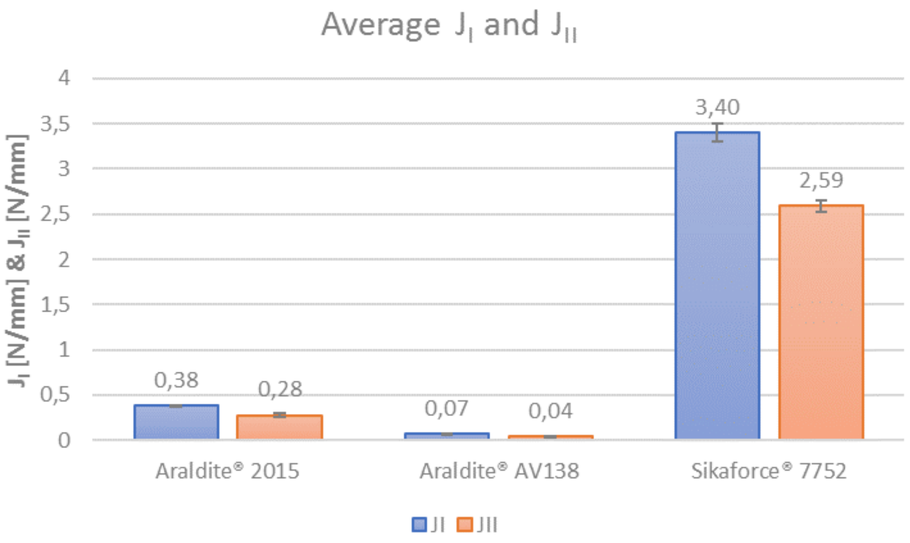

Figure 71 - Average J_I and J_{II} for each adhesive tested.

Regarding the gap between the J_I and J_{II}, despite the energy release rate magnitude, the difference is clearly higher in the brittle Araldite® AV138 adhesive, being J_{II} approximately 43% less than J_I. In the other two adhesives, having a higher difference between J_{IC} and J_{IIC}, with an increasing relative preponderance of J_{IIC}, the value of J_{II} is only approximately 25% lower than J_I.

In an alternative perspective, J_I and J_{II} may be presented in the form of fracture envelopes, in order to characterize the behaviour of each adhesive. The fracture envelopes are presented in Figure 53, Figure 60 and Figure 67. It is possible to identity the two distinct behaviours, ductile and brittle, of the three adhesives. The brittle Araldite® AV138 adhesive behaves near to the power law exponent α=1/2, while the ductile Sikaforce® 7752 adhesive behaves near α=2. The Araldite® 2015, due to its energy release rate similar results to the Araldite® AV138 adhesive, also behaves near to the α=1/2.

In relation to the maximum tensile and shear stresses, to which the adhesive is subjected during the course of the test, Figure 72 presents an overview of the results, for each adhesive.

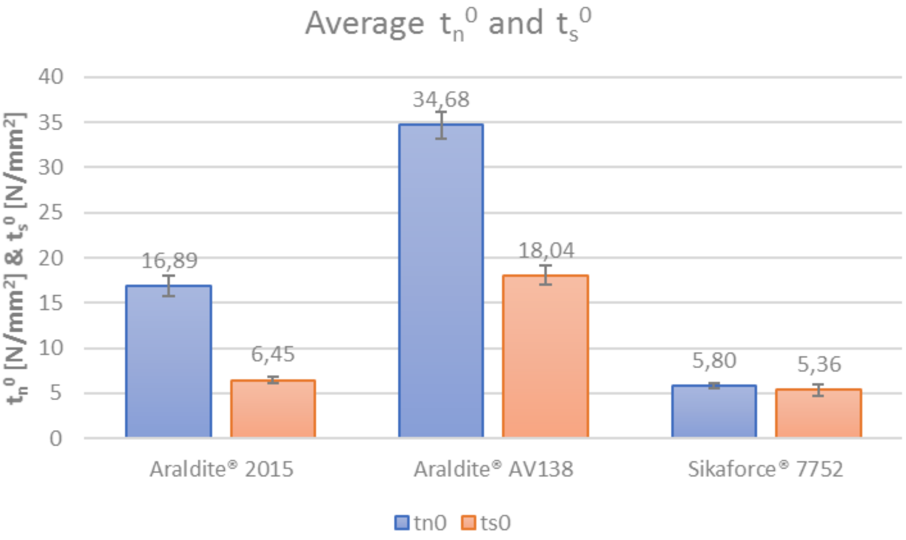

Figure 72 – Average maximum tensile and shear stresses values, for each adhesive tested.

Analysing Figure 72, it is possible to verify that the Araldite® AV138 adhesive shows the best results, in relation to the tensile and shear stresses, followed by the Araldite® 2015 adhesive and finally the Sikaforce® 7752 adhesive. The Araldite® AV138 adhesive, although brittle, is also considered as quite strong, hence the values of tensile and shear stresses are quite high compared to the others. On the opposite side is the ductile adhesive Sikaforce® 7752 which, does not present the stiffness levels of the Araldite® AV138 adhesive, hence the considerable difference of results. On the other hand, the Araldite® 2015, as it presents a mixed behaviour between brittle and ductile, features intermediate results.

Regarding the difference between the maximum tensile and shear stresses for each adhesive, in the case of the Araldite® AV138 adhesive, the difference is significant, as with the Araldite® 2015 adhesive. However, for the Sikaforce® 7752 adhesive, the difference between the stresses is residual. Considering the case of the Araldite® AV138 and 2015 adhesives, the maximum shear stress values represent approximately 48% and 62%, respectively, of the maximum tensile stress values. However, for the Sikaforce® 7752 adhesive, the overall performance is different since there is a balance between the tensile and shear stresses to which the adhesive is subjected, although these values are much lower, compared to the other two adhesives.

Figure 73 represents the standard deviation percentage for all the parameters used through the fracture analysis, considering the 7 specimens tested, for each adhesive. This graphical representation showcases the consistency and repeatability of the tests performed. It is possible to verify that only two parameters, w_0 and δ_0, are above the mark of 15%. Therefore, it is reasonable to consider that the data gathered features high consistency and repeatable results. The other two parameters that shown unusual fluctuation are related to the adhesives' unpredictable behaviour, especially for the ductile Sikaforce® 7752 adhesive.

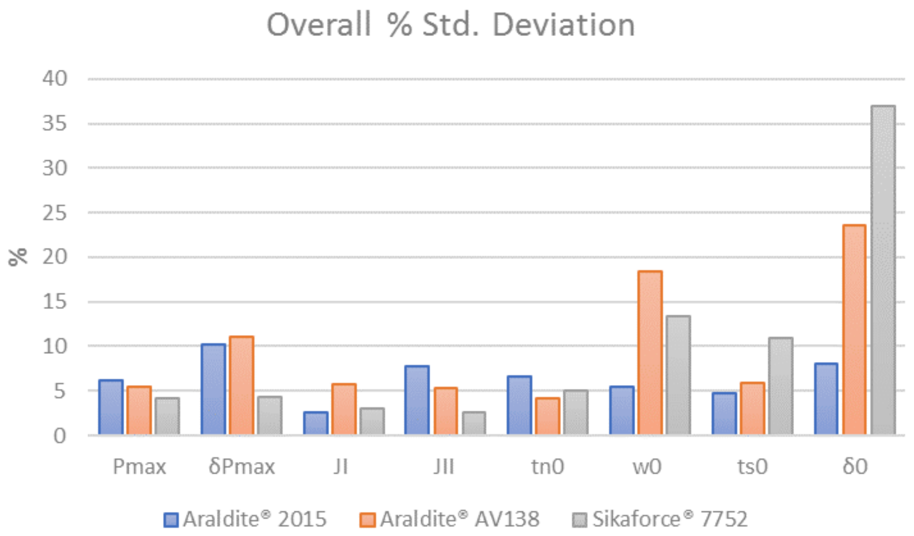

Figure 73 - Overall standard deviation percentage for the parameters used for the facture analysis.

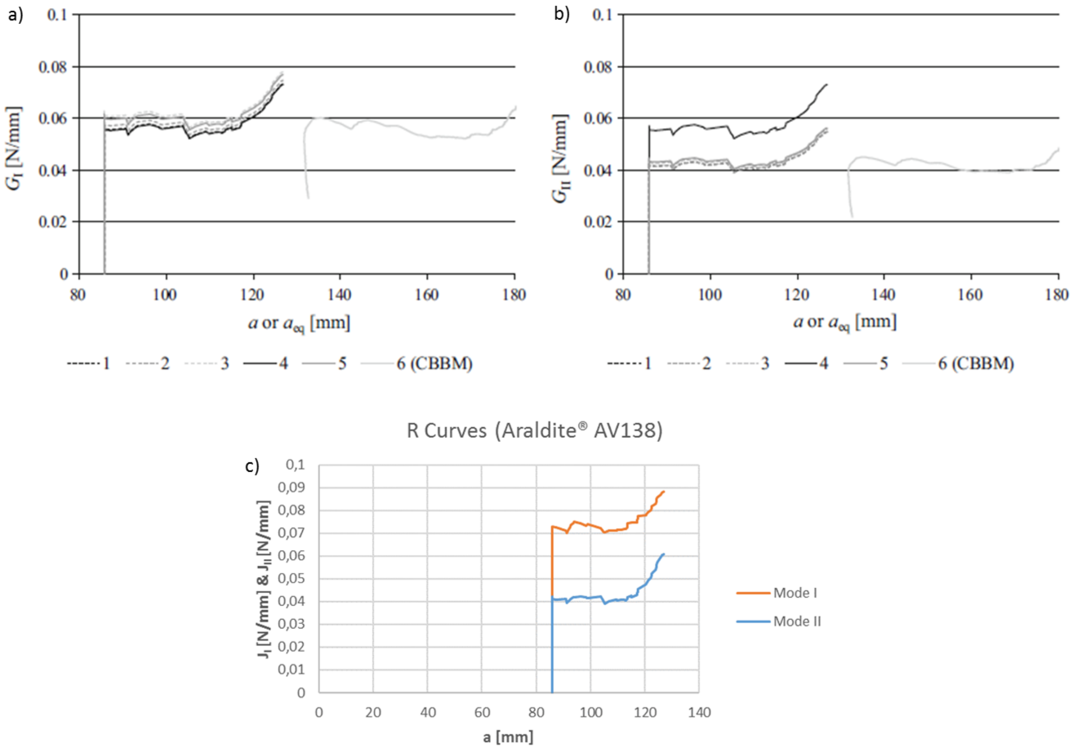

Figure 74 - Specialty literature *R* curves comparison, for Araldite® AV138: a) Mode I [63]; b) Mode II [63]; c) Mode I and II obtained in this work.

In regard to the specialty literature, Figure 74 showcases the *R* curves comparison with Santos and Campilho [63], for the Araldite® AV138 adhesive. It should be noted that

Santos and Campilho [63] used different formulations to obtain the energy release rate, through model 1 to 6. However, the latter (CBBM) will not be considered as a term of comparison due to the geometry of the curve. By analysing the *R* curves represented Figure 74, it is possible to identify two obvious similarities, the shape and magnitude of the *R* curves. Regarding the shape, both feature a well-defined horizontal baseline, with a reasonable fluctuation, which allows to predict a stable crack propagation. Concerning the magnitude of the horizontal baseline, for mode I, the model 5 studied by Santos and Campilho [63] is the closest to the Ji et al. [1] formulation, although there is a difference of approximately 0.01 N/mm. For the mode II, discarding the model 4, all models present fairly similar results with the Ji et al. [1] formulation.

For the Araldite® 2015 and Sikaforce® 7752 adhesives, the *R* curves also feature fairly approximate similarities to the shape of the curves and magnitude of the horizontal baseline between the formulations studied by Santos and Campilho [63] and Ji et al. [1] formulation. Therefore, it is reasonable to consider the Ji et al. [1] formulation as a valid and solid alternative solution for the assessment of the energy release rate, for mixed mode conditions and SLB designed adhesively-bonded joints.

Another way to characterize the behaviour of adhesives under mixed-mode conditions, by the energy release rate, is through fracture envelopes. Figure 75 shows three envelopes associated with the Araldite® 2015 adhesive, obtained by different formulations and also distinct tests.

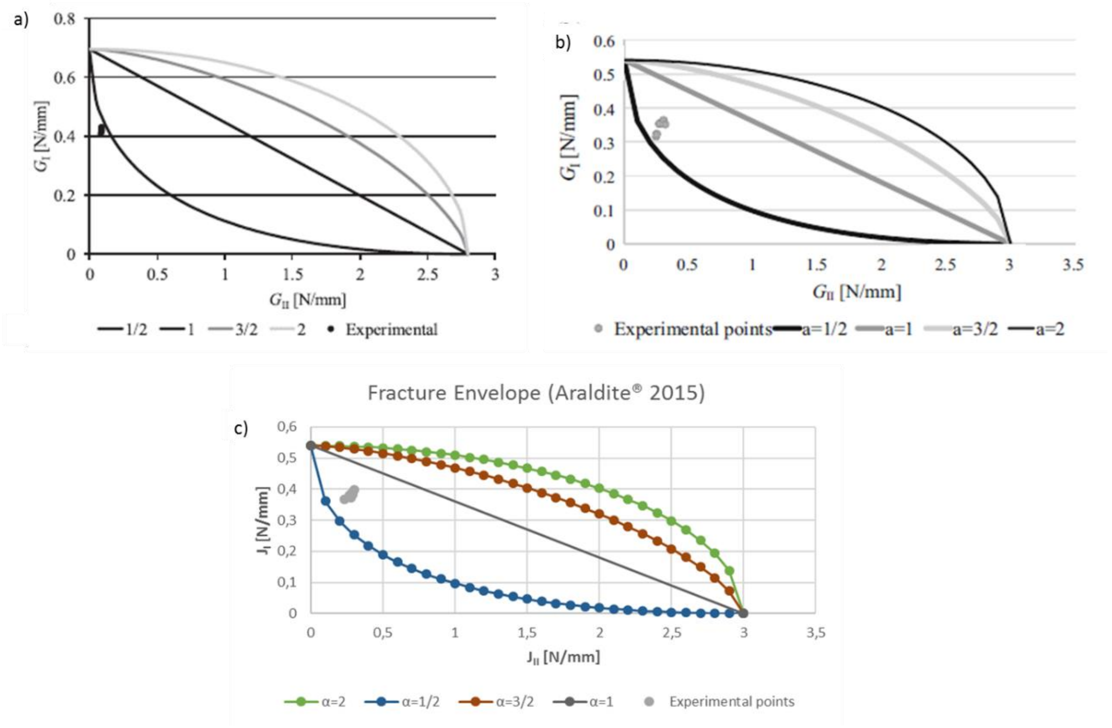

Figure 75 - Specialty literature fracture envelopes comparison, for Araldite® 2015: a) Nunes and Campilho [76]; b) Santos and Campilho [63]; c) Ji et al. formulation calculated in this work [1].

The envelope a) was obtained through an ATDCB test [76], b) considering the SLB test and formulated based on CBBM data and, c) also considering the SLB test but with a different formulation for the assessment of the energy release rate, which was Ji et al. [1] formulation.

All three envelopes feature low dispersion of the experimental points and are relatively close to the power law exponent α=1/2. However, for the envelopes b) and c), these experimental points are above the curve α=1/2, whereas the envelope a) is below. This difference is related to the experimental test, since the latter envelope was obtained through ATDCB test data, while the others based on SLB test data. The ATDCB test usually has higher resistance to the mode I (G_I) and lower resistance to the mode II (G_{II}) and, that is why the G_{II} for the ATDCB test is < 0.25 N/mm while for SLB, the G_{II} is > 0.25 N/mm. Nonetheless, all three envelopes are consistent and reasonably represent the adhesive behaviour, especially between the two envelopes obtained through the SLB test data, where the differences are minimal.

In regard to the other adhesives tested, in between the SLB based envelopes, the results are very similar. However, for the Sikaforce® 7752 adhesive the differences are noticeable. While the SLB envelopes feature a G_I and G_{II} of approximately 3.5 N/mm and 2.5 N/mm, respectively, the ATDCB envelope feature G_I and G_{II} of approximately 3 N/mm and 0.8 N/mm, respectively. This significant deviation on the J_{II} is due to the different mixicity between the SLB and ATDCB tests.

CONCLUSIONS

4 CONCLUSIONS AND PROPOSALS OF FUTURE WORKS

Overall, it can be concluded that the experimental and numerical results performed for each type of adhesive presented consistency and good repeatability, since the items of comparative assessment were reasonably similar in the several specimens analysed.

The P-δ curves obtained by the experimental tests presented the expected results, according to the typical behaviour of the tested adhesives. The Araldite® AV138 brittle adhesive exhibited lower stiffness for a shorter displacement range, while the moderately ductile and ductile adhesives, Araldite® 2015 and Sikaforce® 7752, respectively, exhibited superior stiffness for a longer displacement range. However, the results of the Araldite® 2015 adhesive are near to the brittle adhesive, the Araldite® AV138.

Based on the correlation of experimental and numerical results, it is possible to conclude that the R curves obtained by Ji et al. [1] formulation, based on the J-integral method, presented predictable results, within the acceptable range. As expected, the brittle adhesive, Araldite ® AV138, had the lowest J_C value with a stable crack propagation, due to the well-defined horizontal baseline, while the ductile adhesive, Sikaforce® 7752, presented the highest J_C value and an almost inexistent horizontal baseline, which translated into an unstable crack propagation. Moreover, the comparison between the R curves obtained through two distinct formulations of the J-integral method allows to conclude that the differences are not significant and both represent fairly the adhesive behaviour, despite the different parameters considered in the formulations.

It is also possible to conclude that, through the fracture envelopes, the experimental J_I-J_{II} points, presented low dispersion which, once again, reinforces the repeatability of the results obtained for each test specimen. Based on fracture envelopes, it can be concluded that the power law exponent which best represents the behaviour of the Araldite® 2015 and Araldite® AV138 adhesives is α=1/2, whereas for the Sikaforce® 7752 adhesive, the power law exponent that translates its behaviour corresponds to α=2.

Regarding the cohesive laws obtained for each type of adhesive, it can be concluded that the results obtained are acceptable, since they present small differences between curves of the same adhesive. Due to the known-mixity of the SLB test, the magnitude of the curves meets the expectations, where the tensile stress is higher than the shear stress by a significant margin, with the exception of the pure ductile adhesive, Sikaforce® 7752, which features a very small difference between the stresses. Furthermore, it is also possible to conclude that, similarly to the magnitude of stresses, the cohesive law curves from the Araldite AV138® and Araldite 2015® adhesives clearly resemble the triangular model whereas, for the Sikaforce® 7752 adhesive, the curves are not patterned nor resemble the triangular model, especially for the shear stress, due to the ductile nature of the adhesive and its behaviour when subjected to tensile and shear stresses.

As for the proposals for future works, the following topics show potential for further investigation:

- Application of Prony series instead of polynomial equations, to correlate the experimental and numerical data, in order to obtain more precise J_C results;
- Complete numerical fracture validation through the cohesive law validation, propagation criterion validation and sensitive analysis of the cohesive parameters;
- Perform numerical trials for the Sikaforce® 7752 adhesive using the trapezoidal law and compare its results against the triangular model.

REFERENCES

5 REFERENCES

1. Ji, G., Z. Ouyang, and G. Li, *On the interfacial constitutive laws of mixed mode fracture with various adhesive thicknesses.* Mechanics of Materials, 2012. **47**: p. 24-32.
2. Da Silva, L.F., A. Öchsner, and R.D. Adams, *Handbook of adhesion technology*. 2011: Springer Science & Business Media.
3. Petrie, E.M., *Handbook of adhesives and sealants.* 2000.
4. da Silva, L.F.M., A.G. de Magalhaes, and M.F.S. de Moura, *Juntas adesivas estruturais*. 2007: Publindústria.
5. Adams, R.D., *Adhesive bonding: science, technology and applications*. 2005: Elsevier.
6. SUNSTAR, *Adhesive technology application for automotive industries*, in https://www.sunstar.com/rd/story/weld_bonding, S.-S.g.a.i.w.a.t.W.b. adhesive, Editor.
7. SIKA, *Epoxy resin & structural engineering systems for construction industries*, in https://usa.sika.com/en/solutions_products/Construction-Products-Services/repair-protection-home/epoxy-resin-structural-engineering-systems.html, S.-E.R.S. Engineering, Editor.
8. Packham, D.E., *Handbook of Adhesion, Second Edition*. 2005: John Wiley & Sons, Ltd.
9. Volkersen, O., *Die Nietkraftverteilung in zugbeanspruchten Nietverbindungen mit Konstanten Laschenquerschnitten.* Luftfahrtforschung, 1938. **15:41-7**.
10. Goland, M. and E. Reissner, *The stresses in cemented joints.* Journal of Applied Mechanics, 1944. **A17-A27**.
11. Hart-Smith, L.J., *Adhesive-Bonded Single-Lap Joints*. 1973, NASA CR-112236.
12. Renton, W.J. and J.R. Vinson, *Analysis of Adhesively Bonded Joints Between Panels of Composite Materials.* Journal of Applied Mechanics, 1977. **44**: p. 101-6.
13. Ojalvo, I.U. and H.L. Eidinoff, *Bond Thickness Effects upon Stresses in Single-Lap Adhesive Joints.* AIAA Journal, 1978. **16**: p. 204-11.
14. Allman, D.J., *A THEORY FOR ELASTIC STRESSES IN ADHESIVE BONDED LAP JOINTS.* The Quarterly Journal of Mechanics and Applied Mathematics, 1977. **30**: p. 415-436.
15. Chen, D. and S. Cheng, *An Analysis of Adhesive-Bonded Single-Lap Joints.* Journal of Applied Mechanics, 1983. **50**: p. 109-15.
16. Adams, R.D. and V. Mallick, *A method for the stress analysis of lap joints.* Journal of Adhesion, 1992. **38**: p. 199-217.

17. Zhao, B. and Z.-H. Lu, *A Two-Dimensional Approach of Single-Lap Adhesive Bonded Joints.* Mechanics of Advanced Materials and Structures, 2009. **16**: p. 130-159.

18. Yang, C. and S.-S. Pang, *Stress-Strain Analysis of Single-Lap Composite Joints Under Tension.* Journal of Engineering Materials and Technology, 1996. **118**: p. 247-255.

19. Crocombe, A., *Stress analysis for adhesive structures. 2nd World Congress on Adhesion and Related Phenomena. Florida.* The Adhesion Society, 2002: p. 17-9.

20. da Silva, L.F.M. and R.D.S.G. Campilho, *Advances in Numerical Modelling of Adhesive Joints*, in *Advances in Numerical Modeling of Adhesive Joints*. 2012, Springer Berlin Heidelberg: Berlin, Heidelberg. p. 1-93.

21. Adams, R.D., J. Comyn, and W.C. Wake, *Structural adhesive joints in engineering*. 1997: Chapman and Hall.

22. Barenblatt, G.I., *The formation of equilibrium cracks during brittle fracture. General ideas and hypotheses. Axially-symmetric cracks.* Journal of Applied Mathematics and Mechanics, 1959. **23**(3): p. 622-636.

23. Barenblatt, G.I., *The Mathematical Theory of Equilibrium Cracks in Brittle Fracture*, in *Advances in Applied Mechanics*, H.L. Dryden, et al., Editors. 1962, Elsevier. p. 55-129.

24. Dugdale, D.S., *Yielding of steel sheets containing slits.* Journal of the Mechanics and Physics of Solids, 1960. **8**(2): p. 100-104.

25. Xie, D. and A. Waas, *Discrete cohesive zone model for mixed-mode fracture using finite element analysis*. Vol. 73. 2006. 1783-1796.

26. Wisnom, M.R. and W. Cui, *A Combined Stress Based and Fracture Mechanics Based Model for Predicting Delamination in Composites.* Composites, 1993. **24**: p. 467-474.

27. Feraren, P. and H.M. Jensen, *Cohesive zone modelling of interface fracture near flaws in adhesive joints.* Engineering Fracture Mechanics, 2004. **71**(15): p. 2125-2142.

28. Khoramishad, H., et al., *Predicting fatigue damage in adhesively bonded joints using a cohesive zone model.* International Journal of Fatigue, 2010. **32**(7): p. 1146-1158.

29. Daudeville, L. and P. Ladevèze, *A damage mechanics tool for laminate delamination.* Composite Structures, 1993. **25**(1): p. 547-555.

30. Raghavan, P. and S. Ghosh, *A continuum damage mechanics model for unidirectional composites undergoing interfacial debonding*. Vol. 37. 2005. 955-979.

31. Ashcroft, I.A., A.D. Crocombe, and S.J. Shaw, *Prediction of fatigue thresholds in adhesively bonded joints using damage mechanics and fracture mechanics AU - Wahab, M. M. Abdel.* Journal of Adhesion Science and Technology, 2001. **15**(7): p. 763-781.

32. Shenoy, V., et al., *Fracture mechanics and damage mechanics based fatigue lifetime prediction of adhesively bonded joints subjected to variable amplitude fatigue.* Engineering Fracture Mechanics, 2010. **77**(7): p. 1073-1090.

33. Belytschko, T. and T. Black, *Elastic crack growth in finite elements with minimal remeshing.* International Journal for Numerical Methods in Engineering, 1999. **45**(5): p. 601-620.

34. Mohammadi, S., *Extended Finite Element Method: For Fracture Analysis of Structures*. 2008.
35. Moës, N., J. Dolbow, and T. Belytschko, *A finite element method for crack growth without remeshing.* International Journal for Numerical Methods in Engineering, 1999. **46**(1): p. 131-150.
36. Pocius, A.V. and D.A. Dillard, *Adhesion Science and Engineering - 1*. 2002: Elsevier.
37. ASTM, *ASTM D3433-99(2012), Standard Test Method for Fracture Strength in Cleavage of Adhesives in Bonded Metal Joints*. 2012, ASTM International: Conshohocken, PA.
38. British standard, B.S., *Determination of the Mode I Adhesive Fracture Energy GIC of Structure Adhesives Using the Double Cantilever Beam (DBC) and Tapered Double Cantilever Beam (TDCB) Specimens*. 2001. 3-13.
39. ISO, *ISO 25217:2009, Adhesives -- Determination of the mode 1 adhesive fracture energy of structural adhesive joints using double cantilever beam and tapered double cantilever beam specimens*. 2009. p. 24.
40. Branco, C.A.G.M., *Mecânica dos Materiais*. 1985, Lisboa: Fundação Calouste Gulbenkian.
41. F. Kanninen, M., *An Augmented Double Cantilever Beam Model for Studying Crack Propagation and Arrest*. Vol. 9. 1973. 83-92.
42. Szekrényes, A. and J. Uj, *Beam and finite element analysis of quasi-unidirectional composite SLB and ELS specimens.* Composites Science and Technology, 2004. **64**(15): p. 2393-2406.
43. de Moura, M.F.S.F., R.D.S.G. Campilho, and J.P.M. Gonçalves, *Pure mode II fracture characterization of composite bonded joints.* International Journal of Solids and Structures, 2009. **46**(6): p. 1589-1595.
44. Silva, L.F.M., et al., *Testing Adhesive Joints, Best Practices*. 2012. p. 79-162.
45. Oliveira Jorge, M.Q., F.S.F. de Moura Marcelo, and J.L. Morais José, *Application of the end loaded split and single-leg bending tests to the mixed-mode fracture characterization of wood*, in *Holzforschung*. 2009. p. 597.
46. R. Irwin, G., *Critical Energy Rate Analysis of Fracture Strength*. Vol. 33. 1954. 193-198.
47. Ozdil, F., L.A. Carlsson, and P. Davies, *Beam analysis of angle-ply laminate end-notched flexure specimens.* Composites Science and Technology, 1998. **58**(12): p. 1929-1938.
48. G. Williams, J., *On the calculation of energy release rates for cracked laminates*. Vol. 36. 1988. 101-119.
49. Olsson, R., *A simplified improved beam analysis of the DCB specimen.* Composites Science and Technology, 1992. **43**(4): p. 329-338.
50. Ducept, F., D. Gamby, and P. Davies, *A mixed-mode failure criterion derived from tests on symmetric and asymmetric specimens.* Composites Science and Technology, 1999. **59**(4): p. 609-619.
51. Zhu, Y., *Characterization of interlaminar fracture toughness of a carbon/epoxy composite material*, in *Department of Engineering Science and Mechanics* 2009, The Pennsylvania State University.

52. W.S. Kim, et al., *Enhancement Of Composite-Metal Adhesion Strength By Micro-Patterning Of Metal Surfaces.* 18th International Conference On Composite Materials.

53. Nairn, J.A., *On the calculation of energy release rates for cracked laminates with residual stresses.* International Journal of Fracture, 2006. **139**(2): p. 267.

54. da Silva, L., V.H.C. Esteves, and F.J.P. Chaves, *Fracture toughness of a structural adhesive under mixed mode loadings.* MATERIALWISSENSCHAFT UND WERKSTOFFTECHNIK, 2011. **42**(5): p. 460-470.

55. Fernández, M.V., et al., *Mixed-mode I+II fatigue/fracture characterization of composite bonded joints using the Single-Leg Bending test.* Composites Part A: Applied Science and Manufacturing, 2013. **44**: p. 63-69.

56. Rice, J.R., *A Path Independent Integral and the Approximate Analysis of Strain Concentration by Notches and Cracks.* Journal of Applied Mechanics, 1968. **35**(2): p. 379-386.

57. Szekrényes, A., *J-integral for delaminated beam and plate models*. Vol. 56. 2012. 63-71.

58. Shivakumar, K.N. and I.S. Raju, *An equivalent domain integral method for three-dimensional mixed-mode fracture problems.* Engineering Fracture Mechanics, 1992. **42**(6): p. 935-959.

59. Rigby, R.H. and M.H. Aliabadi, *Decomposition of the mixed-mode J-integral—revisited.* International Journal of Solids and Structures, 1998. **35**(17): p. 2073-2099.

60. Ouyang, Z. and G. Li, *Nonlinear interface shear fracture of end notched flexure specimens.* International Journal of Solids and Structures, 2009. **46**(13): p. 2659-2668.

61. Biel, A., U. Stigh, and T. Walander, *A Critical Study of an Alternative Method to Measure Cohesive Properties of Adhesive Layers*, in *European Conference on Fracture*.

62. Comer, A.J., et al., *Characterising the behaviour of composite single lap bonded joints using digital image correlation.* International Journal of Adhesion and Adhesives, 2013. **40**: p. 215-223.

63. Santos, M.A.S. and R.D.S.G. Campilho, *Mixed-mode fracture analysis of composite bonded joints considering adhesives of different ductility.* International Journal of Fracture, 2017. **207**(1): p. 55-71.

64. Campilho, R.D.S.G., et al., *Modelling adhesive joints with cohesive zone models: effect of the cohesive law shape of the adhesive layer.* International Journal of Adhesion and Adhesives, 2013. **44**: p. 48-56.

65. Campilho, R.D.S.G., et al., *Fracture toughness determination of adhesive and co-cured joints in natural fibre composites.* Composites Part B: Engineering, 2013. **50**: p. 120-126.

66. Campilho, R.D.S.G., et al., *Strength prediction of single- and double-lap joints by standard and extended finite element modelling.* International Journal of Adhesion and Adhesives, 2011. **31**(5): p. 363-372.

67. Faneco, T.M.S., et al., *Strength and fracture characterization of a novel polyurethane adhesive for the automotive industry*. Vol. 45. 2017. 398-407.

68. Santos, M.A.S., *Estudo numérico da fratura em modo misto de juntas adesivas pelo ensaio single-leg bending*, in *Departamento de Engenharia Mecânica*. 2016, Instituto Superior de Engenharia do Porto.

69. Pinto, A.M.G., et al., *Single-Lap Joints of Similar and Dissimilar Adherends Bonded with an Acrylic Adhesive.* The Journal of Adhesion, 2009. **85**(6): p. 351-376.

70. Alfano, G. and M.A. Crisfield, *Finite element interface models for the delamination analysis of laminated composites: Mechanical and computational issues*. Vol. 50. 2001.

71. Allix, O. and A. Corigliano, *Modeling and simulation of crack propagation in mixed-modes interlaminar fracture specimens.* International Journal of Fracture, 1996. **77**(2): p. 111-140.

72. Chandra, N., et al., *Some issues in the application of cohesive zone models for metal–ceramic interfaces.* International Journal of Solids and Structures, 2002. **39**(10): p. 2827-2855.

73. Chen, J., *Predicting Progressive Delamination of Stiffened Fibre-Composite Panel and Repaired Sandwich Panel by Decohesion Models.* Journal of Thermoplastic Composite Materials, 2002. **15**(5): p. 429-442.

74. Kafkalidis, M.S. and M.D. Thouless, *The effects of geometry and material properties on the fracture of single lap-shear joints.* International Journal of Solids and Structures, 2002. **39**(17): p. 4367-4383.

75. Moreira, R.D.F. and R.D.S.G. Campilho, *Strength improvement of adhesively-bonded scarf repairs in aluminium structures with external reinforcements.* Engineering Structures, 2015. **101**: p. 99-110.

76. Nunes, F.A.A. and R.D.S.G. Campilho, *Mixed-mode fracture analysis of adhesively-bonded joints using the ATDCB test specimen.* International Journal of Adhesion and Adhesives, 2018. **85**: p. 58-68.